

1988

Defect Energies And Entropies From Computer Simulation And Ionic Conductivity Measurements

Irene Elizabeth Hooton

Follow this and additional works at: <https://ir.lib.uwo.ca/digitizedtheses>

Recommended Citation

Hooton, Irene Elizabeth, "Defect Energies And Entropies From Computer Simulation And Ionic Conductivity Measurements" (1988). *Digitized Theses*. 1701.
<https://ir.lib.uwo.ca/digitizedtheses/1701>

This Dissertation is brought to you for free and open access by the Digitized Special Collections at Scholarship@Western. It has been accepted for inclusion in Digitized Theses by an authorized administrator of Scholarship@Western. For more information, please contact tadam@uwo.ca, wlsadmin@uwo.ca.



National Library
of Canada

Bibliothèque nationale
du Canada

Canadian Theses Service

Service des thèses canadiennes

Ottawa, Canada
K1A 0N4

NOTICE

The quality of this microform is heavily dependent upon the quality of the original thesis submitted for microfilming. Every effort has been made to ensure the highest quality of reproduction possible.

If pages are missing, contact the university which granted the degree.

Some pages may have indistinct print especially if the original pages were typed with a poor typewriter ribbon or if the university sent us an inferior photocopy.

Previously copyrighted materials (journal articles, published tests, etc.) are not filmed.

Reproduction in full or in part of this microform is governed by the Canadian Copyright Act, R S C 1970, c C-30.

AVIS

La qualité de cette microforme dépend grandement de la qualité de la thèse soumise au microfilmage. Nous avons tout fait pour assurer une qualité supérieure de reproduction.

S'il manque des pages, veuillez communiquer avec l'université qui a conféré le grade.

La qualité d'impression de certaines pages peut laisser à désirer, surtout si les pages originales ont été dactylographiées à l'aide d'un ruban usé ou si l'université nous a fait parvenir une photocopie de qualité inférieure.

Les documents qui font déjà l'objet d'un droit d'auteur (articles de revue, tests publiés, etc.) ne sont pas microfilmés.

La reproduction, même partielle, de cette microforme est soumise à la Loi canadienne sur le droit d'auteur, SRC 1970, c C-30.

Defect Energies and Entropies from Computer Simulation and Ionic Conductivity Measurements

by
Irene Elizabeth Hooton

Department of Chemistry

Submitted in partial fulfillment
of the requirements for the degree of
Doctor of Philosophy

Faculty of Graduate Studies
The University of Western Ontario
London, Ontario
January, 1988

© Irene Elizabeth Hooton 1988

5

Permission has been granted to the National Library of Canada to microfilm this thesis and to lend or sell copies of the film.

The author (copyright owner) has reserved other publication rights, and neither the thesis nor extensive extracts from it may be printed or otherwise reproduced without his/her written permission.

L'autorisation a été accordée à la Bibliothèque nationale du Canada de microfilmer cette thèse et de prêter ou de vendre des exemplaires du film.

L'auteur (titulaire du droit d'auteur) se réserve les autres droits de publication; ni la thèse ni de longs extraits de celle-ci ne doivent être imprimés ou autrement reproduits sans son autorisation écrite.

ISBN 0-315-40775-1

Abstract

Ionic conductivity measurements have been made on pure and strontium- and sulphide-doped sodium chloride and the data analysed by means of a non-linear least squares fitting routine. The purpose of this investigation was two-fold. First, the question as to what types of defects occur in NaCl needed to be resolved. Recent work on KCl^{1,2} indicated that a small concentration of Frenkel defects was present on both sub-lattices in addition to Schottky defects, which have been assumed to predominate in alkali halides. Secondly, a wide variety of values for the anion vacancy migration energy have been given in the literature and it was hoped that the present investigation would help to resolve the correct value of this defect energy. The analysis of the data indicated that Schottky defects do indeed predominate in NaCl. A value of 0.744 eV was determined for the anion migration enthalpy.

In addition to this, calculations were carried out with new potentials for SrCl₂ and Na₂S using the HADES code. The main purpose of these calculations was to develop potentials to be used in defect calculations of NaCl containing Sr²⁺ and S²⁻ impurities; however the availability of these potentials made it possible to carry out additional calculations on SrCl₂ and Na₂S. Although the problem of low defect migration energies commonly found in defect calculations of fluorites³ still persisted, some improvements were made with SrCl₂. No defect calculations on Na₂S had been done previously.

An investigation of the quasi-harmonic approximation was carried out with a set of temperature dependent potentials for NaCl, KCl, and KBr. In the past, quasi-harmonic calculations have been undertaken only with potentials developed at 0 K⁴. However, a lattice which is strain-free at 0 K is no longer at equilibrium at higher temperatures. The temperature dependent potentials were developed over a wide temperature range by fitting to the physical properties of the crystal at 50 K intervals and minimizing the bulk lattice strain. The resulting defect energies were compared to values calculated using the

potentials of Catlow, Diller, and Norgett⁵ developed at 0 K, and additional thermodynamic properties were calculated in the quasi-harmonic approximation.

Acknowledgements

I would like to express my sincere gratitude to Dr. P W M Jacobs for his help and encouragement. I would also like to thank Dr. L.L. Coatsworth for invaluable technical advice.

Table of Contents

Certificate of Examination	ii
Abstract	iii
Acknowledgements	v
Table of Contents	vii
List of Tables	viii
List of Figures	ix
Chapter 1 - Introduction	1
1.1 Statement of Problem	1
1.2 Sodium Chloride Structure and Defects	1
1.3 Ionic Transport	2
1.4 Defect Model for Sodium-Chloride	4
1.5 Anion Transport	5
Chapter 2 - Interionic Potentials	15
2.1 Introduction	15
2.2 Alkali Halides	16
2.3 Sodium Sulphide	18
2.4 Strontium Chloride	19
Chapter 3 - Sodium Sulphide Defect Energy Calculations	52
3.1 Introduction	52
3.2 Sodium Sulphide Defect Calculations	53
3.3 Monovalent Anion Impurity Calculations	56
3.4 NaCl:S ²⁻ Defect Calculations	57
Chapter 4 - Strontium Chloride Defect Calculations	77
4.1 Introduction	77
4.2 Defect Calculations	78
4.3 Monovalent Impurity Defect Calculations	79
4.4 NaCl:Sr ²⁺ Defect Calculations	82
Chapter 5 - Ionic Conductivity Experimental	95
5.1 Sample Preparation	95
5.1.1 Preparation of Sr ²⁺ -Doped Crystals	95
5.1.2 Preparation of S ²⁻ -Doped Crystals	96
5.2 Electrodes	96
5.3 Sample Holder	97
5.4 Vacuum Line	98
5.5 Conductivity Measurements	98
5.6 Data Analysis	100
Chapter 6 - Ionic Conductivity Results and Analysis	108
6.1 Conductivity Experiments	108
6.1.1 Pure Crystals	108

6.1.2 Sr ²⁺ -Doped Crystals	109
6.1.3 S ²⁻ -Doped Crystals	109
6.2 Calculation of Defect Energies Held Constant during the Fitting Procedure	111
6.3 Conductivity Model	111
6.4 Analysis of the Data	112
6.5 Results of the Non-linear Least Squares Fitting	115
6.5.1 Discussion of the Model Type	116
6.5.2 Discussion of Conductivity Parameters	117
6.6 Transport Numbers and Complex Concentrations	118
6.7 Diffusion Coefficient Calculations	119
6.8 Diffusion Coefficient Results	122
Chapter 7 - Alkali Halide Quasi-harmonic Calculations	193
7.1 Introduction	193
7.2 Comparison of Results Using Temperature Dependent and Temperature Independent Potentials	194
7.3 Calculation of Thermodynamic Properties	196
7.4 Temperature Dependence of Conductivity Parameters	199
Vita	242

List of Tables

Table 1-1:	Previously determined defect parameters for NaCl	8
Table 2-1:	Alkali halide lattice parameters	22
Table 2-2:	Symbols and units for potential parameters and physical properties	23
Table 2-3:	Final parameter values for NaCl potential	24
Table 2-4:	Final parameters for KCl potential	25
Table 2-5:	Final parameters for KBr potential	26
Table 2-6:	Elastic constants for the alkali halides	27
Table 2-7:	Static dielectric constant of KCl and KBr ⁴⁷	28
Table 2-8:	High frequency dielectric constant and the frequency of the transverse optic mode for the alkali halides ⁴⁸	29
Table 2-9:	Properties of the alkali halides at 0 K	30
Table 2-10:	Additional potentials	31
Table 2-11:	Potential parameters for Na ₂ S	32
Table 2-12:	Calculated and experimental properties of Na ₂ S	33
Table 2-13:	Force constants for Na ₂ S	34
Table 2-14:	SrCl ₂ potential parameters	35
Table 2-15:	Calculated and experimental values of properties of SrCl ₂	36
Table 2-16:	Force constants for SrCl ₂	37
Table 3-1:	Defect energy symbols	60
Table 3-2:	Formation and migration energies for Na ₂ S	61
Table 3-3:	Arrhenius energies for Na ₂ S	62
Table 3-4:	Impurity complex and migration energies for Na ₂ S calculated using Potential 4 at 50 K	63
Table 3-5:	Energies of solution, binding energies and impurity migration energies for Na ₂ S:Cl ⁻ complexes	64
Table 3-6:	NaCl:S ²⁻ binding energies and vacancy jump energies	66
Table 4-1:	Experimental and previously calculated defect values for SrCl ₂	84
Table 4-2:	Defect energies for SrCl ₂	85
Table 4-3:	Energies of solution, binding energies and impurity migration energies for SrCl ₂ :Na ⁺ complexes	86
Table 4-4:	Impurity-vacancy binding energies and activation energies for vacancy jumps for NaCl:Sr ²⁺	88
Table 6-1:	Calculated Frenkel and vacancy pair energies for NaCl	124
Table 6-2:	Thermodynamic properties determined during fitting of temperature dependence of conductivity	125
Table 6-3:	Final defect parameters for each crystal	126
Table 6-4:	Final average defect parameters	128

List of Figures

Figure 1-1:	Structure of NaCl	9
Figure 1-2:	Point defects in NaCl structure. (a) Schottky defect, (b) Frenkel defects on both sub-lattices. Squares denote vacant lattice sites.	11
Figure 1-3:	Association complexes in NaCl. (a) cation impurity-vacancy, (b) anion impurity-vacancy, (c) vacancy pair	13
Figure 2-1:	Phonon dispersion curves for NaCl. \circ experimental ⁵⁰ , + calculated	38
Figure 2-2:	Phonon dispersion curves for KCl. \circ experimental ⁵⁰ , + calculated	40
Figure 2-3:	Phonon dispersion curves for KBr. \circ experimental ⁵¹ , + calculated	42
Figure 2-4:	Phonon dispersion curves for Na ₂ S. \circ experimental ⁵⁶ , + calculated from Potential 4	44
Figure 2-5:	SrCl ₂ lattice parameters ⁶¹	46
Figure 2-6:	Phonon dispersion curves for SrCl ₂ . \circ experimental ⁶⁴ , + calculated from Potential A3	48
Figure 2-7:	Phonon dispersion curves for SrCl ₂ . \circ experimental ⁶⁴ , + calculated from Potential B1	50
Figure 3-1:	Structure of Na ₂ S	67
Figure 3-2:	Vacancy pair in Na ₂ S (a) structure, (b) anion saddle point, (c) cation saddle point	69
Figure 3-3:	Vacancy triplet in Na ₂ S, (a) structure, (b) anion saddle point, (c) cation saddle point, (d) most stable configuration	71
Figure 3-4:	Na ₂ S:Cl ⁻ complexes	73
Figure 3-5:	NaCl:S ²⁻ complexes and vacancy jumps	75
Figure 4-1:	Structure of SrCl ₂	89
Figure 4-2:	Displacement of Na ⁺ from the cube centre to the face of the empty cube as a function of temperature for the (Na _s ⁺ Na _i ⁺) <100> complex	91
Figure 4-3:	Binding energy as a function of displacement of the (Na _s ⁺ Na _i ⁺) <100> complex	93
Figure 5-1:	Electrode system, (a) single cell, (b) double cell	102
Figure 5-2:	Sample holder	104
Figure 5-3:	Vacuum line	106
Figure 6-1:	Arrhenius plot for pure NaCl	129
Figure 6-2:	Arrhenius plot for three NaCl crystals doped with 360, 190, and 27 ppm strontium	131
Figure 6-3:	Arrhenius plots of pure NaCl and NaCl doped with 60 ppm S ²⁻	133
Figure 6-4:	Arrhenius plot of NaCl doped with 32 ppm S ²⁻	135
Figure 6-5:	Arrhenius plots of pure NaCl and NaCl doped with 19 ppm S ²⁻	137
Figure 6-6:	Arrhenius plots of pure NaCl and NaCl doped with 8.6 ppm S ²⁻	139

Figure 6-7:	Plot of the ratio of the conductivities of NaCl doped with 60 ppm S^{2-} and pure NaCl	141
Figure 6-8:	Plot of the ratio of the conductivities of NaCl doped with 19 ppm S^{2-} and pure NaCl	143
Figure 6-9:	Residuals from fitting of pure NaCl crystal	145
Figure 6-10:	Residuals from fitting of NaCl crystal doped with 19 ppm Sr^{2+}	147
Figure 6-11:	Residuals from fitting of NaCl crystal doped with 8.6 ppm S^{2-}	149
Figure 6-12:	Cation vacancy transport numbers for pure NaCl and NaCl doped with Sr^{2+} and S^{2-}	151
Figure 6-13:	Fraction of complexed impurity in Sr^{2+} -doped NaCl crystals	153
Figure 6-14:	Fraction of complexed impurity in S^{2-} -doped NaCl crystals. The broken line represents values calculated from the final parameters.	155
Figure 6-15:	Total cation diffusion in NaCl doped with 27 ppm Sr^{2+} . The evenly broken line represents B�ni�re's ²¹ data and the unevenly broken line represents Rothman's ¹⁸ data, for pure NaCl. The diffusion coefficients calculated from the results of the present investigation are given by the solid line.	157
Figure 6-16:	Cation diffusion via single vacancies in NaCl doped with 27 ppm Sr^{2+} . The evenly broken line represents B�ni�re's ²¹ data for a pure crystal and the unevenly broken represents his data for a strontium-doped crystal. The diffusion coefficients calculated from the results of the present investigation are given by the solid line.	159
Figure 6-17:	Cation diffusion via vacancy pairs in NaCl doped with 27 ppm Sr^{2+} . The broken line represents B�ni�re's ²⁰ data and the solid line represents the diffusion coefficients calculated from the results of the present investigation.	161
Figure 6-18:	Total anion diffusion in NaCl doped with 27 ppm Sr^{2+} . The broken line represents B�ni�re's ²¹ data for pure NaCl and the diffusion coefficients calculated from the results of the present investigation are given by the solid line.	163
Figure 6-19:	Anion diffusion via single vacancies in NaCl doped with 27 ppm Sr^{2+} . B�ni�re's ²¹ data for pure NaCl are represented by the broken line and the diffusion coefficients calculated from the results of the present investigation are given by the solid line.	165
Figure 6-20:	Anion diffusion via vacancy pairs in NaCl doped with 27 ppm Sr^{2+} . B�ni�re's ²⁰ data are represented by the broken line and the diffusion coefficients calculated from the results of the present investigation are given by the solid line.	167
Figure 6-21:	Total cation diffusion in NaCl doped with 19 ppm S^{2-} . The evenly broken line represents B�ni�re's ²¹ data and the unevenly broken line represents Rothman's ¹⁸ data, for pure NaCl. The diffusion coefficients calculated from the results of the present investigation are given by the solid line.	169

Figure 6-22:	Cation diffusion via single vacancies in NaCl doped with 19 ppm S^{2-} . The broken line represents B�ni�re's ²¹ data for pure NaCl and the solid line represents the diffusion coefficients calculated from the results of the present investigation	171
Figure 6-23:	Cation diffusion via vacancy pairs in NaCl doped with 19 ppm S^{2-} . The broken line represents B�ni�re's ²⁰ data and the solid line represents diffusion coefficients calculated from the results of the present investigation	173
Figure 6-24:	Total anion diffusion in NaCl doped with 19 ppm S^{2-} . The broken line represents B�ni�re's ²¹ data for pure NaCl and the solid line represents diffusion coefficients calculated from the results of the present investigation	175
Figure 6-25:	Anion diffusion via single vacancies in NaCl doped with 19 ppm S^{2-} . The broken line represents B�ni�re's ²¹ data for pure NaCl and the solid line represents diffusion coefficients calculated from the results of the present investigation.	177
Figure 6-26:	Anion diffusion via vacancy pairs in NaCl doped with 19 ppm S^{2-} . The broken line represents B�ni�re's ²⁰ data and the solid line represents the diffusion coefficients calculated from the results of the present investigation.	179
Figure 6-27:	Total cation diffusion in nominally pure NaCl calculated using the average parameter set. The evenly broken line represents B�ni�re's ²¹ data and the unevenly broken line represents Rothman's ¹⁸ data, for pure NaCl. The diffusion coefficients calculated from the results of the present investigation are given by the solid line	181
Figure 6-28:	Cation diffusion via single vacancies in nominally pure NaCl calculated using the average parameter set. B�ni�re's ²¹ data for pure NaCl are represented by the broken line and the diffusion coefficients calculated from the results of the present investigation are given by the solid line	183
Figure 6-29:	Cation diffusion via vacancy pairs in nominally pure NaCl calculated using the average parameter set. B�ni�re's ²⁰ data are represented by the broken line and the diffusion coefficients calculated from the results of the present investigation are given by the solid line.	185
Figure 6-30:	Total anion diffusion in nominally pure NaCl calculated using the average parameter set. B�ni�re's ²¹ data for pure NaCl are represented by the broken line and the diffusion coefficients calculated from the results of the present investigation are given by the solid line.	187
Figure 6-31:	Anion diffusion via single vacancies in nominally pure NaCl calculated using the average parameter set. The broken line represents B�ni�re's ²¹ data for pure NaCl and the solid line represents the diffusion coefficients calculated using the results from the present investigation.	189

Figure 6-32:	Anion diffusion via vacancy pairs in nominally pure NaCl calculated using the average parameter set. The broken line represents B�ni�re's ²⁰ data and the solid line gives the diffusion coefficients calculated using the results from the present investigation.	191
Figure 7-1:	Bulk strain in NaCl as a result of increasing temperature calculated using the CDN potential	200
Figure 7-2:	Experimental ⁴⁵ values of the bulk modulus for NaCl and values calculated using the TD and CDN potentials	202
Figure 7-3:	Experimental ⁴⁵ values of the elastic constant c_{44} for NaCl and values calculated using the TD and CDN potentials	204
Figure 7-4:	Experimental ⁴⁶ values of the static dielectric constant for NaCl and values calculated using the TD and CDN potentials	206
Figure 7-5:	Experimental ⁴⁸ values for the high frequency dielectric constant for NaCl and values calculated using the TD and CDN potentials	208
Figure 7-6:	Experimental ⁴⁸ values for the transverse optic mode for NaCl and values calculated using the TD and CDN potentials	210
Figure 7-7:	Values of u_S for NaCl calculated using the TD and CDN potentials.	212
Figure 7-8:	Values of Δu_{cv} for NaCl calculated using the TD and CDN potentials	214
Figure 7-9:	Values of Δu_{av} for NaCl calculated using the TD and CDN potentials	216
Figure 7-10:	Values of g_S^P , h_S^P , and u_S^V for NaCl calculated using the TD potentials. The solid line represents the value of h_S determined experimentally over the indicated temperature range.	218
Figure 7-11:	Values of s_S^P , s_S^V , and v_S^P/v for NaCl calculated using the TD potentials. The solid line represents the value of s_S determined experimentally over the indicated temperature range.	220
Figure 7-12:	Values of Δg_{cv}^P , Δh_{cv}^P , and Δu_{cv}^V for NaCl calculated using the TD potentials. The solid line represents the value of Δh_{cv} determined experimentally over the indicated temperature range	222
Figure 7-13:	Values of Δs_{cv}^P , Δs_{cv}^V , and $\Delta v_{cv}^V/v$ for NaCl calculated using the TD potentials. The solid line represents the value of Δs_{cv} determined experimentally over the indicated temperature range	224
Figure 7-14:	Values of Δg_{av}^P , Δh_{av}^P , and Δu_{av}^V for NaCl calculated using the TD potentials. The solid line represents the value of Δh_{av} determined experimentally over the indicated temperature range	226
Figure 7-15:	Values of Δs_{av}^P , Δs_{av}^V , and $\Delta v_{av}^V/v$ for NaCl calculated using the TD potentials. The solid line represents the value of Δs_{av} determined experimentally over the indicated temperature range.	228
— Figure 7-16:	Values of g_S^P , h_S^P , and u_S^V for KBr calculated using the TD potentials.	230

Figure 7-17:	Values of s_g^v , s_s^v , and v_g^v/v for KBr calculated using the TD potentials	232
Figure 7-18:	Values of Δg_{cv}^p , Δh_{cv}^p , and Δu_{cv}^v for KBr calculated using the TD potentials	234
Figure 7-19:	Values of Δs_{cv}^p , Δs_{cv}^v , and $\Delta v_{cv}^p/v$ for KBr calculated using the TD potentials	236
Figure 7-20:	Values of Δg_{av}^p , Δh_{av}^p , and Δu_{av}^v for KBr calculated using the TD potentials	238
Figure 7-21:	Values of Δs_{av}^p , Δs_{av}^v , and $\Delta v_{av}^p/v$ for KBr calculated using the TD potentials	240

The author of this thesis has granted The University of Western Ontario a non-exclusive license to reproduce and distribute copies of this thesis to users of Western Libraries. Copyright remains with the author.

Electronic theses and dissertations available in The University of Western Ontario's institutional repository (Scholarship@Western) are solely for the purpose of private study and research. They may not be copied or reproduced, except as permitted by copyright laws, without written authority of the copyright owner. Any commercial use or publication is strictly prohibited.

The original copyright license attesting to these terms and signed by the author of this thesis may be found in the original print version of the thesis, held by Western Libraries.

The thesis approval page signed by the examining committee may also be found in the original print version of the thesis held in Western Libraries.

Please contact Western Libraries for further information:

E-mail: libadmin@uwo.ca

Telephone: (519) 661-2111 Ext. 84796

Web site: <http://www.lib.uwo.ca/>

Chapter One

Introduction

1.1. Statement of Problem

Ionic transport in sodium chloride has been studied by various groups, however, the values for the thermodynamic properties of the defects have not been completely resolved. The main area of controversy lies in the values for the anion parameters. These values have been particularly difficult to determine due to the lack of appropriate anion dopants.

Another area of interest has been the type of defect occurring in sodium chloride. It has been assumed in the past that the defects were of the Schottky type; however, recent work on KCl has suggested the possibility of the presence of a small concentration of Frenkel defects as well. The following is a brief outline of ionic conductivity in sodium chloride. An excellent account of the theory of ionic conductivity in general has been given by Lidiard⁶.

1.2. Sodium Chloride Structure and Defects

Sodium chloride possesses the rock salt structure shown in Figure 1-1. The sodium and chloride ions occupy alternate corners of the cubes.

Two types of point defects might occur in such crystals. The first, and the one assumed to be the dominant defect in NaCl, is the Schottky defect. This defect involves the removal of both a cation and an anion to the surface of the crystal, leaving behind a cation and anion vacancy of virtual charge -1 and $+1$ respectively at their former sites. (Virtual charge assumes a regular lattice site is neutral and therefore removal of the ion results in a charge at that site.) Charge neutrality is conserved. The second type of defect is the Frenkel defect which arises through the displacement of an ion from its regular lattice site to an interstitial position. This might occur on either the cation or anion sub-lattice. Diagrams of these defects are given in Figures 1-2a and 1-2b.

In order to determine the defect parameters to a higher degree of accuracy it would be advantageous to enhance the conductivity of one defect type, for example cation vacancies, with respect to another type of defect and in the case of Schottky defects, this would be the anion vacancies. This can be achieved by adding a small amount of divalent impurity to the pure crystal. In this example, a small addition of divalent cation impurity would also introduce an equal number of cation vacancies in order to conserve charge balance. The same would be true of the addition of a divalent anion impurity. Because the divalent cation impurity has a virtual charge of +1 and the cation vacancy has a virtual charge of -1, these two species will be attracted to each other and may form an impurity-vacancy complex. This same phenomenon occurs in the case of anions and also for cation-anion vacancy pairs. The impurity-vacancy or vacancy pair are said to form a complex when they occupy nearest-neighbour positions as shown in Figure 1-3. A divalent impurity with a vacancy in the second neighbour position is also regarded as a complex defect, but the interactions of defects further apart than the second neighbour position are treated in the Debye-Huckel approximation.

1.3. Ionic Transport

Ionic transport arises through the motion of defects through the crystal. Vacancies migrate through the crystal by direct interchange with an adjacent ion of the same type. Interstitials may move in one of two ways. The first is the interstitial mechanism whereby the ion moves directly from one interstitial site to another. The second type of motion is the interstitialcy mechanism which involves the movement of the interstitial ion to a regular lattice site and the displaced lattice ion to a new interstitial position. The direction of the jump may be either collinear or non-collinear. In the alkali halides, the collinear interstitialcy mechanism has the lowest activation energy and therefore in this investigation this mechanism was assumed to be the one that would occur if Frenkel defects were present.

Previous transport work in sodium chloride can now be examined. This section will

deal with the cation transport and Schottky formation parameters. Section 1.5 deals more explicitly with the problem of anion transport. Ion transport in NaCl has been studied extensively. The Schottky formation and cation migration defect parameters have been resolved satisfactorily using several methods. Contributions to this field have been made by Dreyfus and Novick⁷, Kanzaki *et al.*⁸, Kao *et al.*⁹, Brown and Hoodless¹⁰, Kirk and Pratt¹¹, and Nadler and Rossel¹² to name but a few.

More recently Allnatt, Pantelis, and Sime¹³ measured the conductivity of pure and Sr²⁺-doped NaCl. They were unable to determine a single value for the Schottky formation energy, but their range of values of 2.4 to 2.5 eV was in line with previously determined values. They were able to determine a single value for the cation migration parameters; however the cation association parameters once again fell in a short range of values. The final defect parameters determined in the experiments are listed in Table 1-1 along with other values referred to in the following text. The defect symbols used in this thesis are defined in Tables 3-1 and 6-2 and the units used for these quantities are also given there.

The cation parameters have also been determined by dielectric relaxation measurements by Dryden and Heydon¹⁴. They determined a value for the cation migration enthalpy of 0.678 eV. They suggested that the error introduced by the fact that the impurity and cation do not have the same radii is only ± 0.003 eV. This conclusion was based on a study of NaCl doped with Mn²⁺, Ca²⁺, and Pb²⁺ and indeed their value of 0.678 eV seems reasonable when compared to the other values determined experimentally. Their migration entropy was based on the frequency of the transverse optic mode measured by Martin¹⁵.

In addition to this conductivity and dielectric loss work, combinations of ionic conductivity studies and diffusion, using the sectioning technique, have also been undertaken. Nelson and Friauf¹⁶ determined the Arrhenius energy for cation diffusion.

4

Their measurements involved ionic conductivity experiments on pure crystals and diffusion experiments with ^{22}Na and ^{36}Cl tracers. By applying a field during diffusion measurements they were able to separate the contributions due to pairs and single vacancies. Further measurements by Downing and Friauf¹⁷ at lower temperatures led to a slightly lower value for the Arrhenius energy, namely 1.784 eV. Rothman *et al.*¹⁸ have also determined a value for the Arrhenius energy for Na^+ diffusion. Their value of 2.04 eV for the Arrhenius energy is in good agreement with the other results. A recent thorough investigation of diffusion and conductivity for NaCl and NaCl doped with Sr^{2+} has been reported by B ni re, B ni re, and Chemla^{19, 20, 21}. Their careful diffusion and conductivity work led to the extensive set of parameters listed in Table 1-1.

Theoretical calculations have also been carried out to determine the Schottky formation and cation and anion migration energies for NaCl. The most recent of these involves calculations employing the HADES code. Several potentials have been developed for NaCl for use in this program; however, the most widely quoted work is that of Catlow *et al.*²² These values are also included in Table 1-1 and are in excellent agreement with the experimental values.

1.4. Defect Model for Sodium Chloride

It has been assumed in the past that defects in the alkali halides were of the Schottky type. Acuna and Jacobs^{1, 2} found that by assuming the presence of a small concentration of Frenkel defects on both sub-lattices for KCl they were able to achieve a better fit to the conductivity data. This was especially true at high temperatures where potassium chloride exhibits a slight curvature in the Arrhenius plot of the conductivity. The presence of anion Frenkel defects on the anion sub-lattice also provided a quantitative explanation of the anomalous increase in the diffusivity of Cl^- that occurs at high doping levels of Sr^{2+} ²³. If the inclusion of Frenkel defects in the defect model improved the fitting of the conductivity for KCl, it is possible that this model might also lead to a better understanding of the defect structure of NaCl.

1.5. Anion Transport

As mentioned earlier the anion transport parameters in NaCl have not been determined previously with certainty, due to the absence of an appropriate divalent dopant. The doping of NaCl with Sr^{2+} or another divalent impurity cation leads to an enhancement of the cation transport due to the introduction of cation vacancies. This has not been possible for the anion transport. Chemla and B ni re²⁴ found that it was possible to dissolve up to 36.4 ppm SO_4^{2-} in KCl and they²¹ along with Acu a and Jacobs^{1,2} were able to make use of this to investigate the anion transport in KCl. Unfortunately the solubility of SO_4^{2-} is much less in NaCl, only 2 ppm, and therefore an appropriate anion dopant was still required for this substance.

Several groups have carried out diffusion experiments in order to resolve the anion transport parameters. Laurence²⁵ using the sectioning technique and ^{36}Cl determined an Arrhenius energy of 2.12 eV for anion migration. Morrison^{26, 27, 28} and his group carried out several investigations into anion transport in the alkali halides using the isotope exchange technique developed in their laboratory. They found a value of 1.92 eV for the Arrhenius energy of anion migration.

Allnatt, Pantelis, and Sime¹³ tried to determine the anion migration parameters by fitting the conductivity of pure NaCl crystals without success. Problems arose in the fitting of the anion parameters to the experimental data of pure NaCl due to the linearity of the intrinsic region. Divalent anion doping is required to extract these values from conductivity data.

The most recent measurements are those of B ni re, B ni re, and Chemla²¹. They carried out a combination of conductivity and diffusion (sectioning technique) experiments, and determined a value of 0.77 eV for the anion migration activation energy, which along with their value of 2.44 eV for the Schottky formation energy would result in an Arrhenius energy of 1.99 eV. Thus a fairly consistent set of parameters was

derived from the experimental data which was also in agreement with the HADES values of 0.72 and 0.71 eV²²

Prakash^{29, 30} and Cook and Dryden^{31, 32} found S²⁻ to be sufficiently soluble in NaCl to be useful in anion studies of this crystal. Baba, Ikeda and Yoshida³³ have also carried out ionic conductivity and optical absorption experiments on quenched S²⁻-doped NaCl. The conductivity experiments showed a lowering of the conductance in the extrinsic region of the anion doped crystals with respect to the pure crystals which they attributed to the lower mobility of the anion vacancies. They also found that this region possessed no curvature and attributed the slope of 1.17 eV to the migration of cation vacancies (0.8 eV) and the formation of vacancy pairs, cation vacancy-impurity complexes, cation-anion impurity complexes, and anion vacancy-impurity complexes, the magnitude of the contributions being in the stated order. Their measurements were made at increasing temperatures and hysteresis was noted. Measuring the conductivity with crystal ageing revealed a drop in conductance with time due to the formation of complexes. The optical absorption work showed a disappearance of sulphur complexes in as-grown crystals on heating and their reappearance on ageing of the quenched crystal.

Cook and Dryden^{31, 32} carried out dielectric relaxation experiments on NaCl doped with S²⁻. They assumed that the divalent impurity ion would remain isolated from the vacancy on quenching and therefore association would not need to be included in the analysis, unlike the divalent cation doped crystals. They determined a value of 1.24 eV for the anion vacancy migration. This value is higher than those previously determined and therefore further investigation is required to resolve this discrepancy.

Cook and Dryden³⁴ have also made dielectric absorption measurements and measurements of thermally stimulated depolarizing currents in an attempt to detect divalent anion impurity-vacancy dipoles but were unsuccessful although optical absorption and emission spectra indicate changes on ageing of the quenched crystals.

which have been attributed to the formation of these complexes. They suggested that their lack of success was due to a mechanism which reduces the dipole of the pair by electron-sharing

Equations in the following text are numbered from (1) in each individual chapter and will be referred to as Equation (n) within a chapter and as Equation (c-n) outside the chapter, where c refers to the chapter. Tables and Figures are collected at the end of each Chapter

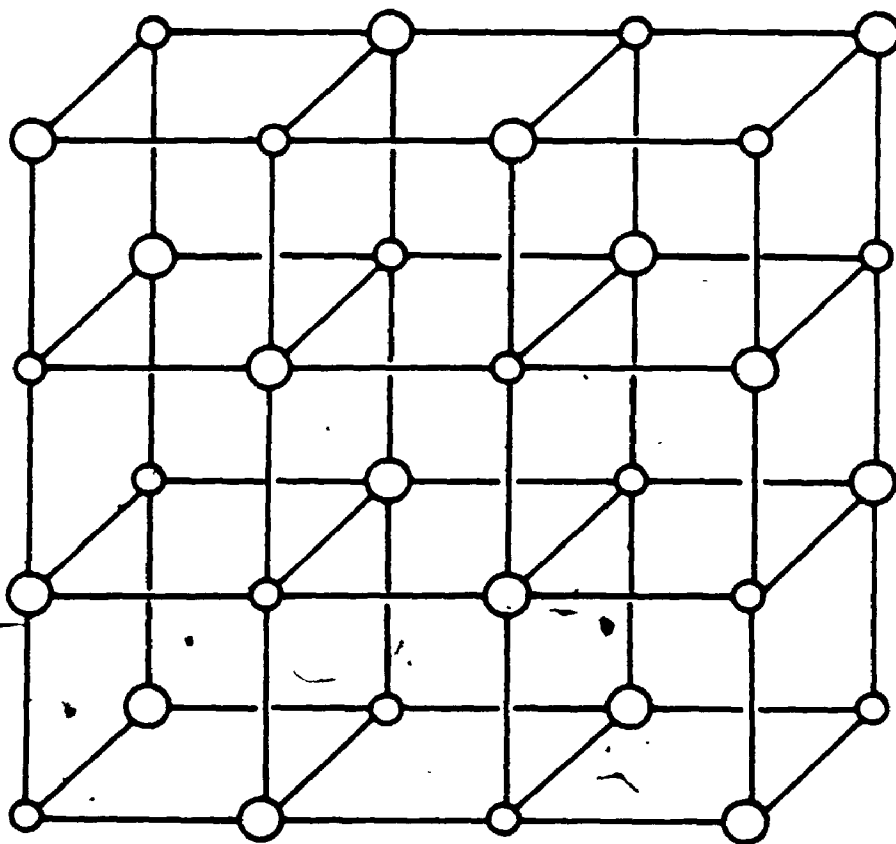
Table I-1: Previously determined defect parameters for NaCl

Ref	h_S	s_S	Δh_{cv}	Δs_{cv}	Δh_{av}	Δs_{av}	$-h_{ck}$	$-s_{ck}$
21	2.44	9.8	0.69	1.64	0.77	1.38	0.46	0.48
13	2.4-2.5	9-10	0.65	1.7	1.5	1.0	0.6-0.9	2-4
14			0.678	1.87				
31					1.24			

Ref	E_{cv}	E_{av}
27		1.92
16	2.10	
17	1.78	
18	2.04	

Ref	u_S	Δu_{cv}	Δu_{av}
22	2.32	0.68	0.72
22	2.54	0.66	0.71

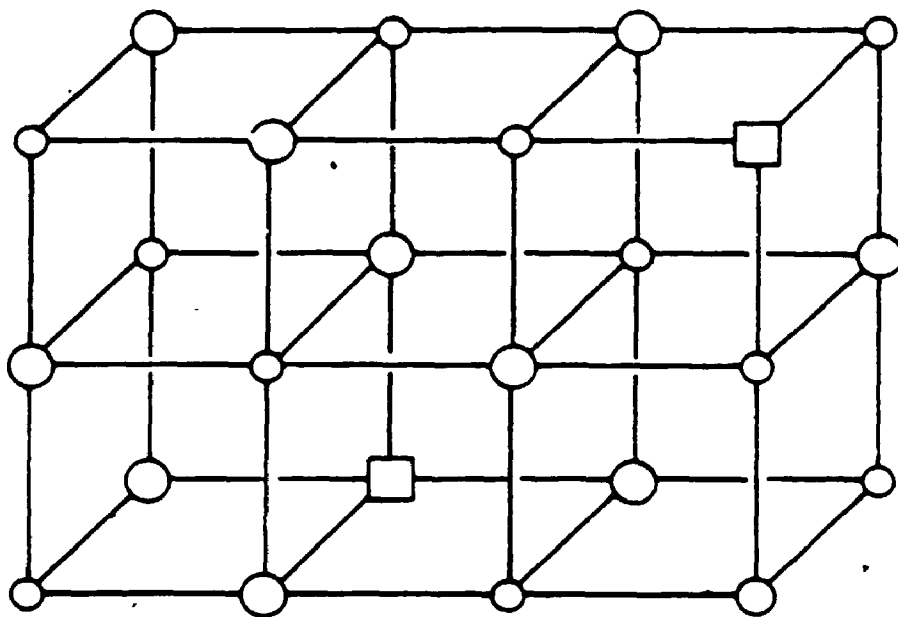
Figure 1-1: Structure of NaCl



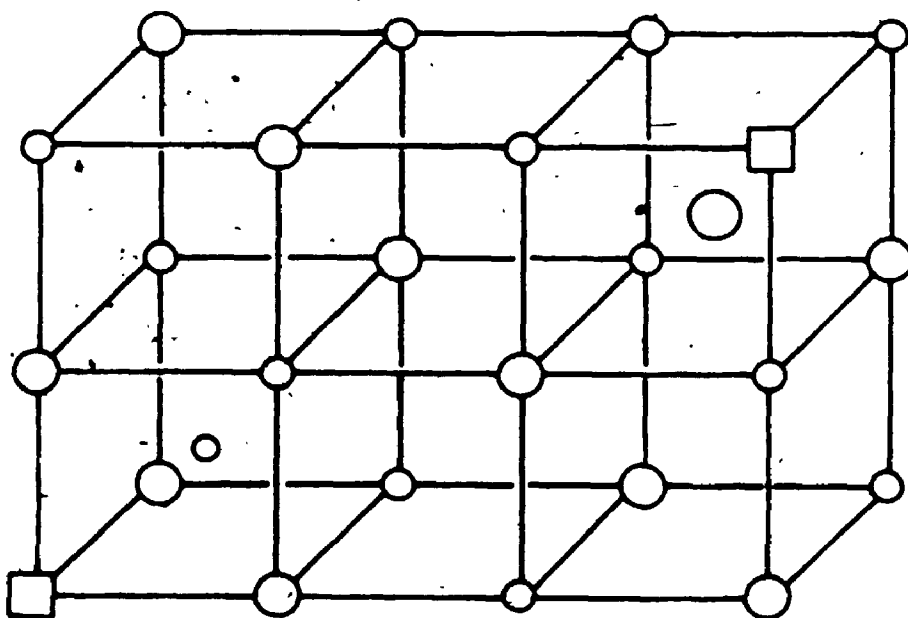
○ Na⁺

○ Cl⁻

Figure 1-2: Point defects in NaCl structure, (a) Schottky defect, (b) Frenkel defects on both sub-lattices. Squares denote vacant lattice sites.

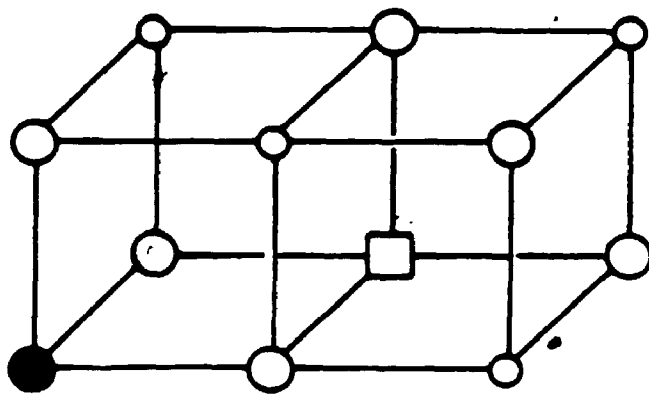


α

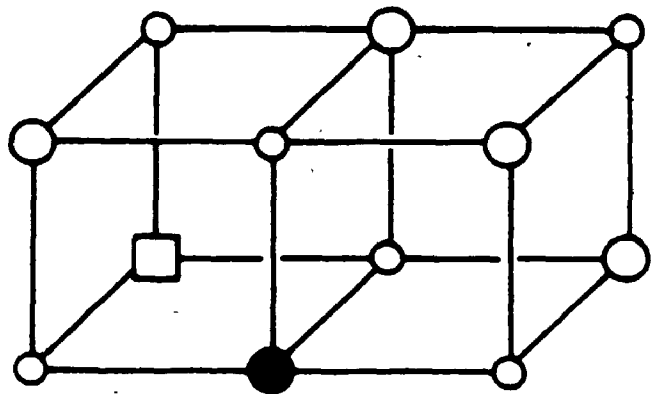


β

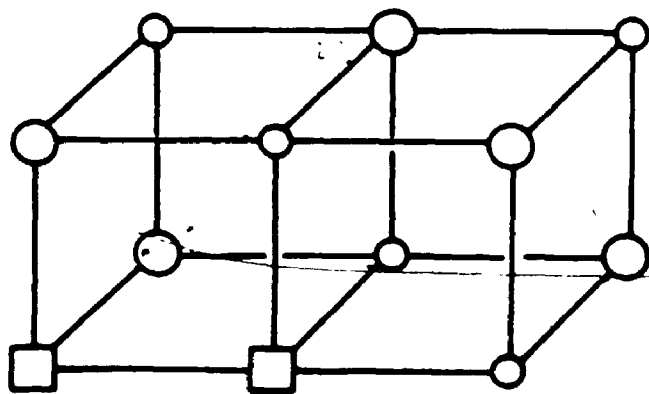
Figure 1-3: Association complexes in NaCl, (a) cation impurity-vacancy, (b) anion impurity-vacancy, (c) vacancy pair



a



b



c

Chapter Two

Interionic Potentials

2.1. Introduction

Potentials for the alkali halides, NaCl, KBr, and KCl, as well as SrCl₂ and Na₂S, were derived using the method employed previously by Catlow *et al*³⁵. The following is only a brief summary of the development of these potentials since the method has been discussed in detail in the previously mentioned reference and in the references quoted therein.

The interactions of the ions in a crystal lattice were treated in the pair-potential approximation, ignoring many-body interactions, since defect energy calculations with the HADES program are presently limited to two-body potentials. The short-range component was described by a Buckingham function,

$$V_{ij}(r) = A_{ijk} \exp(-r/\rho_{ijk}) - C_{ij} r^{-6} \quad (1)$$

where the subscripts *i* and *j* denote ion types. A double exponential form of this equation was used for the anion-anion interactions and the subscript *k* was used to specify each Born-Mayer term.

Parameters were derived by a combination of non-empirical calculations and the fitting of the potential to crystal properties. Initially the parameters were calculated using the electron-gas approximation developed by Wedepohl³⁶ and later modified by Gordon and Kim^{37, 38}.

The shell model of Dick and Overhauser³⁹ was used to ensure an adequate description of the dielectric properties of the crystals⁵. In this model, each ion *i* is represented by a core and shell of charge *X_i* and *Y_i*, respectively, such that the sum of these charges is equal to the ionic charge. The shell and core are coupled harmonically by a force constant, *K_i*. The mass of the ion is centred at the core and the shells are assumed to have negligible inertia.

These potentials were used in the PLUTO program⁴⁰ to calculate the elastic and dielectric properties of the perfect crystal and were modified iteratively to achieve better agreement with the experimental data. The phonon dispersion was calculated using the program PHONON. This provides a check not only on the frequencies of the longitudinal and transverse optic modes at Γ but also of all the acoustic and optic mode frequencies throughout the Brillouin Zone.

2.2. Alkali Halides

Several potentials for the alkali halides have been developed using slightly modified forms of the Born-Mayer equation to describe the interactions of the ions^{5, 41, 42}. In all previous investigations, potentials were fitted at one temperature only, usually 0 K. If these potentials are then utilized at other temperatures, using the quasi-harmonic approximation^{4, 43, 44}, the bulk lattice strains will inevitably not be zero at other temperatures. The present study was undertaken to determine the temperature dependence of the potentials in a strain-free crystal.

A set of temperature dependent potentials (TD) were developed for NaCl, KCl, and KBr. These potentials were derived by varying the repulsive and hardness terms in the nearest-neighbour interaction, A_{121} and ρ_{121} respectively, the Van der Waals coefficient in the anion-anion interaction, C_{22} , the shell and core charges, X_1 and Y_1 for the cation, and X_2 and Y_2 for the anion, and the core-shell coupling constants, K_1 and K_2 . Potentials were developed for the three alkali halides in the quasi-harmonic approximation at approximately 50 K intervals from 0 K to their melting points, by varying the lattice constant, a , using the thermal expansion data listed in Table 2-1. The final parameters are given in Tables 2-3, 2-4, and 2-5 for NaCl, KCl, and KBr respectively; the symbols used for the potential parameters and their units are given in Table 2-2.

The short-range part of the alkali halide crystal potentials was modified to reproduce

the bulk modulus and c_{44} using the elastic data of Slagle and McKinstry⁴⁵ which is listed in Table 2-6. The shell-model parameters were used to vary the calculated dielectric properties and the frequency of the transverse optic mode. The equation for the static dielectric constant derived by Rao and Smakula⁴⁶ was used for NaCl and is given below,

$$\epsilon_s = 5.4 + 2.7 \exp\left(-\frac{0.05 \text{ eV}}{kT}\right) \quad (2)$$

Smith's data⁴⁷ were used for KCl and KBr. The difference in the calculated and experimental values was less than one percent for these properties. The values for the high frequency dielectric constant and transverse optic mode frequency were determined by extrapolating the 2 and 290 K data of Lowndes and Martin⁴⁸. The experimental dielectric data are presented in Tables 2-7 and 2-8. The residual bulk strains in these crystals produced by the final potentials were less than one part in 10^4 . Table 2-9 lists the 0 K properties calculated for each potential, along with the experimental values, and also the values calculated from the Catlow, Diller, and Norgett (CDN) potentials⁵. The CDN spline potentials were used for KCl and KBr. The symbols are explained in Table 2-2.

In order to fit the data over the entire temperature range, it was necessary to decrease A_{121} and increase ρ_{121} as the temperature was increased. This resulted in a potential in which the first-neighbour interaction became more repulsive with increasing temperature. It was also necessary to increase C_{22} with temperature, so that the second-neighbour anion-anion interaction became more attractive with increasing temperature. Plots of the nearest-neighbour potential energy and the anion-anion Van der Waals coefficient as a function of lattice parameter for KCl have been published elsewhere⁴⁹. These results are typical of all three alkali halides.

Phonon dispersion curves were generated using the 80 K potentials for each of the crystals and the resulting plots compared with those found in the literature. The calculated curves showed good agreement with the experimental results, (NaCl and KCl,

Raunio and Rolandson⁵⁰, KBr, Bilz and Kress⁵¹) as illustrated in Figures 2-1, 2-2, and 2-3

Some additional interionic potentials were required for the sodium chloride system in order to calculate the relevant energies for the addition of impurity ions to the pure crystal. Potentials for the sulphide-chloride and sodium-strontium interactions were derived from electron-gas calculations and are listed in Table 2-10. The parameters derived in Sections 2-3 and 2-4 were used for the sodium-sulphide and strontium-chloride interactions

2.3: Sodium Sulphide

There have been a few previous attempts to derive potentials for sodium sulphide. Jain and Shanker⁵² developed potentials for the alkali chalcogenides to calculate the cohesive energy, bulk modulus and its pressure derivatives. These potentials were the sum of three terms representing the electrostatic, van der Waals and repulsive energies. Agnihotri *et al*⁵³ also derived a set of potentials to calculate the cohesive energy, second-order elastic constants, and their pressure derivatives. Their potentials consisted of long-range Coulomb and three-body interactions and short-range dispersive and repulsive interactions. Neither of these potentials are readily adaptable to defect calculations. Pandey and Harding⁵⁴ developed a potential for Na₂S when studying calcium sulphide since the bulk properties of Na₂S are better known than those for CaS.

Since it was not possible to fit simultaneously as many physical properties for sodium sulphide as for the alkali halides, four potentials were developed which differed in the emphasis of their fit to the 0 K properties. In Potential 1, the longitudinal and transverse optic and Raman frequencies⁵⁵ were fitted preferentially. Potentials 2 and 3 were developed to reproduce the dielectric constants and elastic constants^{56, 55}, the difference in the two potentials being that c_{12} was fitted in Potential 2 and c_{44} was fitted in Potential 3. The optic and Raman frequencies, and the force constants derived from

the phonon dispersion experiments by Buhrer and Bull⁵⁷ and the elastic and dielectric constants calculated from these values were used to produce Potential 4. This was done in order to achieve a better fit to the phonon dispersion curves. The short-range potential was derived by varying A_{121} , ρ_{121} , ρ_{221} , and C_{22} and the shell parameters were varied to fit the dielectric data. In each case, the potential produced essentially zero bulk lattice strains (less than 1 part in 10^4). The lattice constant of Na_2S is 3.263 \AA ⁵⁸ at room temperature and 3.252 \AA ⁵⁷ at 50 K.

The final potentials are given in Table 2-11. The calculated properties, excluding force constants, are listed in Table 2-12 along with the experimental values. The force constants are given in Table 2-13. Since Na_2S and the fluorites have the same structure (with anion and cation sub-lattices interchanged), the definition of the force constants is the same as that given by Elcombe^{59, 60}. The phonon dispersion curves produced from Potential 4 are plotted in Figure 2-4 and are in good agreement with experiment. Only Potential 4 was used for the final defect calculations, for reasons outlined in Section 3.2, and therefore only this set of curves has been included, although the phonon dispersion was calculated for all four potentials.

2.4. Strontium Chloride

Bendall and Catlow³ have developed a potential to describe the defect properties of pure strontium chloride and strontium chloride containing sodium impurities. This potential consisted of Buckingham potentials to describe the cation-anion and anion-anion interactions, the ionic polarization being treated using the shell model. The calculated anion Frenkel formation energy was in good agreement with the experimental value however, the anion interstitial migration energy was low, a common problem with defect calculations for fluorites. It was therefore decided to develop a new potential which would also incorporate a strontium-strontium interaction.

It was found not to be possible to develop a single two-body potential which would

reproduce both c_{12} or c_{44} as well as the phonon frequencies and therefore three potentials were developed at 0 K. Potential A1 involved the preferential fitting of c_{44} at the expense of the phonon frequencies and Potential A2 reversed this emphasis. The third potential, A3, was a compromise between the other two. The consequences of fitting c_{12} instead of c_{44} were investigated, but it was found that the compromise potential gave results for the defect energies in best agreement with experimental values. A better fit to the elastic constants resulted in values in closer agreement for the anion Frenkel defect formation energy, but at the expense of the anion interstitial migration energy. Conversely, fitting to the phonon frequencies resulted in a higher value for the anion interstitial migration energy but also a higher value for the anion Frenkel formation energy.

A fourth potential, B1, was also developed at 0 K using the lattice parameter quoted by Bendall and Catlow. The lattice parameter used in the first three potentials was extrapolated from the values determined from the neutron scattering experiments of Dickens *et al*⁶¹ and was lower than the value given by Bendall⁶² (Figure 2-5). However, this potential was developed in order to determine the effect that fitting to an alternate lattice parameter has on the final defect energies. Since the compromise potential was the most successful in defect calculations, Potential B1 was fitted to the experimental data in the same way.

The nearest-neighbour repulsive and hardness parameters and the anion-anion hardness parameter in the electron-gas potentials were varied to reproduce the experimental values for these properties, as indicated above. The dielectric constants were fitted by varying the shell parameters, as described in Section 2.2. The bulk lattice strain was also minimized. The lattice parameter, a , was interpolated from neutron scattering studies⁶¹ and these values are given in Figure 2-5. The potential parameters are given in Table 2-14. The calculated properties and experimental values are listed in Table 2-15. The force constants were also calculated and compared to the literature

values⁶³ and these results are also given in Table 2-16. The definition of the force constants is the same as that given by Elcombe for CaF_2 ⁵⁹ and SrF_2 ⁶⁰.

Phonon dispersion curves were plotted and compared to the experimental curves⁶⁴. Sets of curves calculated from Potentials A3 and B1 are plotted in Figures 2-6 and 2-7, and the results exhibit good agreement with experiment. These potentials are given since they were the ones used in the majority of the defect calculations.

Table 2-1: Alkali halide lattice parameters

Temperature K	Lattice Parameter \AA		
	NaCl ⁶⁵	KCl ⁶⁶	KBr ⁶⁷
0	2.789	3.116	3.262
80	2.7972	3.1258	3.265
200	2.8091	3.1361	3.2764
300	2.8201	3.1468	3.2889
350	2.8257	3.1525	3.2954
400	2.8316	3.1585	3.3020
450	2.8377	3.1647	3.3089
500	2.8440	3.1713	3.3160
550	2.8506	3.1781	3.3234
600	2.8574	3.1851	3.3310
650	2.8645	3.1925	3.3390
700	2.8719	3.2001	3.3472
750	2.8795	3.2079	3.3558
800	2.8874	3.2161	3.3648
850	2.8958	3.2245	3.3742
900	2.9046	3.2332	3.3857
950	2.9138	3.2421	3.3952
1000	2.9235	3.2574	-

The lattice parameter a is the nearest-neighbour anion-cation distance in the rock salt structure.

Table 2-2: Symbols and units for potential parameters and physical properties

Symbol	Definition	Units
Parameters:		
A_{ijk}	repulsive parameter	eV
ρ_{ijk}	hardness parameter	\AA
C_{ij}	Van der Waals coefficient	eV \AA^6
X_i	core charge	e
Y_i	shell charge	e
K_i	core-shell coupling force constant	eV/\AA^2
Properties:		
c_{ij}	elastic constants	10^{10}N/m^2
B	bulk modulus = $(c_{11} + 2c_{12})/3$	10^{10}N/m^2
A_i, B_i	force constants	$\text{e}^2/2v$
a	lattice constant (a_0)	\AA
v	unit cell volume = $2a^3$	\AA^3
ϵ_s	static dielectric constant	
ϵ_∞	high-frequency dielectric constant	
ω_{TO}	transverse optic mode frequency	cm^{-1}
ω_{LO}	longitudinal optic mode frequency	cm^{-1}
ω_{R}	Raman frequency	cm^{-1}
BLS	bulk lattice strain	

Table 2-3: Final parameter values for NaCl potential

Temp K	V_{121}	ρ_{121}	C_{22}	γ_1	K_1	γ_2	K_2
0	1566	0.304	0.0	2.05	203	-2.05	17.4
80	1710	0.302	0.0	1.88	160	-1.92	14.9
200	1643	0.305	0.0	2.12	166	-2.12	18.9
300	1396	0.312	0.0	2.25	198	-2.20	20.4
350	1277	0.316	3.6	2.20	209	-2.20	20.2
400	1164	0.320	6.1	2.19	188	-2.18	19.7
450	1062	0.325	9.2	2.18	221	-2.18	19.5
500	958	0.330	13.7	2.11	195	-2.13	18.6
550	878	0.335	16.4	2.11	204	-2.11	18.1
600	798	0.340	21.0	2.07	175	-2.06	17.2
650	727	0.345	24.8	1.97	132	-1.99	15.9
700	662	0.351	29.3	1.93	162	-1.95	14.9
750	599	0.357	35.9	1.89	146	-1.89	13.9
800	538	0.363	43.0	1.83	143	-1.83	12.8
850	484	0.370	50.1	1.74	125	-1.76	11.5
900	433	0.378	58.1	1.67	110	-1.67	10.2
950	385	0.386	67.3	1.59	107	-1.59	9.0
1000	340	0.395	77.8	1.48	69	-1.50	7.7

Temperature Independent Values:

A_{111} : 6714

A_{221} : 1175

A_{222} : 108771

ρ_{111} : 0.180

ρ_{221} : 0.255

ρ_{222} : 0.137

C_{11} : 3.14

C_{12} : 0.0

Table 2-4: Final parameters for KCl potential

Temp K	λ_{121}	ρ_{121}	C_{22}	γ_1	K_1	γ_2	K_2
0	2989	0.316	180	2.76	81	-2.76	33.4
80	2929	0.318	187	2.90	91	-2.90	37.7
200	2704	0.321	191	3.12	109	-3.12	43.9
300	2361	0.327	198	3.13	110	-3.13	44.3
350	2143	0.332	203	3.16	109	-3.12	43.8
400	2041	0.334	210	3.25	116	-3.19	45.8
450	1778	0.341	214	3.16	108	-3.13	44.0
500	1597	0.346	223	3.17	109	-3.15	44.7
550	1426	0.351	227	3.18	110	-3.14	44.1
600	1277	0.357	234	3.01	97	-3.10	42.8
650	1143	0.363	243	3.11	105	-3.10	43.0
700	1020	0.369	251	3.05	99	-3.05	41.4
750	906	0.376	261	3.02	97	-3.02	40.4
800	810	0.383	272	3.06	100	-3.06	41.5
850	713	0.390	284	3.00	95	-3.01	40.0
900	628	0.398	297	2.98	93	-2.98	39.1
950	551	0.407	313	2.94	90	-2.94	37.7
1000	490	0.416	327	3.08	96	-2.84	35.0

Temperature Independent Values:

- A_{111} : 5155
- ρ_{111} : 0.262
- C_{11} : 50.0
- A_{221} : 1175
- ρ_{221} : 0.255
- A_{222} : 108772
- ρ_{222} : 0.137
- C_{12} : 0.0

Table 2-5: Final parameters for KBr potential

Temp K	V_{121}	ρ_{121}	C_{22}	γ_1	K_1	γ_2	K_2
0	3620	0.323	417	2.90	93.2	-2.90	28.8
80	3150	0.329	420	2.93	65.8	-2.94	21.6
200	2380	0.340	428	2.97	97.2	-2.97	28.4
300	1922	0.350	437	2.72	71.9	-2.69	22.5
350	1765	0.355	442	2.78	84.5	-2.79	24.8
400	1595	0.360	448	2.81	80.1	-2.84	25.6
450	1437	0.365	455	2.91	88.9	-2.91	27.0
500	1286	0.371	461	2.90	87.8	-2.89	26.6
550	1144	0.377	469	2.90	88.8	-2.91	26.9
600	1028	0.383	478	2.91	89.6	-2.91	26.9
650	926	0.390	488	2.89	87.3	-2.89	26.4
700	833	0.396	499	2.84	85.3	-2.86	25.8
750	748	0.403	510	2.83	82.9	-2.84	25.2
800	668	0.410	523	2.68	68.4	-2.73	23.1
850	592	0.418	538	2.81	80.3	-2.80	24.3
900	493	0.431	553	2.40	51.3	-2.44	18.0
950	403	0.445	573	2.44	58.4	-2.44	18.0

Temperature Independent Values.

A_{111} 5155

ρ_{111} 0.262

C_{11} 50.0

C_{12} 0.0

A_{221} 903

ρ_{221} 0.380

A_{222} 17534

ρ_{222} 0.203

Table 2-6: Elastic constants for the alkali halides

The elastic constants of NaCl, KCl and KBr were determined from the following equation²⁵,

$$c_{ij} \cdot 10^{10} \text{ N m}^{-2} = A_0 + A_1 T + A_2 T^2 + A_3 T^3 + A_4 T^4$$

	A_0	$A_1 \cdot 10^{-3}$	$A_2 \cdot 10^{-6}$	$A_3 \cdot 10^{-9}$	$A_4 \cdot 10^{-12}$
NaCl					
c_{11}	5.037	-3.552	-0.748	2.752	-1.912
c_{44}	1.287	-0.316	-0.187	0.160	-0.145
$(c_{11} - c_{12})/2$	1.880	-1.871	-0.368	1.701	-1.052
KCl					
c_{11}	4.138	-2.796	-1.762	3.918	-2.357
c_{44}	0.634	-0.123	-0.103	0.088	-0.092
$(c_{11} - c_{12})/2$	1.719	-1.577	-0.840	2.239	-1.326
KBr					
c_{11}	3.540	-2.567	-1.620	4.349	-2.986
c_{44}	0.511	-0.098	-0.116	0.132	-0.119
$(c_{11} - c_{12})/2$	1.485	-1.487	-0.332	1.161	-0.544

Table 2-7: Static dielectric constant of KCl and KBr³⁷

Temperature K	KCl	KBr
0	4.48	4.48
200	4.63	4.66
300	4.85	4.72
350	4.84	4.78
400	4.92	5.00
450	5.00	5.10
500	5.09	5.20
550	5.18	5.32
600	5.30	5.42
650	5.40	5.52
700	5.52	5.64
750	5.66	5.80
800	5.81	5.94
850	5.98	6.12
900	6.17	6.28
950	6.37	6.50
1000	6.60	

Table 2-8: High frequency dielectric constant and the frequency of the transverse optic mode for the alkali halides¹⁸

Property	NaCl	KCl	KBr
ϵ_{∞}			
2 K	2.35	2.20	2.39
290 K	2.33	2.17	2.36
ω_{TO}			
2 K	178	151	123
290 K	164	142	114

Table 2-9: Properties of the alkali halides at 0 K

Property	NaCl			KCl			KBr		
	Expt	TD	CDN	Expt	TD	CDN	Expt	TD	CDN
ϵ_{11}	5.73 ⁴⁵	5.32	5.89	4.83 ⁴⁵	4.58	4.96	4.02 ⁴⁵	4.21	4.17
ϵ_{12}	1.12 ⁴⁵	1.33	1.34	0.54 ⁴⁵	0.66	0.66	0.35 ⁴⁵	0.53	0.52
ϵ_{44}	1.33 ⁴⁵	1.33	1.35	0.66 ⁴⁵	0.66	0.66	0.53 ⁴⁵	0.53	0.52
B	2.66	2.66	2.63	1.97	1.97	2.09	1.57	1.76	1.74
ϵ_s	5.45 ⁴⁶	5.45	5.38	4.48 ⁴⁷	4.41	4.25	4.48 ⁴⁷	4.43	4.34
ϵ_∞	2.35 ⁴⁸	2.35	2.39	2.20 ⁴⁸	2.22	2.17	2.39 ⁴⁸	2.41	2.37
ω_{TO}	178 ⁴⁸	192	170	151 ⁴⁸	154	149	123 ⁴⁸	124	119
BLS $\times 10^5$	-	0.0	0.84	-	0.0	0.16	-	0.0	0.04

Table 2-10: Additional potentials

Parameter	$\text{Sr}^{2+} - \text{Na}^+$	$\text{Cl}^- - \text{S}^{2-}$
A_{ij1}	7196.6	1086.6
P_{ij1}	0.218	0.335
C_{ij}	6.141	57.16
A_{ij2}	-	76057.1
P_{ij2}	-	0.142

Table 2-11: Potential parameters for Na₂S

Potential	A ₁₂₁	ρ ₁₂₁	ρ ₂₂₁	C ₂₂	Y ₁	Y ₂	K ₁	K ₂
1	1513.0	0.340	0.475	11.81	2.50	-5.10	92.0	60.0
2	4044.8	0.300	0.475	11.81	1.80	-6.28	92.0	101.2
3	5075.0	0.294	0.369	11.81	2.75	-6.44	92.0	121.2
4	748.0	0.384	0.320	685.00	1.80	-5.40	92.0	120.0

Parameters common to all potentials:

A₁₁₁: 6714.1

ρ₁₁₁: 0.180

C₁₁: 3.14

A₂₂₁: 312.5

A₂₂₂: 11483.1

ρ₂₂₂: 0.186

C₁₂: 0.0

Table 2-12 Calculated and experimental properties of Na_2S

Potential	ϵ_{11}	ϵ_{12}	ϵ_{44}	ϵ_s	ϵ_∞	ω_{LO}	ω_{TO}	ω_R	BLS
1	7.42	2.59	1.91	8.51	3.28	326	203	192	0.00
2	8.12	3.29	2.67	5.95	2.69	358	240	207	0.00
3	8.12	3.50	2.07	5.95	2.96	364	257	214	0.00
4	6.44	2.17	1.78	6.45	2.02	335	197	188	0.00
expt	8.12 ⁵⁶	3.3 ⁵⁶	2.1 ⁵⁶	5.95 ⁵⁶	2.96 ⁵⁵	305 ⁵⁵	215 ⁵⁵	190 ⁵⁵	
	6.44 ⁵⁷	2.17 ⁵⁷	1.79 ⁵⁷				2.41 ⁵⁷		

Table 2-13: Force constants for Na_2S

Potential	λ_1	B_1	λ_2	B_2
1	15.5	-1.87	-0.036	0.006
2	17.6	-1.87	6.799	-0.987
3	18.7	-1.94	1.449	-0.156
4	15.7	-2.14	-0.037	0.006
A	12.0	1.16	4.7	-0.96

A Buhrer and Bill⁵⁷

Table 2-14: SrCl₂ potential parameters

Potential	A ₁₂₁	ρ ₁₂₁	P ₂₂₁	C ₂₂	Y ₁	Y ₂	K ₁	K ₂
A1	1352.4	0.358	0.354	0.0	2.77	-2.15	54.8	60.0
A2	2376.8	0.342	0.359	0.0	4.75	-2.15	250.0	60.0
A3	2288.5	0.336	0.347	0.0	4.75	-2.15	250.0	60.0
B1	5193.5	0.307	0.345	30.0	9.60	-2.15	231.5	60.0

Parameters common to all potentials

A₁₁₁: 9949.1 N

ρ₁₁₁: 0.245

C₁₁: 0.0

A₂₂₁: 1175.2

A₂₂₂: 108771.7

ρ₂₂₂: 0.137

C₁₂: 0.0

Table 2-15: Calculated and experimental values of properties of SrCl_2

Potential	ϵ_{1f}	ϵ_{12}	ϵ_{44}	ϵ_s	ϵ_∞	ω_{10}	ω_{10}	ω_R	BLS
A1	7.55	1.33	1.03	6.38	1.70	114	220	169	0.0
A2	8.77	2.59	1.81	4.06	1.58	155	248	187	0.0
A3	7.55	1.70	1.36	5.34	1.59	130	238	170	0.0
B1	7.55	2.26	1.75	6.94	2.74	145	231	171	0.0
expt ⁶³	7.55	1.72	1.03	6.94	2.7	155	248	188	

Table 2-16: Force constants for SrCl₂

Potential	A_1	B_1	A_2	B_2
A1	13.7	-1.62	2.95	-0.300
A2	18.0	-2.05	3.31	-0.342
A3	15.0	-1.68	2.54	-0.253
B1	17.3	-1.76	2.02	-0.185
ASM ^a	16.8	-1.26	2.12	0.047
SDM ^b	17.3	-1.33	1.75	0.280

^a Non-deformable shell model⁶³

^b Shell deformation model⁶³

Figure 2-1: Phonon dispersion curves for NaCl. \circ experimental⁴⁹, + calculated

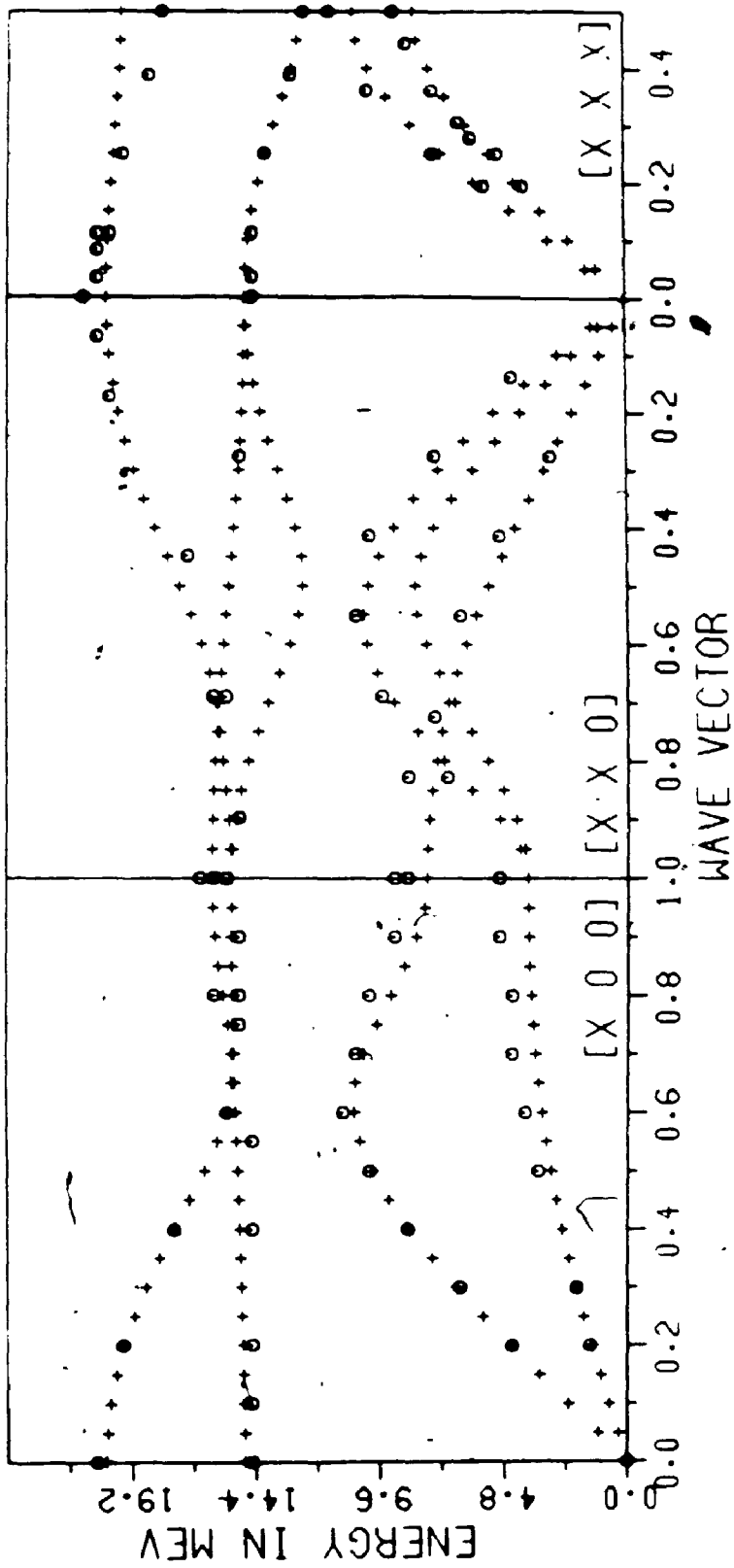


Figure 2-2: Phonon dispersion curves for KCl. = experimental⁴⁹, + calculated

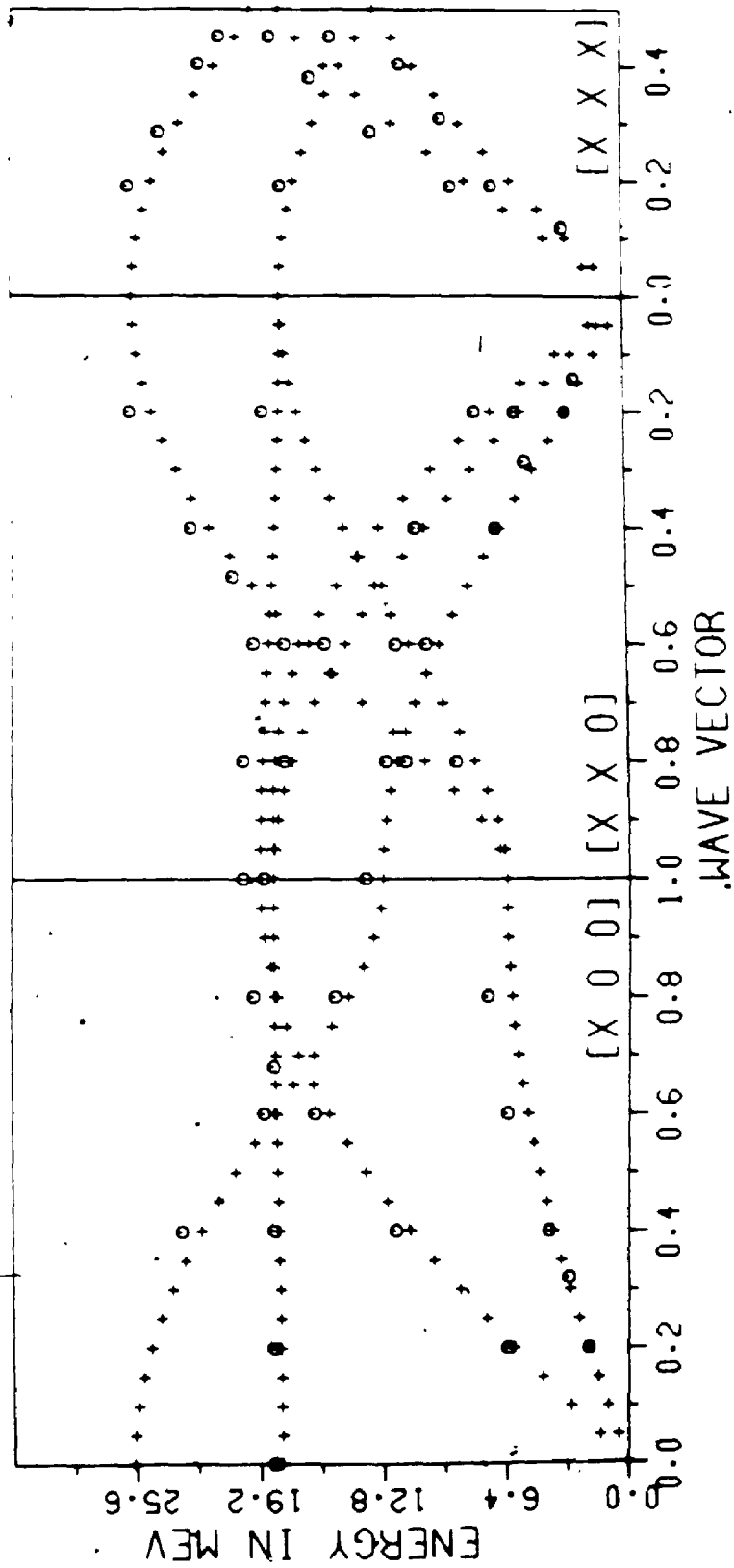


Figure 2-3: Phonon dispersion curves for KBr, \circ experimental⁵⁰, + calculated

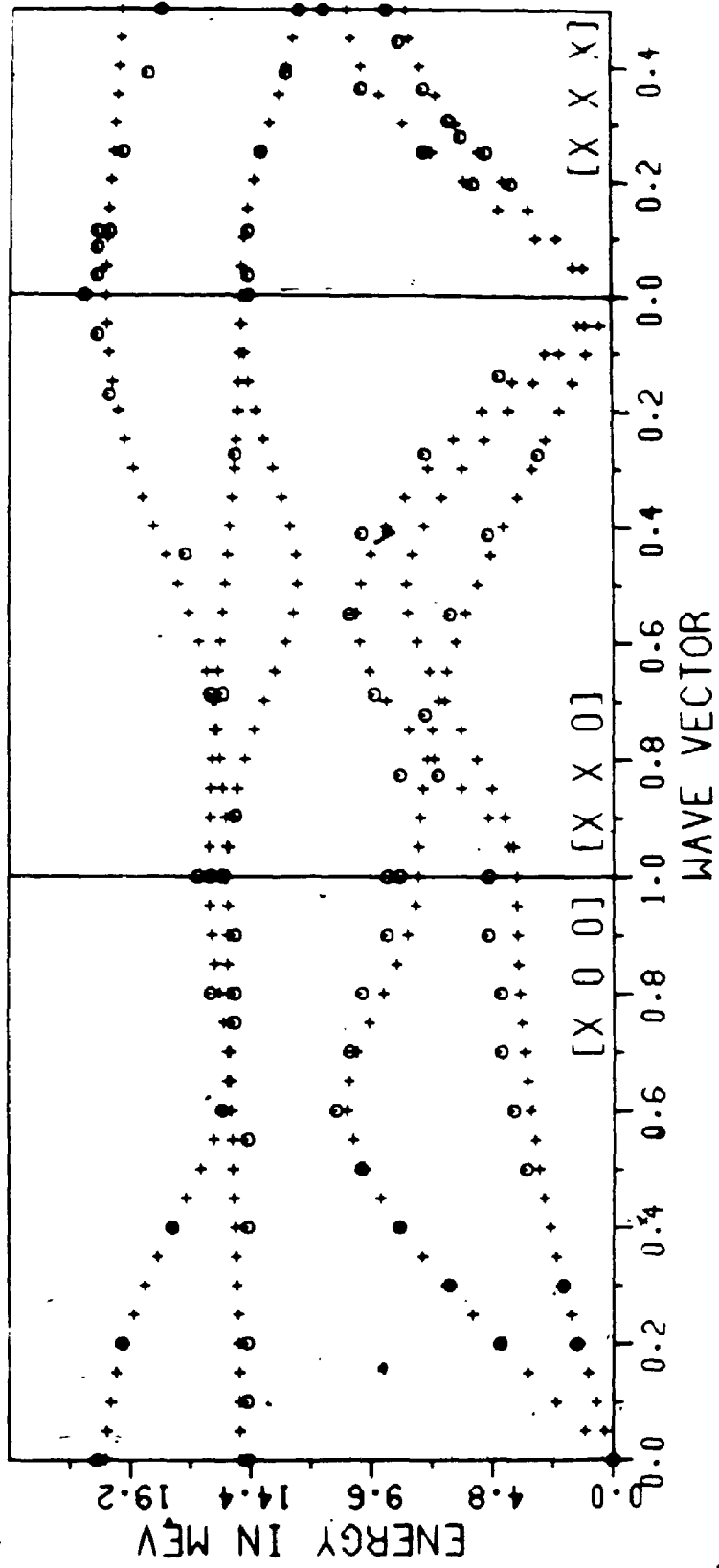
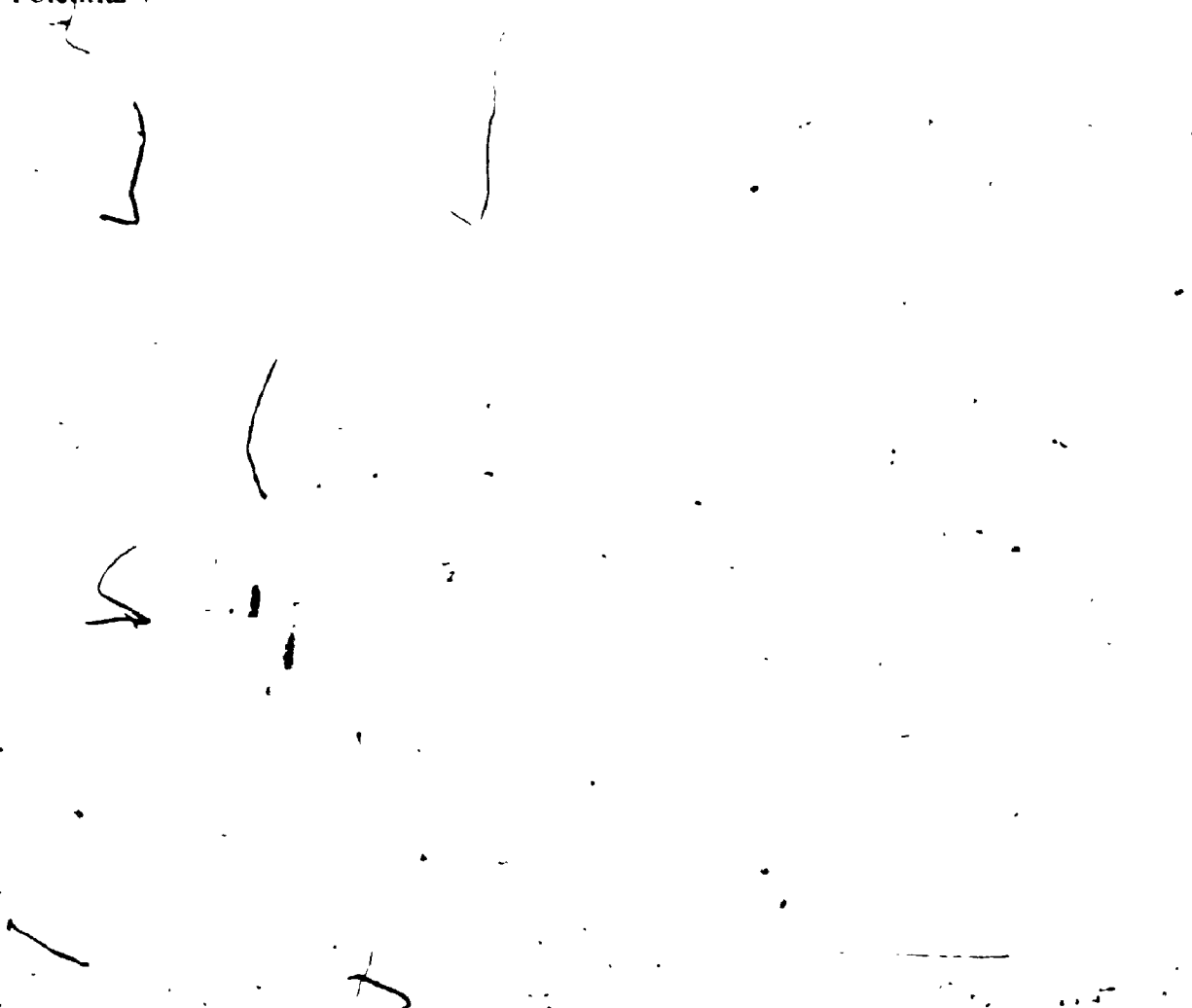


Figure 2-4: Phonon dispersion curves for Na_2S . \circ experimental⁵⁵; + calculated from Potential 4



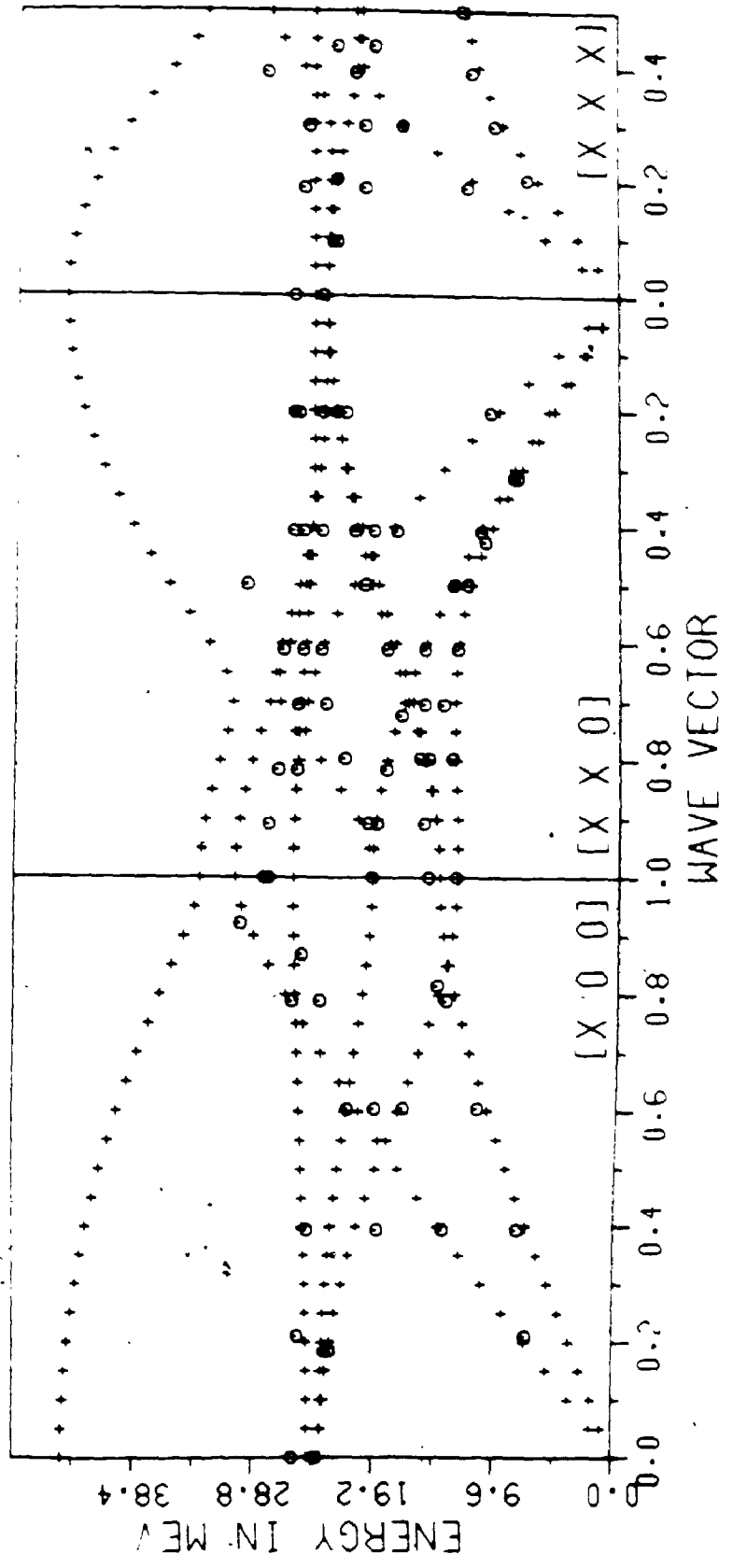


Figure 2-5: SrCl_2 lattice parameters⁶⁰

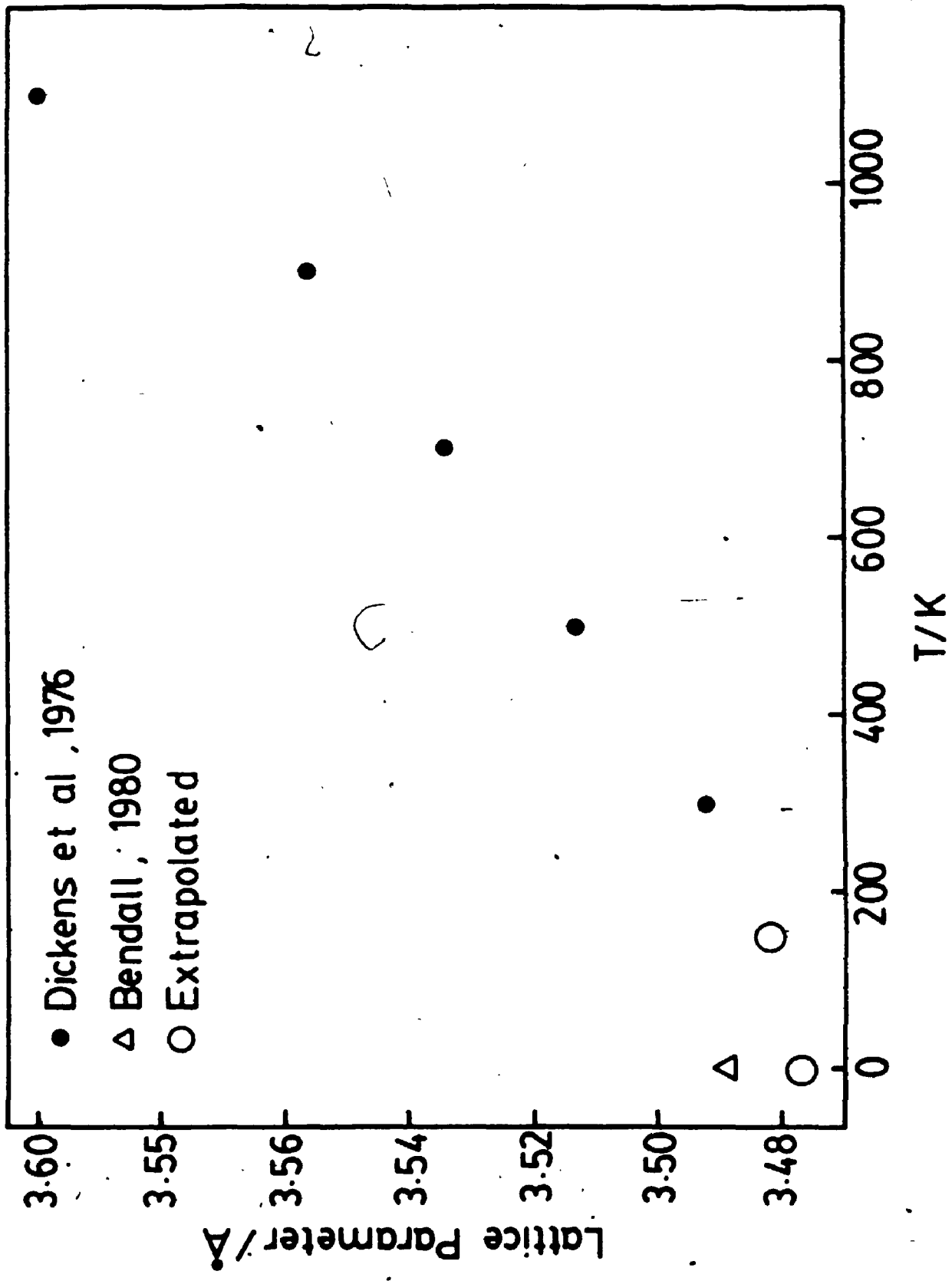


Figure 2-6: Phonon dispersion curves for SrCl_2 . \circ experimental⁶³, + calculated from Potential A3

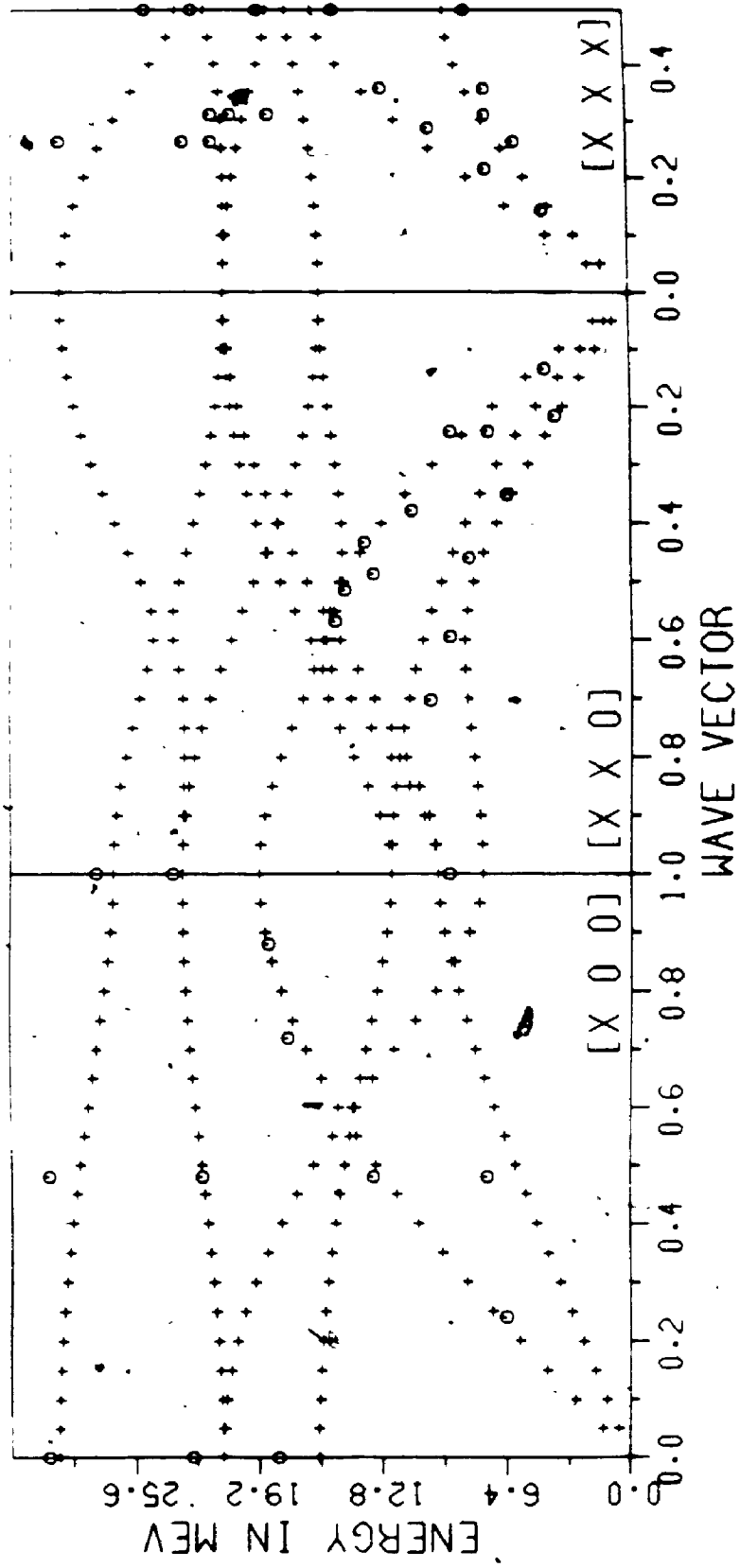
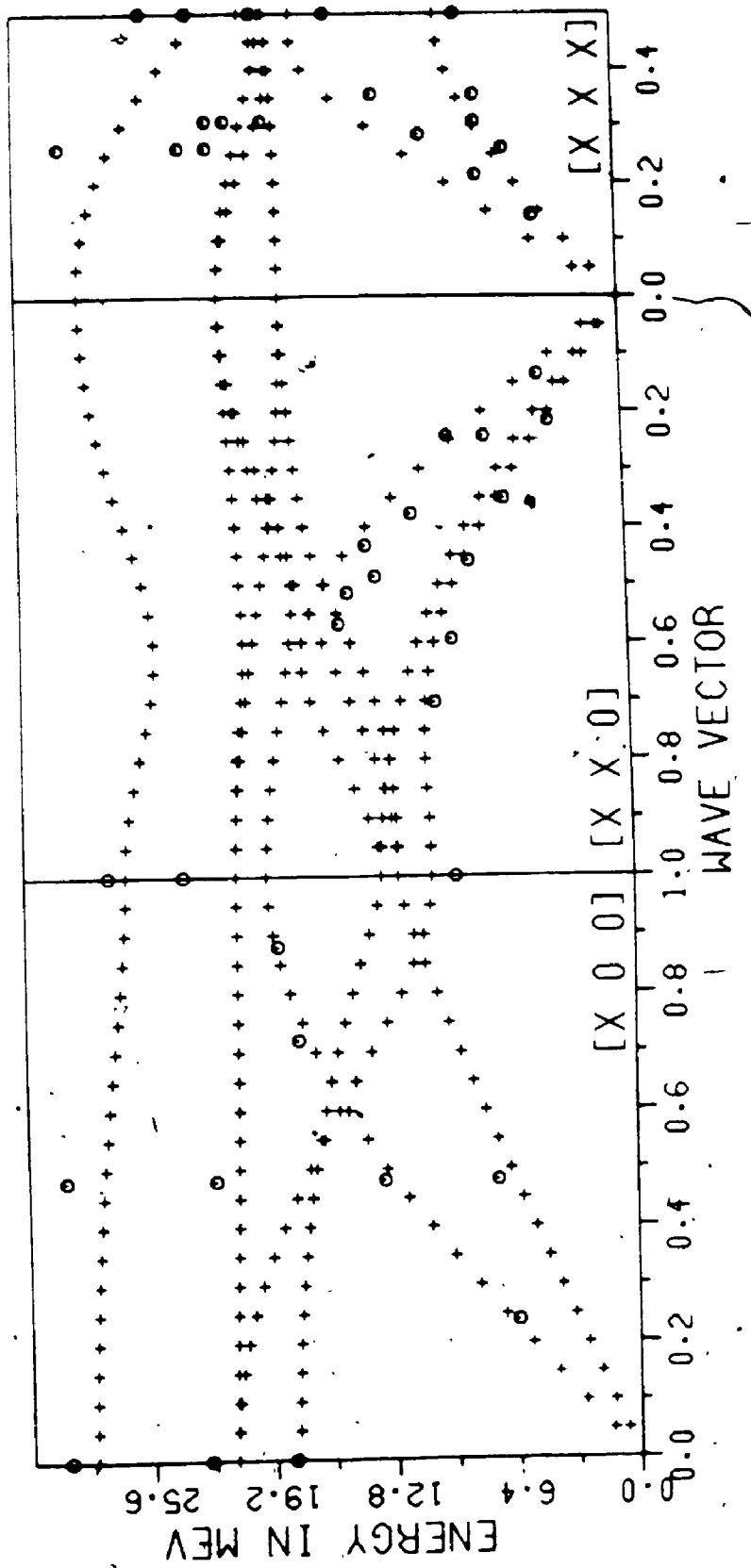


Figure 2-7: Phonon dispersion curves for SrCl_2 , \circ experimental⁶³, + calculated from Potential B1



Chapter Three

Sodium Sulphide Defect Energy Calculations

3.1. Introduction

Sodium sulphide possesses the anti-fluorite structure. The sodium ions occupy the corners of cubes and sulphur ions are positioned at the centre of every other cube. A diagram of the structure is given in Figure 3-1. Interest in Na_2S arose from the fact that it is a fast-ion conductor. A limited amount of experimental work has been carried out on this substance but there have been no previous defect calculations on Na_2S . The primary purpose of this investigation was to develop a sodium-sulphide potential for impurity calculations in NaCl; however, the availability of this potential meant that additional calculations on Na_2S itself could also be completed.

The ionic conductivity of sodium sulphide has been investigated by Möbius *et al*⁶⁸, who carried out ionic conductivity and diffusion experiments on pressed pellets of Na_2S . The conductivity was measured over a temperature range of approximately 1100 K to 600 K on pure Na_2S and on samples doped with sodium chloride. The radioactive isotopes ^{22}Na and ^{35}S were used in the diffusion experiments. The experimental values of the Arrhenius energies determined by Möbius *et al* are 1.657 eV from diffusion of Na^+ and 1.169 eV from diffusion of S^{2-} .

The experimental Arrhenius energy from conductivity measurements is given by,

$$E = -k \frac{d \ln \sigma T}{dT^{-1}} \quad (1)$$

The corresponding equation from diffusion measurements is,

$$E = -k \frac{d \ln D}{dT^{-1}} \quad (2)$$

The calculated Arrhenius energy for a particular mechanism involving defect r is one-nth the formation energy of the n defects that include r , plus the migration energy for defect r by the specified mechanism.

53

The lattice dynamics work gives supporting evidence for the high ionic conductivity of Na_2S . Bührer and Bill⁵⁷ suggested that large interstitial cavities in the lattice enable the formation of Frenkel defects with minimal distortion to the host lattice. They also proposed that the large thermal vibrations (the mean square displacement of Na^+ being 0.175 \AA^2 at 1000 K) favours the creation of defects.

Defect calculations were carried out using the HADES program. This program has been described elsewhere⁶⁹ and therefore will be discussed only very briefly here. This program employs the Mott-Littleton procedure to calculate the minimum energy configuration of the defect and the surrounding lattice. The lattice is divided into two regions. Region I is the volume immediately surrounding the defect and it consisted of approximately 100 ions in the present calculations. The ion interactions in this region are treated explicitly and the position coordinates of these ions are the variables in the minimization procedure. Region II is the outer region containing approximately 1000-1500 ions and is treated as a dielectric continuum. Displacements of the ions are matched at the boundary between Regions I and II to ensure continuity. The calculations were done on the Cyber 170/825 and the Cyber 170/835 main-frame computers.

3.2. Sodium Sulphide Defect Calculations

Defect calculations were carried out on all four potentials at 50 K and room temperature (the only two temperatures at which the lattice constant has been measured) and these values are listed in Table 3-2. Definitions of the defect energy symbols and their units are given in Table 3-1. Although the absolute magnitude of the defect energies differs for each of the potentials, the relative trends in energies are similar. Since the cation Frenkel formation energy is less than the Schottky formation energy, it may be assumed that the predominate defects are cation Frenkel defects in agreement with the conclusions of Bührer and Bill⁵⁷. These calculations also indicate that the main carriers are cation vacancies since this migration energy is lower than that for the cation interstitials. The anion Frenkel formation energy is significantly higher than either the

34

Schottky or cation Frenkel migration energies, as would be expected considering the relative sizes and charges of the two ions.

The Arrhenius energies were calculated for each of the possible transport mechanisms in order to compare them with the experimental results of Möbius *et al*⁶⁸. These values are listed in Table 3-3. The experimental value for the Arrhenius energy for the cation migration agrees most favourably with the migration of single cation vacancies derived from Schottky defects, although the calculated Arrhenius energy for vacancies from Frenkel defects is lower. This point is discussed below.

The defect formation energy can be determined from the experimental results by assuming that the Arrhenius energy in the high temperature region is equal to one-third the Schottky formation energy or one-half the Frenkel formation energy plus the migration energy and that the low temperature Arrhenius energy is equal to just the migration energy. This procedure assumes a dominant transport mechanism and neglects association in the extrinsic region. It yields a value of 1.77 eV for the formation energy which is in fairly good agreement with the calculated value of 1.85 eV for the cation Frenkel formation energy and much lower than the Schottky defect formation energy of 4.69 eV. This indicates that the difference in the experimental and calculated values for the Arrhenius energy lies in the cation vacancy migration energy which is 0.772 eV and 0.225 eV for the experimental and calculated (Potential 4, 50 K) values respectively. Low calculated migration energies are not uncommon with the fluorite structure and this problem also exists with the anion vacancy and interstitial migration energies for the fluorites³. The suggestion that the conductivity mechanism consists of the migration of cation vacancies arising through the formation of cation Frenkel defects may therefore be valid, despite the large differences between the calculated and experimental migration energies. The experimental value will include a contribution from the association of cation vacancies with substitutional Cl^- ions and so the true experimental migration energy is somewhat lower than 0.772 eV.

The anion results differ markedly from the experimental values. Therefore, additional calculations were carried out for vacancy complexes in order to gain some insight into a possible migration mechanism. Potential 4 was used for these calculations since the previous calculations using this potential yielded the results in best agreement with the literature values.

The energy required for jumps into vacancy pairs and triplets was calculated. Figure 3-2a is a diagram of a vacancy pair and Figure 3-2b shows the saddle point for the anion jump into the pair. The cation jump into the pair was calculated as well and a diagram of the saddle point is given in Figure 3-2c. The vacancy triplet configuration is shown in Figure 3-3a and diagrams of the anion and cation saddle points are given in Figures 3-3b and 3-3c respectively. In the calculation for the cation jump into the triplet (a), the moving cation relaxed into vacancy 1 in (c), yielding the more stable triplet configuration shown in Figure 3-3d. The calculated defect energies for both configurations are given in Table 3-4. The migration of the triplet defect requires a series of cation and anion jumps.

These calculations on vacancy clusters did not yield results any closer to the experimental values. The Arrhenius energies are listed in Table 3-1 and the defect energies are given in Table 3-4. The triplet energy was actually significantly higher than that for the single vacancy but the pair energy was only slightly higher. Therefore, it would not be possible to distinguish between anion conductivity arising through the migration of single vacancies and conductivity arising through anion vacancy jumps into the pairs. A vacancy pair mechanism for charge migration in fluorites requires successive anion and cation jumps but $\Delta H_{ap} \gg \Delta H_{cp}$ so that anion jumps will be rate determining. It is surprising that the experimental Arrhenius energy for the anion migration would be this low, and in fact lower than that of the cation, since the anion is significantly larger than the cation and carries twice the charge and one would therefore expect it to be less mobile.

3.3. Monovalent Anion Impurity Calculations

Energies of solution of chloride ions in Na_2S were also calculated for various mechanisms. Five different modes of solution were investigated. In the first case, the monovalent anion entered as an interstitial accompanied by a sodium interstitial, secondly the impurity anion occupied a substitutional site with charge compensation by either a sodium vacancy or a monovalent anion interstitial, alternatively the impurity ion might enter as an interstitial with charge compensation by a sulphide vacancy or finally it might occupy a substitutional site with sulphide interstitial charge compensation. The energies of solution for each of these mechanisms are given by the following equations:

$$E_1 = E(\text{Cl}_i^-) + E(\text{Na}_i^+) - E_c(\text{NaCl}) \quad (3)$$

$$E_2 = E(\text{Cl}_s^-) + E(\text{Na}_v^+) + E_c(\text{Na}_2\text{S}) - E_c(\text{NaCl}) \quad (4)$$

$$E_3 = (1/2)E(\text{Cl}_s^-) + (1/2)E(\text{Cl}_i^-) - E_c(\text{NaCl}) + (1/2)E_c(\text{Na}_2\text{S}) \quad (5)$$

$$E_4 = E(\text{Cl}_i^-) + (1/2)E(\text{S}_v^{2+}) - E_c(\text{NaCl}) + (1/2)E_c(\text{Na}_2\text{S}) \quad (6)$$

$$E_5 = E(\text{Cl}_s^-) + (1/2)E(\text{S}_i^{2-}) - E_c(\text{NaCl}) + (1/2)E_c(\text{Na}_2\text{S}) \quad (7)$$

where the subscripts i, v, and s refer to interstitial, vacancy, and substitutional respectively and E_c is the cohesive energy. Values of the energy of solution, calculated for each of these mechanisms, using Potential 4 at 0 K and room temperature, are listed in Table 3-5. The 0 K TD sodium-chloride potential and the electron-gas chloride-sulphide potential were used to describe the interactions between the impurity and the host lattice. The results indicate that the mechanism whereby the impurity anion enters on both substitutional and interstitial sites is the most favourable energetically.

The binding energies for each of the complexes, shown in Figure 3-4, formed by the addition of the monovalent anion were also calculated and these values are listed in Table 3-5. The only significant displacement on relaxation occurred for the $(\text{Cl}_i^- \text{Cl}_s^-) \langle 100 \rangle$ complex. In this case, the complex ions moved approximately 0.1 lattice units in the direction of the empty cell. The binding energies for the complexes once again favour the substitutional impurity-interstitial impurity nearest-neighbour complex.

Mobius *et al.*⁶⁸ suggested that chloride ions would go into solution in sodium sulphide via the second mechanism whereby the chloride would substitute for a sulphide ion and this would be accompanied by the formation of a sodium vacancy. This same discrepancy in the mode of solution occurs in the fluorites since it was determined experimentally that a monovalent cation would occupy a regular cation site in strontium chloride and this would be accompanied by the formation of an anion vacancy⁷⁰ However, calculations by Bendall and Catlow³ indicated that a mechanism corresponding to the third mode above, would occur

This discrepancy in the mode of solution between the experimental and calculated results led to an investigation into an alternate conduction mechanism, that is the migration of monovalent anion interstitial impurities. But, the activation energy for the migration of chlorine interstitials proved to be too high to be of any consequence, as indicated in Table 3-4, so that this mechanism would not make a significant contribution to the conductivity. The energy required to form the $(\text{Cl}_i^- \text{Cl}_i^-) <100>$ complex saddle point for the reorientation shown in Figure 3-4, is much lower; however, this would not lead to an alternative migration mechanism. The calculated values are therefore not in agreement with the results of doping on conductivity, a problem similar to that of sodium-doped SrCl_2 ³. If the $(\text{Cl}_i^- \text{Cl}_i^-) <100>$ complexes do indeed exist then the reorientation of these complexes would lead to an ionic thermocurrent (ITC) peak with an activation energy of about 0.47 eV

3.4. $\text{NaCl}:\text{S}^{2-}$ Defect Calculations

Calculations were also carried out for the substitution of a sulphide ion on a regular chloride ion site in sodium chloride. These calculations had not been attempted previously and although there are no experimental data with which to compare the results, the calculations might give some insight into the migration mechanism by providing values for the association energies.

The binding energies for complexes involving an impurity ion and an anion vacancy on nearest-neighbour $nn \langle 110 \rangle$ or second neighbour $nnn \langle 200 \rangle$ sites were calculated. EPR studies by Watkins⁷¹ on Mn^{2+} -doped NaCl had suggested the possibility of the existence of the analogous cation complexes. Calculations on alkaline-earth cations in sodium chloride, potassium chloride, and potassium bromide have been carried out and this work confirms the possibility of the existence of the cation complexes⁷².

The present calculations were carried out using Potential 4 for the sodium-sulphide interaction and the TD potentials at 0 and 800 K for the sodium chloride potentials. The electron-gas potential was used for the sulphide-chloride interaction. The binding energies are listed in Table 3-6. Diagrams of the complexes are given in Figure 3-5. The results indicate that the nearest-neighbour complex is the more stable configuration.

The activation energies for the four kinds of vacancy jumps around the impurity were also calculated and these values are given in Table 3-6. The w_1 jump involves the migration of an anion vacancy from a nearest-neighbour position to another nearest-neighbour position, the w_3 jump involves the migration of a vacancy from a second neighbour site to a nearest-neighbour site and w_4 jump is the reverse. A w_2 jump is the migration of a vacancy into the impurity site. Diagrams of the jumps are given in Figure 3-5.

The activation energy for the w_2 jump is similar to the values obtained for the divalent cation⁷² as would be expected from the structure of sodium chloride and the similar sizes of the impurity ions. The activation energies for the other jumps follow the same trends exhibited by sodium chloride containing a divalent cation impurity. Δu_1 is the activation energy for the reorientation of the S^{2-} -cation vacancy complexes which would be observed in ITC or dielectric loss experiments. These experiments are usually done at relatively low temperatures where the precipitation of Na_2S would probably reduce the concentration of the complexes to a negligible amount. Cook and Dryden³²

measured dielectric loss on S^{2-} -doped NaCl but failed to find any evidence for the complexes, probably for the above reason. The value for $\Delta\mu_2$ corresponds to the diffusion of S^{2-} ions in NaCl, however, no such measurements have been reported as yet.

Table 3-1: Defect energy symbols

Defect	Energy	Arrhenius Energy
Schottky formation	u_S	
Anion Frenkel formation	u_{F_A}	
Cation Frenkel formation	u_{F_C}	
Cation vacancy migration	Δu_{cv}	E_{cv}
Anion vacancy migration	Δu_{av}	E_{av}
Cation interstitial migration	Δu_{ci}	E_{ci}
Anion interstitial migration	Δu_{ai}	E_{ai}
Vacancy pair association	u_{vp}	
Cation jump into pair	Δu_{cp}	E_{cp}
Anion jump into pair	Δu_{ap}	E_{ap}
Vacancy triplet association	u_{vt}	
Cation jump into triplet	Δu_{ct}	E_{ct}
Anion jump into triplet	Δu_{at}	E_{at}
Impurity-vacancy nn complex	u_1	
Impurity-vacancy nnn complex	u_2	
w_1 jump	Δu_1	
w_2 jump	Δu_2	
w_3 jump	Δu_3	
w_4 jump	Δu_4	

Superscripts S and F indicate that the mobile vacancy originated from a Schottky or Frenkel defect respectively.

Table 3-2: Formation and migration energies for Na₂S

Defect	50 K				Room Temperature			
	1	2	3	4	1	2	3	4
u_S	4.06	5.34	5.53	4.78	3.97	5.21	5.41	4.69
u_{Fe}	1.82	2.15	2.11	1.87	1.80	2.12	2.08	1.85
u_{Fa}	6.81	8.35	7.52	6.09	6.59	8.08	7.28	5.92
Δu_{Cu}	0.26	0.36	0.40	0.23	0.25	0.34	0.39	0.23
Δu_{Sv}	2.31	2.82	2.62	2.11	2.29	2.79	2.61	2.10
Δu_{Cu}	0.43	0.61	0.63	0.56	0.41	0.58	0.61	0.54
Δu_{Sv}	3.32	3.99	4.04	2.83	3.29	3.95	4.00	2.82

Table 3-3: Arrhenius energies for Na_2S

Energy	Value
E_{cv}^S	1.79
E_{cv}^F	1.15
E_{ci}	1.46
E_{cp}	2.54
E_{ci}	-
E_{av}^S	3.67
E_{av}^F	5.06
E_{μ}	5.78
$E_{\mu p}$	3.68
$E_{\mu t}$	4.56

Table 3-4: Impurity complex and migration energies for Na₂S calculated using Potential 4 at 50 K

Defect	Energy
u_{cp}	-1.25
Δu_{cp}	0.75
Δu_{ap}	1.80
u_{ct}	-1.80 ^a , -2.06 ^d
Δu_{ct}	-
Δu_{at}	1.53

a refers to configuration (a) in Figure 3-3

d refers to configuration (d) in Figure 3-3

Table 3-5: Energies of solution, binding energies and impurity migration energies for Na₂S:Cl⁻ complexes

	50 K	Room Temperature
Defect Energies:		
E(Na _i ⁺)	-1.69	-1.72
E(Na _v ⁺)	3.56	3.57
E(S _i ²⁻)	-13.98	-14.04
E(S _v ²⁻)	20.07	19.97
E(Cl _i ⁻)	-3.65	-3.69
E(Cl _s ⁻)	12.66	12.62
Cohesive Energies:		
E _c (NaCl)	-8.03	-7.94
E _c (Na ₂ S)	-22.34	-22.34
Energies of Solution:		
Mode of Solution		
E ₁	2.60	2.53
E ₂	1.81	1.79
E ₃	1.27	1.23
E ₄	3.15	3.06
E ₅	2.43	2.37

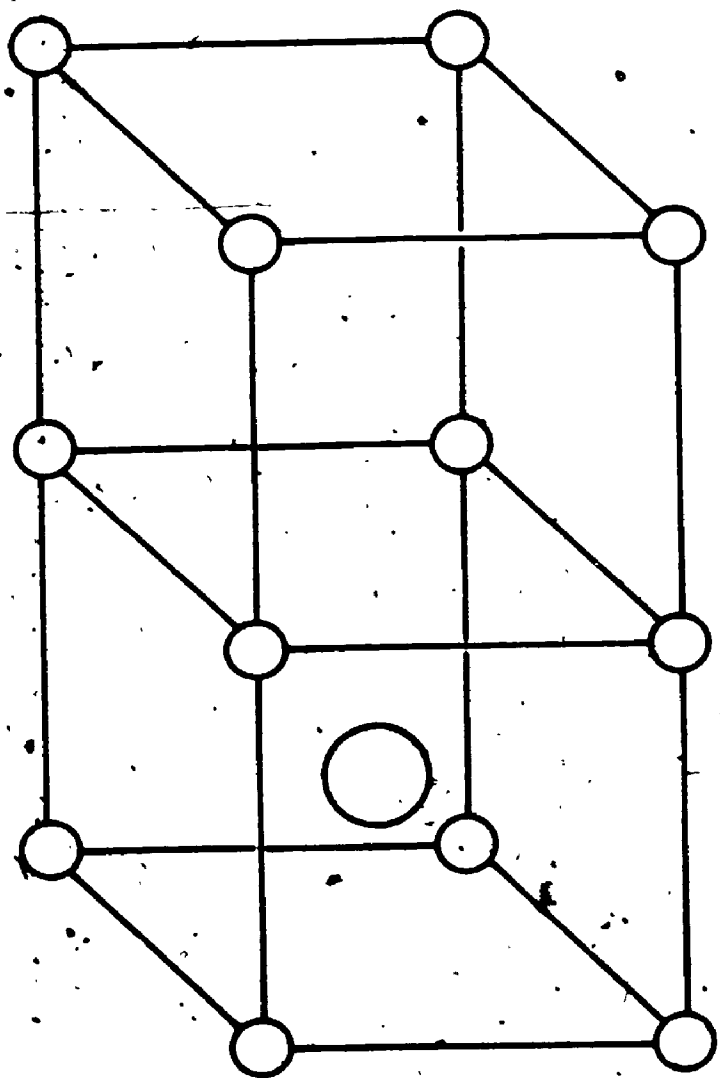
Table 3-5: cont

	50 K	Room Temperature
Binding Energies:		
Complex		
$(Cl_5^- Na_1^+) <111>$	-0.672	-0.651
$(Cl_5^- Cl_1^-) <100>$	-0.865	-0.842
$(Cl_5^- Cl_1^-) <111>$	-0.343	-0.336
$(Cl_1^- Na_1^+) <110>$	-0.433	-0.419
Migration Energy:		
Cl_1^-	2.78	2.73
Reorientational Energy:		
$(Cl_5^- Cl_1^-) <100>$	0.47	0.47

Table 3-6: NaCl.S²⁻ binding energies and vacancy jump energies

Defect Energy	0 K	800 K
u_1	-0.632	-0.475
u_2	-0.446	-0.371
Δu_1	0.679	0.520
Δu_2	0.863	0.856
Δu_3	0.590	0.468
Δu_4	0.776	0.572

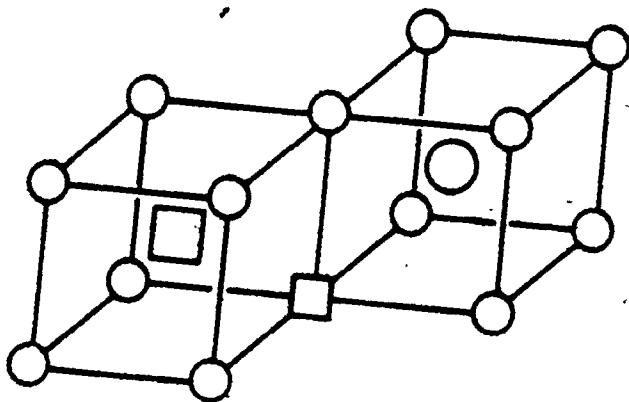
Figure 3-1: Structure of Na_2S



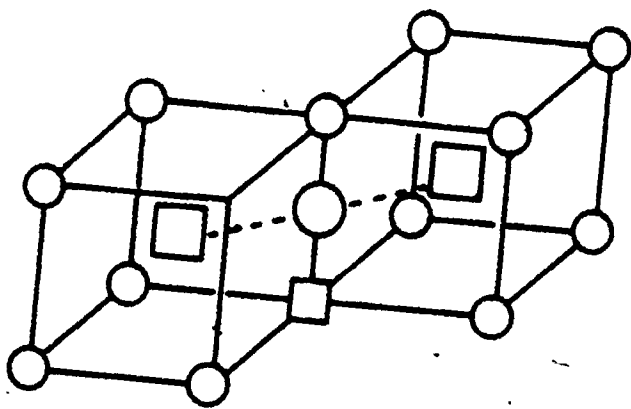
○ Na⁺

○ S²⁻

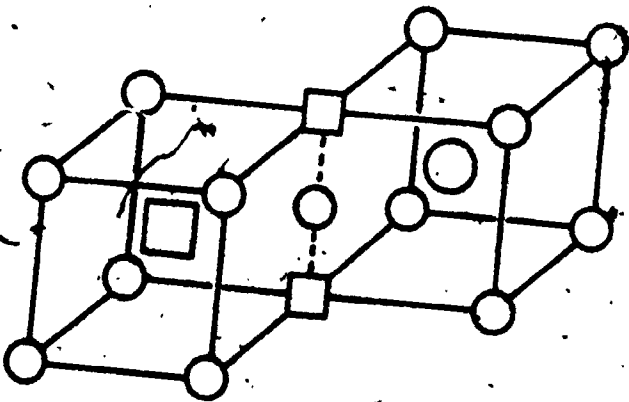
Figure 3-2: Vacancy pair in Na_2S (a) structure, (b) anion saddle point, (c) cation saddle point



a

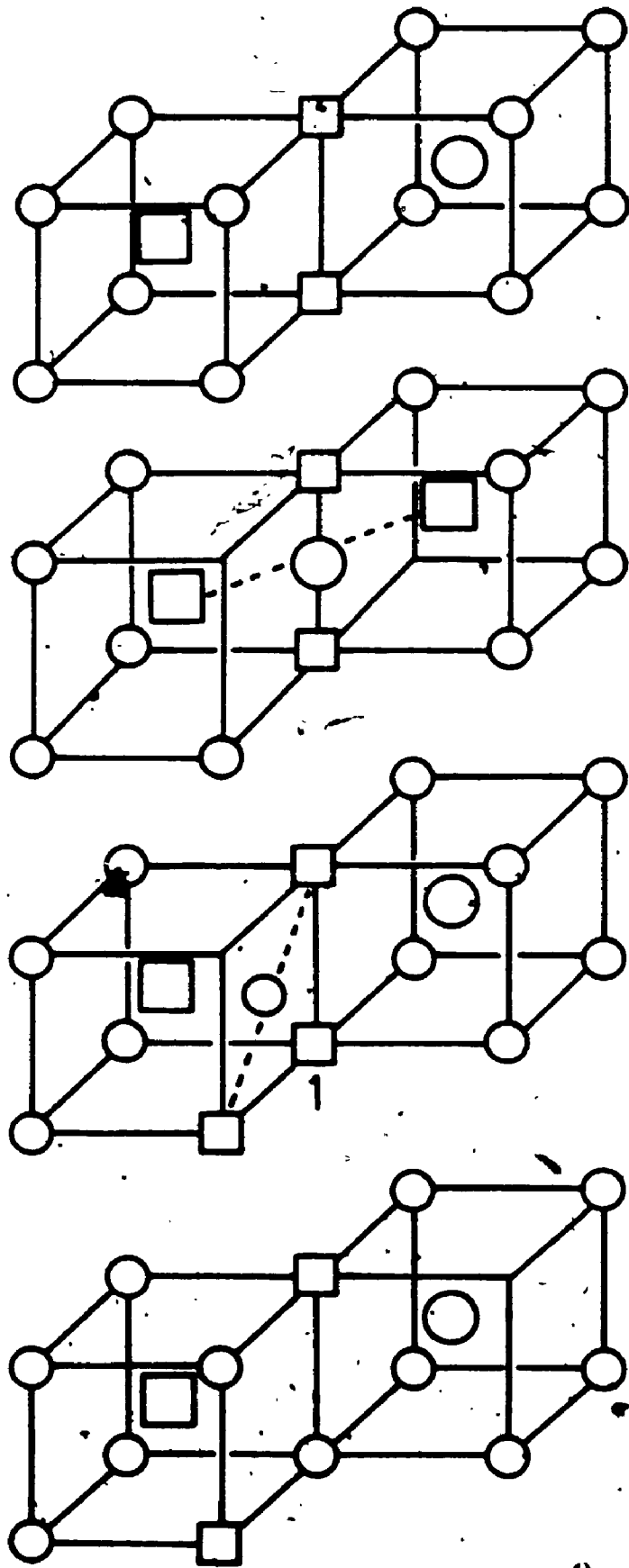


b



c

Figure 3-3: Vacancy triplet in Na_2S . (a) structure, (b) anion saddle point, (c) cation saddle point, (d) most stable configuration



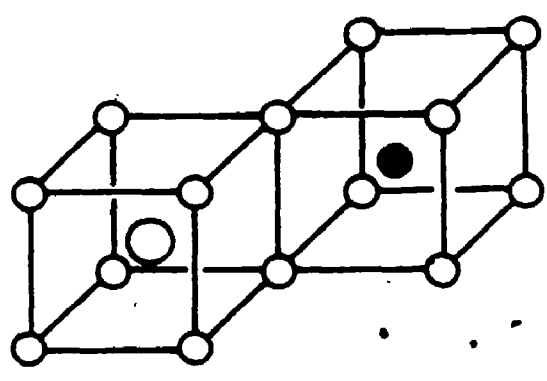
α

β

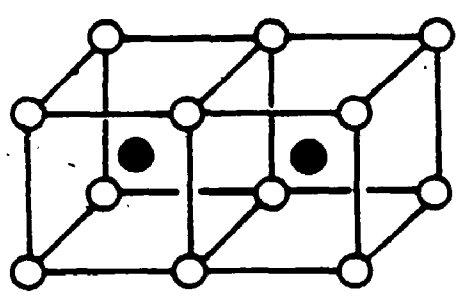
γ

δ

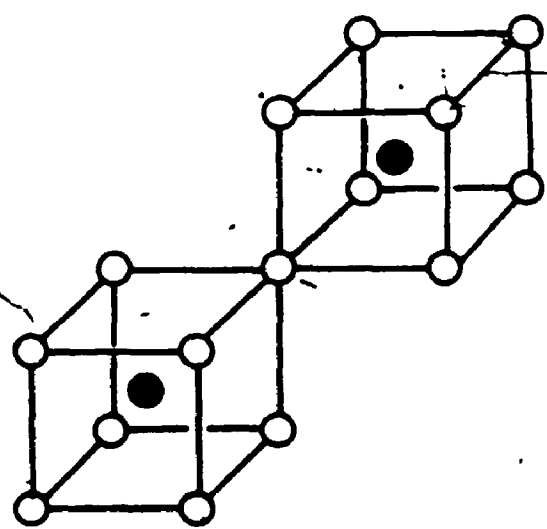
Figure 3-4: $\text{Na}_2\text{S}\cdot\text{Cl}^-$ complexes



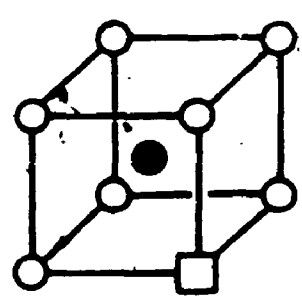
$(Na^+ Cl^-) \langle 110 \rangle$



$(Cl_s^- Cl_i^-) \langle 100 \rangle$



$(Cl_s^- Cl_i^-) \langle 111 \rangle$



$(Na^+ Cl_s^-) \langle 111 \rangle$

$(Cl_s^- Cl_i^-) \langle 100 \rangle$
sp

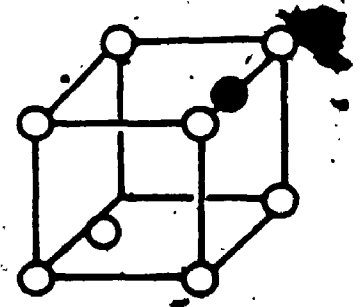
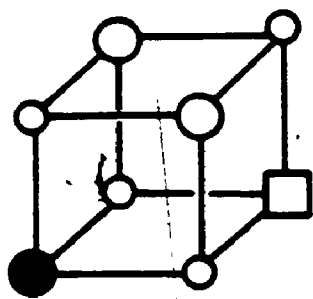
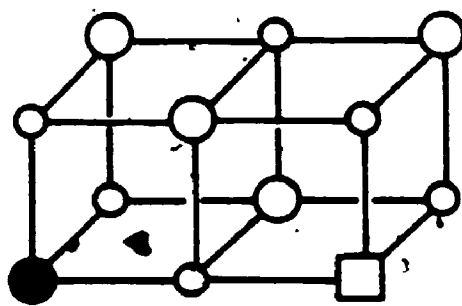


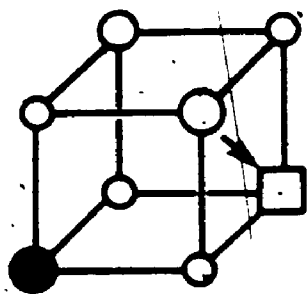
Figure 3-5: $\text{NaCl}:\text{S}^{2-}$ complexes and vacancy jumps



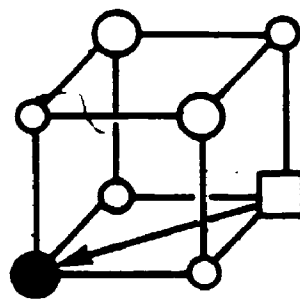
nn



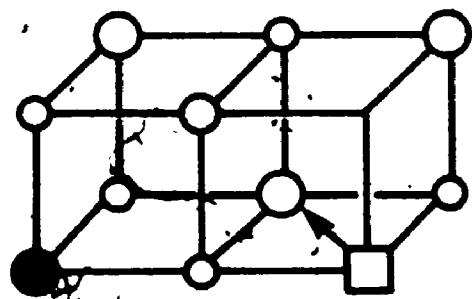
nnn



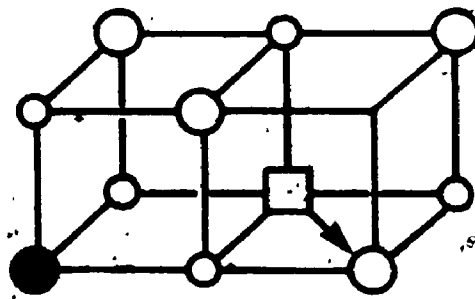
w₁



w₂



w₃



w₄

Chapter Four

Strontium Chloride Defect Calculations

4.1. Introduction

Strontium chloride possesses the fluorite structure shown in Figure 4-1. Chlorine ions occupy the corners of the cubes and strontium ions are located in the centre of alternate cubes. Strontium chloride exhibits fast-ion conduction at high temperatures and its conductivity has been investigated by several groups, most recently by Chadwick *et al.*⁷⁰ and Jacquet⁷³ (also see references therein). They have carried out conductivity experiments on pure and M^+ - and M^{3+} -doped $SrCl_2$ and defect energies derived from these results are tabulated in Table 4-1. The conductivity of strontium chloride has been attributed to the motion of anion vacancies which arise through the formation of Frenkel defects.

Defect calculations have also been carried out on pure and doped $SrCl_2$ by Bendall and Catlow³. Their values for defect energies are also listed in Table 4-1. The calculated value for the anion Frenkel formation energy is in good agreement with Chadwick *et al.*⁷⁰ however, their anion vacancy and interstitial migration energies are lower than the experimental values.

The present investigation was undertaken in order to develop a strontium-chloride potential for use in calculations on sodium chloride containing strontium ions. Some defect energies were also calculated in order to test the potentials. These calculations were not extensive and did not involve an investigation into the fast-ion conduction of strontium chloride⁷⁴. The HADES program described in Section 3.1 was used.

4.2. Defect Calculations

Schottky and anion Frenkel defect formation energies, and anion vacancy and interstitial migration energies were calculated for the final potentials at 0 K. Further calculations were carried out at 900 K and 1100 K in order to select the best A potential. The defect energies were sensitive to the potential as can be seen from the results listed in Table 4-2. Fitting c_{11} resulted in a value for the anion Frenkel formation energy in good agreement with the experimental value, however the migration energies were low. Potential A2, which was derived by preferentially fitting the optic and Raman frequencies, gave good values for the migration energies but the anion Frenkel formation energy was too high. The potential which was a compromise of these two, A3, was therefore used in the subsequent calculations. The cation Frenkel formation energy and the cation vacancy and interstitial migration energies were also calculated using Potentials A3 and B1 and these values are included in Table 4-2.

Defect energies were calculated at all three temperatures using Potential B1 in order that the effect due to a change in lattice constant could be determined. It is best to compare the defect energies calculated using potentials A3 and B1 since their fitting procedures were the most similar. The defect energies were quite close in value, however the results from Potential B1 were actually better since the anion Frenkel formation energy is lower than that obtained using Potential A3 and the anion vacancy and interstitial migration energies are higher. It cannot be stated for certain that this improved potential is a result of fitting the potential to a different lattice constant. The defect energies are very sensitive to the potential parameters and this may be the cause of improved defect energies. Table 2-15 shows that Potential B1 gives a better fit to the physical properties of the crystal.

The present results support the model in which the conductivity arises from the presence of anion Frenkel defects with anion vacancies being the more mobile species.

The calculated anion Frenkel formation energy was slightly higher than the experimental value of Chadwick *et al.*⁷⁰ and the anion vacancy migration energy was lower. The anion interstitial migration energy was much lower than the value determined by this group, but higher than the value determined by Bendall and Catlow³. The calculated values were in much better agreement with the results of Jacquet⁷³ since his value for the anion Frenkel formation energy was higher than that of Chadwick *et al.* and his migration energies were lower. However, the calculated value for the anion interstitial migration energy was still lower than the experimental. A low value for the anion interstitial migration energy is a common problem with calculations on crystals possessing the fluorite structure as mentioned previously in Section 3.2.

4.3. Monvalent Impurity Defect Calculations

Calculations for sodium ions occupying interstitial and substitutional sites in SrCl_2 are also of interest and have been carried out by Bendall and Catlow³. They determined that the sodium ions would preferentially go into solution by occupying both interstitial and substitutional positions contrary to the conclusions of Chadwick *et al.*⁷⁰, who suggested from their experiments that impurity ions would occupy substitutional lattice sites, charge compensation taking the form of chloride vacancies. Jacquet⁷³ also suggested that this latter mode of solution would occur and determined an energy of solution of 1.2 ± 0.1 eV. Bendall and Catlow suggested this difference might be explained by an equilibrium between the two modes. Gervais *et al.*⁷⁵ had suggested that an equilibrium between substitutional impurity ions and interstitial impurities and strontium vacancies might also be occurring. By considering a mass action treatment of the defect equilibria, Bendall and Catlow determined the distribution of defects as a function of dopant concentration and temperature. This led them to suggest that at lower temperatures, the equilibrium between the two modes of solution becomes important and charge compensation by impurity interstitials might occur (See Figure 1, Bendall and Catlow³).

Similar calculations have been carried out using potentials A3 and B1 for the SrCl_2 interactions, the 0 K TD potential for the sodium-chloride interaction, and the electron-gas potential for the strontium-sodium interaction. The energies of solution for modes analogous to those described in Section 3.3 for sodium sulphide were calculated at 0 and 900 K and the results are tabulated in Table 4-3. Although the energies of solution differ slightly from the previous calculations, the same trends were observed. The binding energies for each of the complexes were also calculated and once again the $(\text{Na}_5^+ \text{Na}_1^+) <100>$ complex was the most stable. These values are listed in Table 4-3. The structures of these complexes are the same as the corresponding complexes for Cl^- impurities in Na_2S (Figure 3-4).

The tendency for the ions to move from the starting configuration when the crystal was relaxed was more pronounced for SrCl_2 than Na_2S , since it was possible to carry out the SrCl_2 calculations at higher temperatures. This was particularly apparent in the $(\text{Na}_5^+ \text{Na}_1^+) <100>$ complex. The magnitude of this displacement was temperature dependent as indicated by Figure 4-2. In fact at room temperature, the substitutional ion has moved almost to the face of the adjoining empty cell and the interstitial ion is in the same cell, the distance between the two ions always being less than the cell length. Local minima must occur along the potential surface since the final coordinates were often dependent on the initial positions of the ions, especially at the intermediate temperatures. The positions plotted correspond to the lowest defect energies.

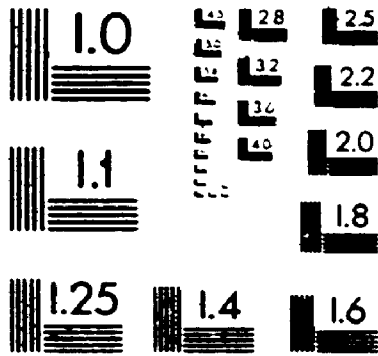
The impurity ion was never located at the centre of the cube, but moved along $<100>$ toward the adjacent face at a lower temperature when Potential B1 was used. The difference in the results from Potentials A3 and B1 can best be attributed to the difference in lattice constant. Bendall's value for the 0 K lattice constant and values interpolated between this 0 K value and the experimental results of Dickens *et al.*⁶¹ were used in the calculations employing B1. This resulted in a very small change in the lattice constant in

this temperature range. The lattice constants used for A3 in this temperature range were somewhat lower and showed a greater temperature dependence (see Figure 2-5).

The binding energy as a function of displacement from the cell centre was also calculated at 0 K and 900 K using both potentials A3 and B1. This was accomplished by fixing the substitutional impurity and allowing the interstitial and the other ions to relax. These results are plotted in Figure 4-3. The binding energy increases significantly as the defect approaches the cell centre but is very flat towards the cell face. The displacements observed for calculations with Potential B1 were greater than those using Potential A3 however the same general shape is observed for both potential plots at a given temperature. The shape of the plot varies with temperature as one would expect from the results of Figure 4-2. The change in potential energy from the centre of the cube to the face is less at 0 K than at 900 K. The minimum binding energy occurs at approximately 0.2 lattice units towards the cube face at 0 K. At 900 K, the minimum is located much closer to the cube face at approximately 0.4 lattice units from the cube centre.

As in the case of the calculations of Bendall and Carlow³, the results indicate that the mode whereby the impurity enters as both a substitutional and interstitial ion is the most energetically favourable, in disagreement with the experimental results. Additional calculations were carried out to determine whether some of the conductivity could be the result of the migration of sodium ion interstitials. As can be seen from the results listed in Table 4-3, the energy of migration of the interstitial is too high to make a significant contribution to the conductivity. The reorientational energy for the $(\text{Na}^+ \text{Na}^+)_{\langle 100 \rangle}$ complex is also listed in Table 4-3 and is in good agreement with the experimental value of 0.345 eV for the activation energy for Na^+ dipoles determined by Jacquet⁷³.

2



METRO

4.4. NaCl:Sr²⁺ Defect Calculations

The effect of divalent impurities in sodium chloride is of interest in this study and in particular the binding energies of the vacancy-impurity complexes and the activation energy of the vacancy jumps around the impurity. Calculations have been carried out by Catlow *et al.*⁷² on alkaline-earth cation containing alkali halide systems. They used the CDN² spline potentials for the alkali halides and electron-gas potentials to describe the interactions between the impurity ions and the host. As mentioned in Section 3.4, these dipolar complexes have been observed for Mn²⁺-doped potassium chloride using EPR.⁷¹

In the present investigation the TD potentials for sodium chloride at 0 K and 800 K were used along with the strontium-chloride Potentials A3 and B1 developed for the SrCl₂ structure and the strontium-sodium electron-gas potential. The final results are listed in Table 4.4. The structures of the complexes and the jump saddle points are analogous to those for the sulphide impurities (Figure 3-5). Considerable care was taken in determining the path for the w_{3,4} jump at 0 K using Potential B1. The lowest energy pathway was found to arc slightly away from the complex. The path at 800 K also deviated from a straight line. There was no significant displacement when Potential A3 was used. Catlow *et al.*⁷² had found that out-of-plane calculations for the w₂ jump resulted in higher saddle point energies and therefore this was not re-investigated.

The binding energies for the complexes are close to those of Catlow *et al.*⁷². The impurity-vacancy nearest-neighbour complex is the most energetically favourable although the energy difference is not substantial enough to rule out the presence of second neighbour complexes. The binding energies are in generally good agreement with the experimental results^{12, 13, 21}. If the binding energies for nn and nnn complexes are similar, both species will exist in equilibrium. Transport measurements do not distinguish between the type of complex and so yield an intermediate value for the binding energy.

The value for the w_1 jump is slightly lower than the experimentally determined value⁷⁶. The activation energies for the w_1 and w_3 jumps are lower than the other two jumps as would be expected since these represent the migration of the vacancy into the more stable complex configuration. The w_2 jump is higher because it involves the migration of a larger, doubly-charged impurity ion.

Table 4-1: Experimental and previously calculated defect values for SrCl₂

Defect	Experimental ^a	Experimental ^b	Calculated ^c
u_{F_1}	2.02	2.20	2.06
u_{F_2}	-	-	5.85
u_S	-	-	4.00
Δu_{uv}	0.35	0.30	0.24
Δu_{uu}	0.86	0.76	0.46

^a Chadwick *et al.*⁷⁰

^b Jacquet⁷³

^c Bendall and Catlow³

Table 4-2: Defect energies for SrCl₂

Defect	0 K						900 K			1100 K		
	A1	A2	A3	B1	A1	A2	A3	B1	A3	B1	A3	B1
u_S	3.54	5.76	4.41	4.58	2.87	4.58	3.60	3.93	3.13	3.47		
u_{Fc}			7.25	6.58			5.61	5.32	4.72	4.49		
u_{F_2}	2.28	2.96	2.47	2.23	1.91	2.57	2.08	1.96	1.87	1.78		
Δu_{cv}			2.31	2.69			2.06	2.46	1.91	2.28		
Δu_{sv}	0.10	0.26	0.17	0.25	0.03	0.18	0.09	0.17	0.04	0.12		
Δu_{ci}			3.52	4.17			3.15	3.80	2.95	3.56		
Δu_{si}	0.43	0.80	0.56	0.61	0.22	0.62	0.36	0.43	0.23	0.30		

Table 4-3: Energies of solution, binding energies and impurity migration energies for SrCl_2Na^+ complexes

	A3		B1	
	0 K	900 K	0 K	900 K
Defect Energies:				
$E(\text{Cl}_i^-)$	-0.89	-1.27	-1.39	-1.65
$E(\text{Cl}_i^+)$	3.36	3.35	3.61	3.61
$E(\text{Sr}_i^{2+})$	-11.91	-12.70	-12.42	-13.00
$E(\text{Sr}_i^{2+})$	19.16	18.31	19.00	18.33
$E(\text{Na}_i^+)$	-3.83	3.02	-8.25	-9.20
$E(\text{Na}_i^+)$	11.72	11.51	11.72	11.57
Cohesive Energies:				
$E_c(\text{NaCl})$	-7.93	-7.88	-7.93	-7.88
$E_c(\text{SrCl}_2)$	-21.45	-21.41	-21.63	-21.60
Energies of Solution:				
Mode of Solution				
E_1	3.21	2.58	2.58	2.13
E_2	1.55	1.33	1.63	1.46
E_3	1.15	0.92	0.99	0.82
E_4	2.95	2.30	2.65	2.14
E_5	2.97	2.34	2.63	2.15

Table 4-3: cont

	A3		B1		
	0 K	900 K	0 K	900 K	1100 K
Binding Energies:					
Complex					
$(\text{Na}_s^+ \text{Cl}_i^-) \langle 111 \rangle$	-0.65	-0.46	-0.64	-0.50	-0.42
$(\text{Na}_s^+ \text{Na}_i^+) \langle 100 \rangle$	-0.91	-0.86	-0.75	-0.73	-0.74
$(\text{Na}_s^+ \text{Na}_i^+) \langle 111 \rangle$	-0.43	-0.35	-0.32	-0.29	-0.27
$(\text{Na}_i^+ \text{Cl}_i^-) \langle 110 \rangle$	-0.50	-0.37	-0.35	-0.27	-0.22
Migration Energy:					
Cl_i^-	2.65	2.15	2.62	2.22	1.95
Reorientational Energy:					
$(\text{Na}_s^+ \text{Na}_i^+) \langle 100 \rangle$	0.46	0.53	0.49	0.54	0.60

Table 4-4: Impurity-vacancy binding energies and activation energies for vacancy jumps for NaCl: Sr²⁺

Defect	0 K		900 K	
	A3	B1	A3	B1
u ₁	-0.64	-0.66	-0.48	-0.49
u ₂	-0.46	-0.46	-0.37	-0.36
Δu ₁	0.68	0.67	0.55	0.56
Δu ₂	0.88	0.86	0.86	0.84
Δu ₃	0.64	0.66	0.51	0.44
Δu ₄	0.82	0.86	0.62	0.57

43

Figure 4-1: Structure of SrCl_2

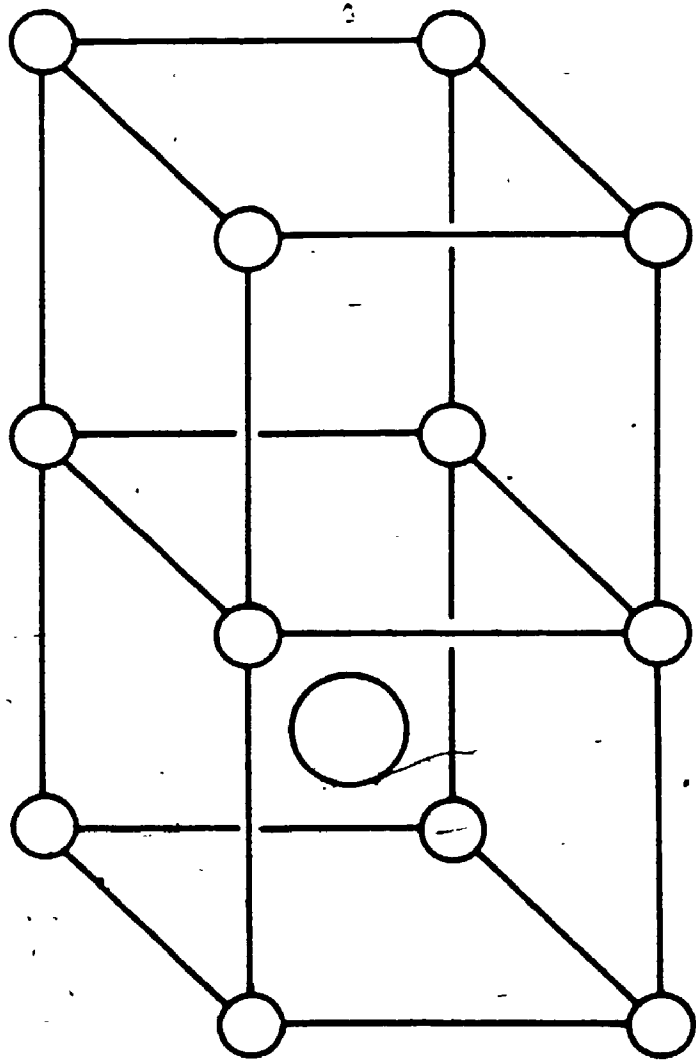


Figure 4-2: Displacement of Na_i^+ from the cube centre to the face of the empty cube as a function of temperature for the $(\text{Na}_i^+ \text{Na}_i^+)<100>$ complex

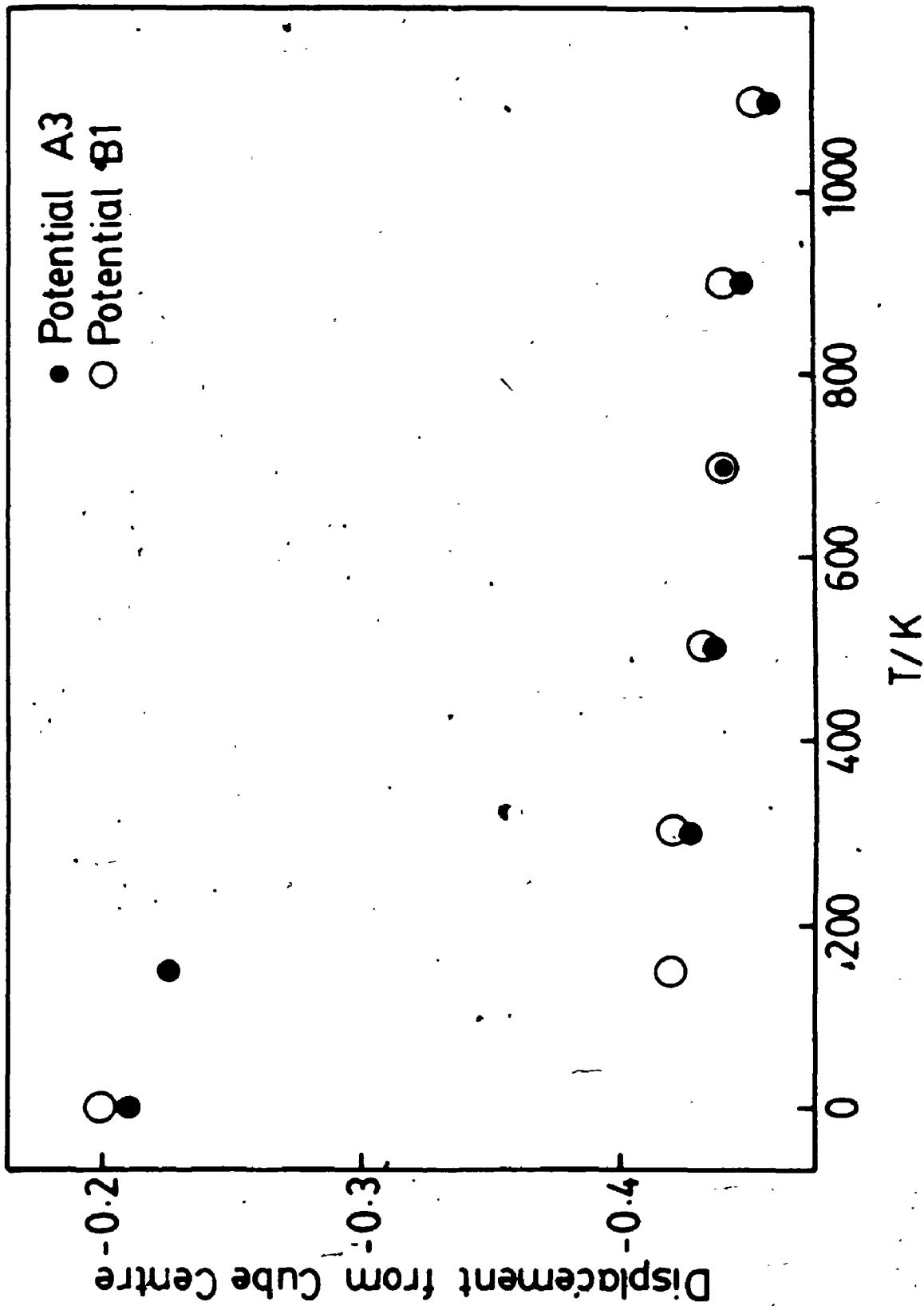
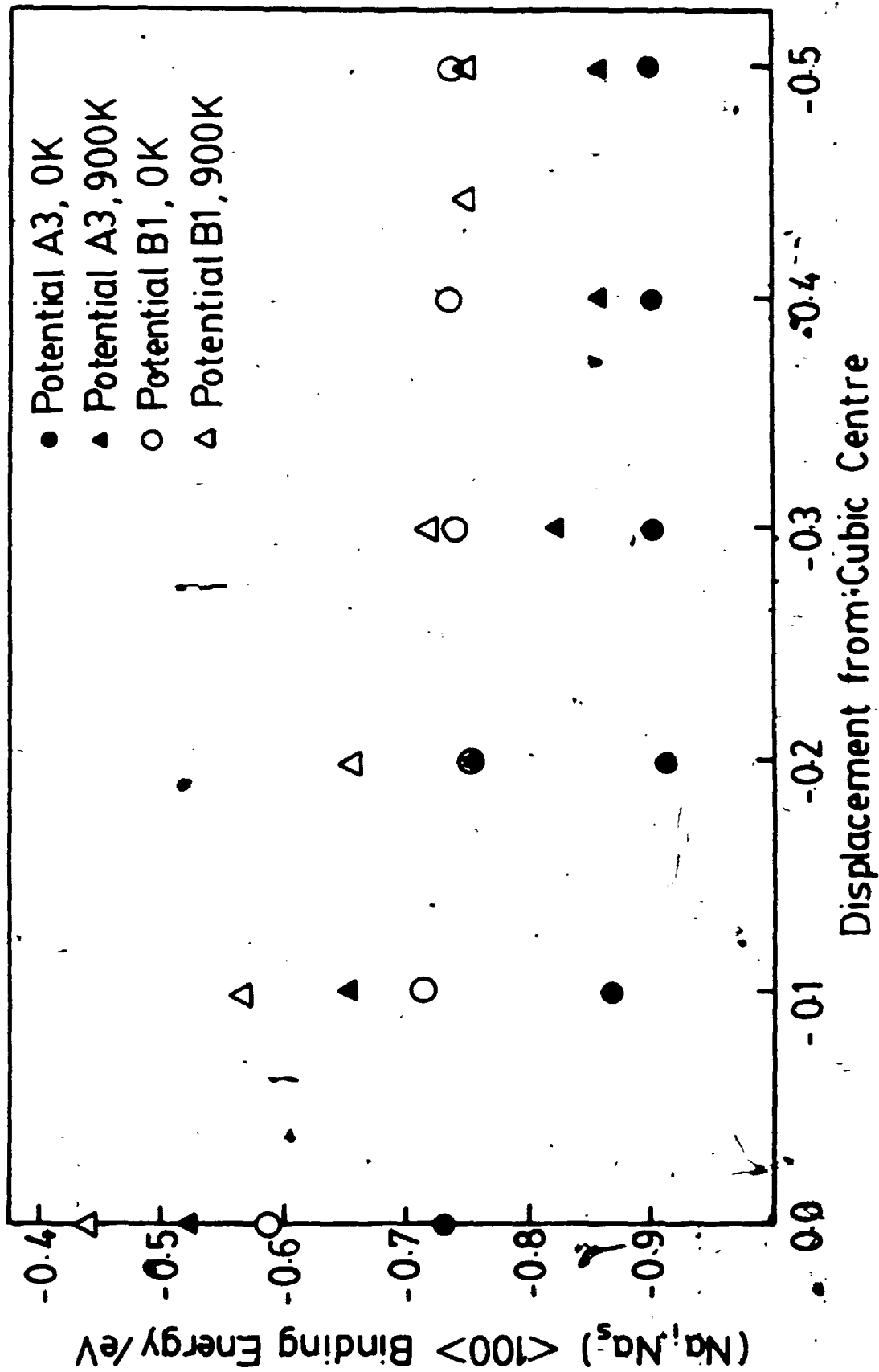


Figure 4-3: Binding energy as a function of displacement of the $(\text{Na}_1^+ \text{Na}_2^+) \langle 100 \rangle$ complex



Chapter Five

Ionic Conductivity Experimental

5.1. Sample Preparation

All the experiments were carried out on Harshaw NaCl, with the exception of a crystal given to us by J. S. Dryden. Samples for the experiments were cleaved from single crystals of NaCl into dimensions of approximately $3\text{mm} \times 10\text{mm} \times 10\text{mm}$. The large faces of the samples were roughened by microtoming so that graphite would adhere to the surface. Graphite (Alpha, -325 mesh, t2N5) was rubbed on to the surfaces to provide a continuous electrical contact. The crystal edges were then freed of graphite by microtoming until clean or by removing the entire edge by cleaving. The cell constant is the ratio of the crystal height to the electrode area and was determined by measuring the cell dimensions using a Mitutoyo Profile Projector Type PJ-250. This measurement was repeated at the end of the experiment. The samples were also weighed before and after the experiments and the difference was never greater than two percent.

5.1.1. Preparation of Sr^{2+} -Doped Crystals

Harshaw NaCl was doped with Sr^{2+} in the following way. A 9×10^{-3} M solution of SrCl_2 (anhydrous, Cerac/pure, -40 mesh, 99.5% pure) in methanol (analytical grade) was applied to a freshly cleaved crystal surface. The solution was applied in small amounts and allowed to dry before the next addition. The total amount of solution was varied resulting in a range of dopant concentrations. This procedure was carried out under an atmosphere of argon.

The crystals were then placed in a graphite boat and inserted into a quartz tube, in the centre of the furnace. The graphite boat was milled from a UF-4S grade graphite rod. The boat was then soaked in two concentrated nitric acid baths to remove any contamination and rinsed in three baths of triply distilled water. The residual water was removed by heating the boat to 200°C under a slow stream of argon gas. The boat used

for the diffusion doping had been used previously for growing NaCl crystals thereby leaching any soluble impurities out of the graphite. The furnace consisted of a single zone and was built from Lindberg windings. The quartz tube was flushed with argon and the crystals were slowly heated to approximately 750 °C. Argon was allowed to flow through the tube at a very slow rate during the annealing. The crystals remained in the furnace for two weeks.

Upon removal from the furnace, the crystal surfaces were no longer smooth, and required more extensive microtoming than was necessary for the pure crystals. This procedure also removed any SrCl_2 which remained on the surface of the sample. The crystals all appeared clear. Further sample preparation was carried out as outlined in Section 5.1.

5.1.2. Preparation of S^{2-} -Doped Crystals

Initially, S^{2-} -doped crystals were prepared as outlined for the Sr^{2+} -doped crystals. However, this did not result in high dopant concentrations. Subsequently, a slurry of Na_2S (anhydrous, Alpha) in methanol was prepared under argon and applied to the sample surface. The procedure then followed that outlined for Sr^{2+} -doped crystals. Some of the crystals appeared milky or yellow in areas when removed from the furnace.

5.2. Electrodes

The electrode system varied depending on whether one or two crystals were being measured. In the first case, the crystal was positioned between two platinum electrodes. Platinum leads were welded to the side of each electrode and Pt-13%Rh wires were spot-welded to the centre of the electrode. These Pt-13%Rh leads were isolated from the platinum electrode by alumina discs. The Pt-13%Rh wires were threaded through a hole in the alumina disc. Slits in the quartz and alumina discs prevented the wires protruding and so deforming the crystal at high temperatures. These Pt/Rh wires, along with the platinum wires, formed a Type R thermocouple. The Pt-13%Rh wire was welded to the electrode at the centre to ensure that the temperature was measured in the middle of the crystal. A diagram is given in Figure 5-1a.

In the double crystal configuration, another electrode, which separated the two crystals, was placed between the two electrodes described previously (Figure 5-1b). This electrode consisted of a piece of platinum folded in half. A Pt-13%Rh wire was spot-welded to the centre of one face of the platinum foil and a Pt wire was welded to one side. Mica isolated the Pt-13%Rh wire from the platinum electrode. The double cell was used when measuring S^{2-} -doped crystals. It is not possible to achieve high dopant concentrations in these crystals and the change in conductivity due to doping is more clearly seen in plots of σ/σ_0 where σ is the conductivity of the doped crystal and σ_0 is the conductivity of the pure crystal at the same temperature.

5.3. Sample Holder

The samples and electrodes were mounted in the quartz holder shown in Figure 5-2. The bottom of the holder extended far enough out of the furnace to ensure that it remained cold throughout the experiment, thereby maximizing its resistance. It was held in place by a stainless steel holder welded into a flange. This holder also supported the quartz tubes which were used to guide the electrode leads to the bottom of the sample holder. The height of the sample holder was such that the crystal was positioned in the centre of the furnace.

The crystal and electrode system were held in place by two quartz discs. The bottom disc was attached to a quartz rod. This rod sat on a spring in an aluminum cup, well out of the furnace, and the distance between the discs was varied by a linear drive mechanism. The spring reduced the force exerted on the crystal. This is especially critical at high temperatures where the crystal is soft and prone to deformation.

The thermocouple wires extended to the bottom of the holder through quartz tubing and connected to thermocouple feed-throughs welded into the flange. Copper wires connected the leads from the feed-through to a high resistance switch (Centralab Power Rotary Switch). An Omega ice-point compensator was used to correct the thermocouple

emf to room temperature. The thermocouple emf was measured by a Keithley multimeter with microvolt resolution. The platinum wires were used to measure the conductance of the crystal, as described in Section 5.5.

5.4. Vacuum Line

The sample holder flange was bolted to the vacuum line using a copper gasket seal. It fitted into an outer quartz jacket sealed to a stainless steel flange. The rest of the vacuum line was metal and enabled the evacuation of the cell and the introduction of argon. An Edwards-diffusion pump using Fomblin oil and a Leybold-Heraeus roughing pump were used to evacuate the system. Experiments were carried out under an atmosphere of pre-purified argon. The gas was passed through an Oxiclear Gas Purifier to remove oxygen and water. A leak valve and several feet of stainless steel capillary tubing were placed between the purifier and the rest of the line to enable a slow flow of argon to be passed through the cell. The gas entered at the top of the outer jacket through a quartz tube and exited at the bottom through a system of molecular sieves, charcoal, and finally through a bubbler containing Santovac-5 pump oil. A diagram of the vacuum line is given in Figure 5-3.

The cell jacket was surrounded by a three-zone furnace built from Lindberg windings. The temperature of the furnace was regulated by a Trirect Mk2 temperature controller, which enabled separate control of each of the three zones.

5.5. Conductivity Measurements

After mounting the crystal, the vacuum line was pumped down to a pressure of approximately 1×10^{-5} torr, measured using an Edwards Penning 8 gauge or a Granville-Phillips Series 260 ion gauge, and the cell was then heated to approximately 200 °C in order to dry the system. The following day, the cell was filled with argon and the crystal was heated to 600 °C and allowed to anneal overnight. This annealing period allowed the impurity ions to dissolve in the crystal and the crystal to equilibrate. During this time, the contact between the graphite and platinum electrodes also improved. Argon

was flowed at a slow rate through the system during the experiment. The crystal was then cycled between 600 °C and 630 °C and measurements of the conductivity made at the lower and upper temperatures selected. These measurements were checked for reproducibility and, if found satisfactory, the experiment was started the next day.

The measurements were carried out in the following way. The temperature was set and allowed to stabilize. This usually required thirty minutes and this waiting period also allowed the crystal to equilibrate. Readings of temperature-conductivity-temperature-conductivity-temperature were then taken. The temperature gradient across the crystal was generally not greater than 0.2 °C. The only time this requirement was not strictly met was at the initial high temperatures for the S²⁻-doped crystals in the double cell configuration. It was difficult to adjust the gradient when the temperature increments were large, as was necessary for these crystals (see below), and the time required to eliminate this gradient would have resulted in additional crystal sublimation. The difference in temperature from the start to the finish of a measurement was never greater than 0.2 °C. At the end of a reading the temperature was changed and the procedure repeated. The conductance was measured by a Wayne-Kerr Autobalance Bridge Model B109 and checked occasionally with a GenRad 1689 RLC Digibridge. The lead resistances were measured and found to be negligible even at high temperatures.

The order of the measurements over the desired temperature range was carried out in one of two ways. The preferred method was to increase the crystal temperature to 680 °C and take measurements at decreasing temperatures until the impurities in the crystal precipitated. This phenomenon was recognized by the associated sudden drop in conductivity. The crystal was then heated to 600 °C and annealed. The measurements were then continued at increasing temperatures. This method minimized effects due to crystal sublimation.

Experience with S²⁻-doped crystals indicated that unless the crystal was heated to the

maximum temperature initially, all the sulphide would not go into solution. It was therefore necessary to heat the crystals to approximately 780 °C to make measurements at decreasing temperatures. Measurements were continued until the impurities precipitated.

Plots of $\log \sigma T$ versus $1/T$ were plotted each morning and sometimes throughout the day in order to follow the progress of the experiment. In this way, it was immediately apparent when the impurities in the crystal had precipitated. The raw data were entered on a PDP 11/24 computer and plots of $\log \sigma T$ versus $1/T$ obtained using a Hewlett-Packard 7225B Plotter.

At the end of an experiment, the crystal was removed from the cell and examined for cracks and damage, although none of the results had to be rejected for this reason. The crystal was re-measured and the new cell constant calculated as described in Section 5.1. The change in the cell constant was never greater than one percent.

5.6. Data Analysis

The conductivity of the crystal was calculated using Equation (1).

$$\sigma(T) = \frac{G(T)}{A(T)} h(T) \quad (1)$$

where $G(T)$ is the measured conductivity, $A(T)$ is the area of the crystal in contact with the electrode, and $h(T)$ is the thickness of the crystal.

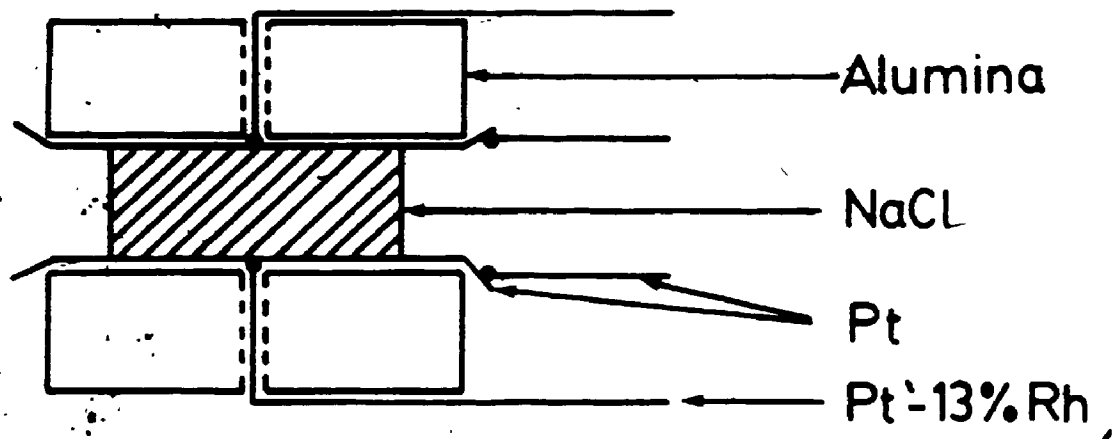
The data were fitted to the theoretical expression for the conductivity using a non-linear least squares fitting routine. The BMDP algorithm P3R Nonlinear Regression was used⁷⁸. This minimizes the weighted sum of squares of the deviations between experimental and calculated values of σ . The conductivity of the crystal in units of Siemens per metre was calculated at each temperature (in Kelvin) and the residual sum of squares RSS given by Equation (2) minimized.

$$RSS = \sum ((\sigma_{\text{expt}} - \sigma_{\text{calc}}) / \sigma_{\text{calc}})^2 \quad (2)$$

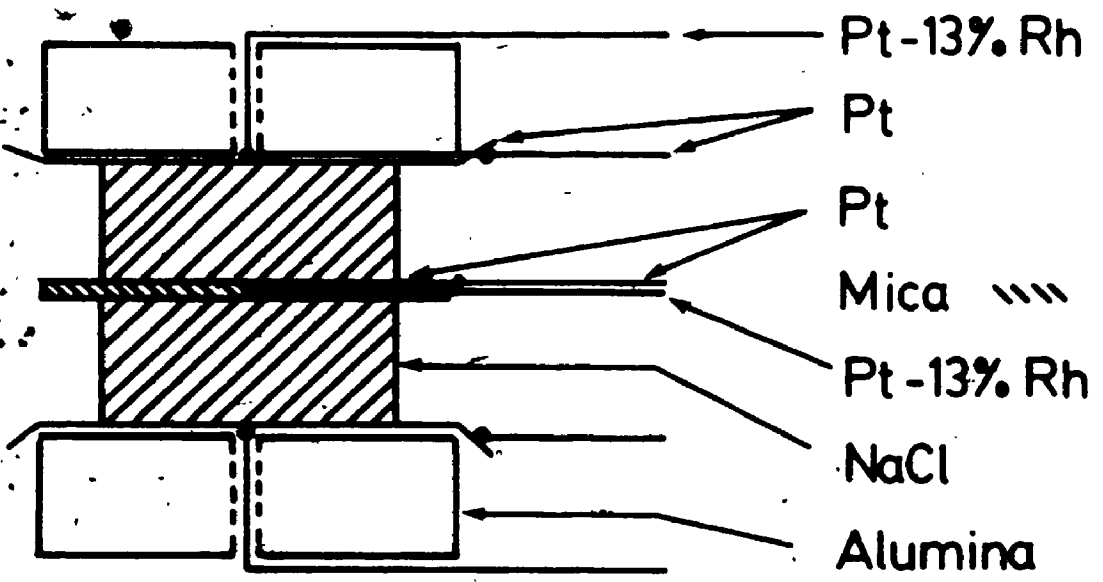
A list of thermodynamic properties calculated in the fitting procedure is given in Table 6-2. Values for the cation and anion Frenkel formation enthalpies and the cation and anion interstitial migration enthalpies remained fixed at the values determined in the HADES 2 calculations. It was assumed, based on the work of Acuña⁷⁷, that if Frenkel defects existed on one or both sub-lattices, their concentrations would be low and therefore the fitting should be relatively insensitive to slight variations in these thermodynamic values.

The order of the fitting procedure was as follows. The Schottky parameters were determined by fitting the data for a pure crystal, with the cation and anion vacancy parameters held constant. The cation vacancy and anion vacancy migration and association parameters were then calculated by fitting the data for cation-doped and anion-doped crystals, respectively, with the Schottky parameters held constant at the values determined by fitting the pure crystal data. This procedure was cycled through several times until the change in values during the fitting became small. Then, more parameters were allowed to vary at each stage of the least squares procedure. This was continued until a self-consistent set of thermodynamic parameters was achieved. The final parameter set was determined by taking the average for the individual runs. Values for the diffusion coefficients of each of the defects were also calculated using the final parameter sets. The calculations were carried out on the Cyber 170/825 and Cyber 170/835 after data transfer from the PDP 11/24.

Figure 5-1: Electrode system. (a) single cell. (b) double cell



a



b




Figure 5-2: Sample holder, TF = thermocouple feedthrough, F = flange, and SSH = stainless steel holder

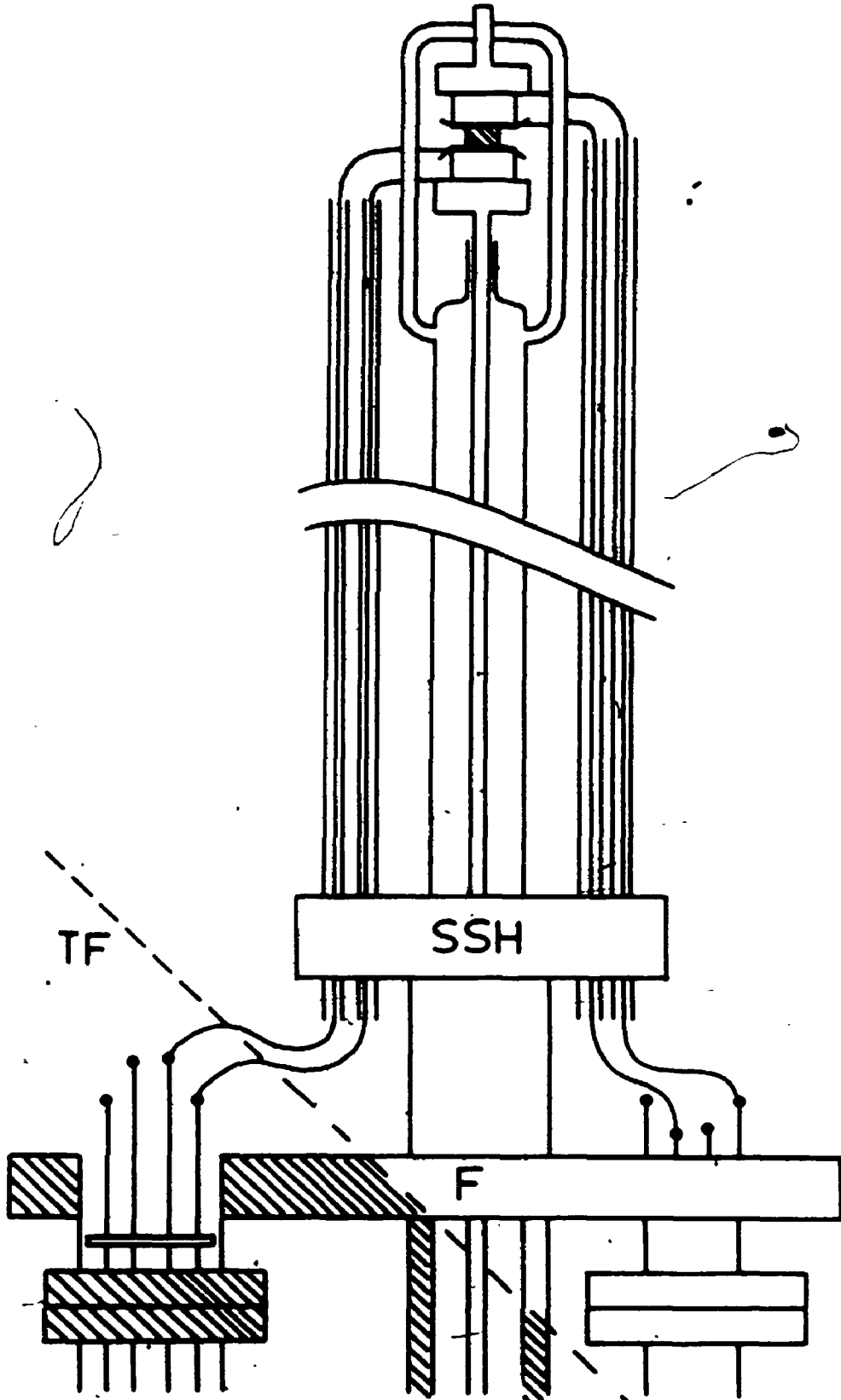
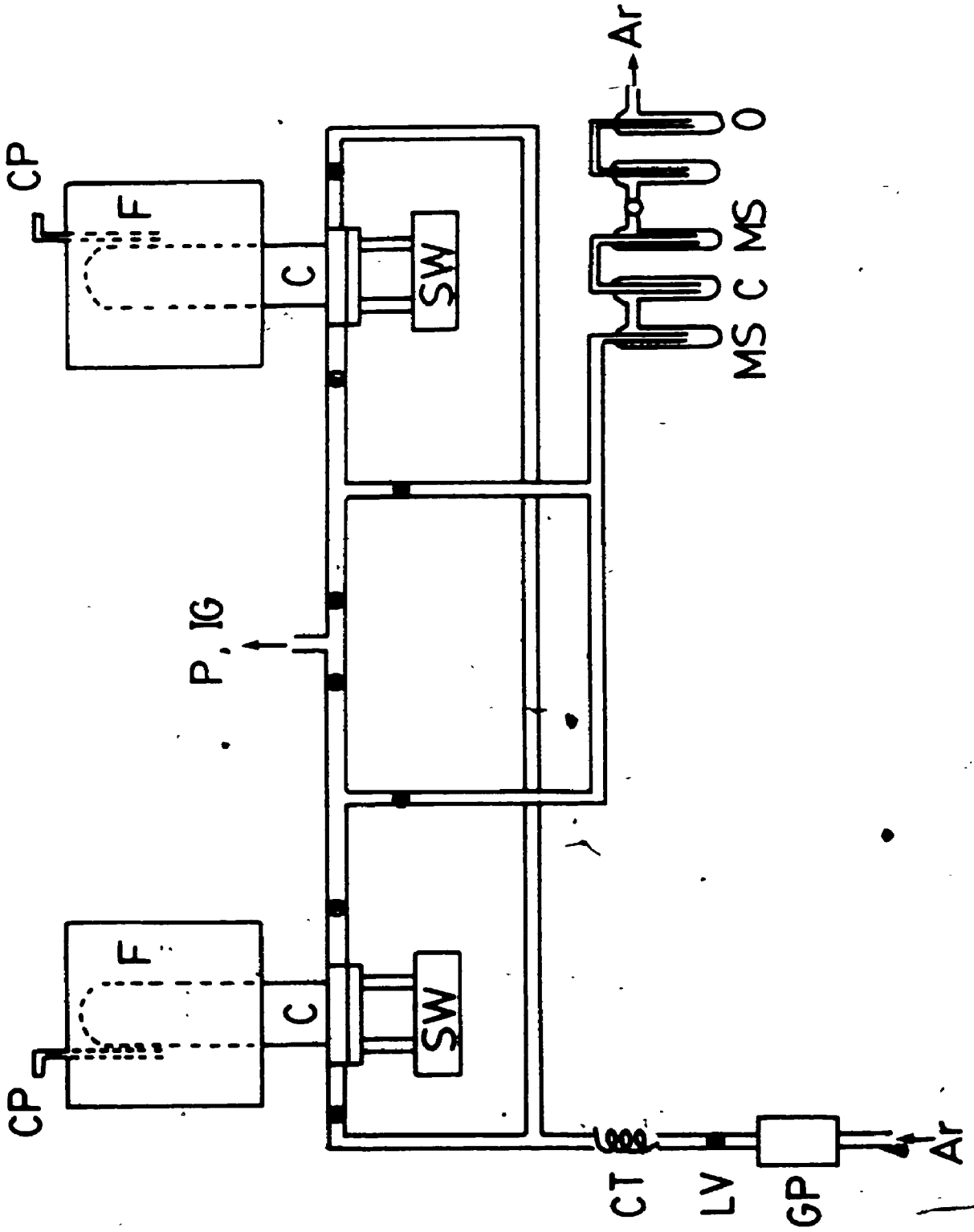


Figure 5-3: Vacuum line, CP = controller probe, F = furnace, C = cell, SW = switching box, P = pumps, IG = ion gauge, CT = capillary tubing, LV = leak valve, GP = gas purifier, MS = molecular sieves, C = carbon, O = oil



Chapter Six

Ionic Conductivity Results and Analysis

6.1. Conductivity Experiments

Conductivity measurements were made on nominally pure NaCl and on crystals doped with divalent cations or anions. These results were plotted in the Arrhenius form, as the log of the product of conductivity and temperature versus the reciprocal of the temperature. The resulting plots may be divided into two distinct regions separated by a knee as seen in Figure 6-1. The upper portion of the plot, the intrinsic region, is a property of the host crystal. The lower portion, the extrinsic region, is dependent on the impurities in the crystal. A slight curvature is often observed in the extrinsic region of doped crystals due to the formation of impurity-vacancy complexes. This feature can be seen in Figure 6-2.

6.1.1. Pure Crystals

The analysis of the nominally pure crystals was based on two Harshaw crystals measured in the single cell configuration. These crystals were used because they covered a much wider temperature range than the pure crystals measured in the double cell configuration. The latter experiments were terminated when precipitation occurred in the doped crystal. The conductivity results for the pure crystals were very similar and therefore the results from only one experiment are plotted in Figure 6-1. This plot includes data taken during the cooling and heating cycles (Section 5.5) and so demonstrates that thermal equilibrium was established prior to each measurement. It also shows the good reproducibility of the measurements. The intrinsic region did not exhibit the curvature observed in the KCl plots of Acuña and Jacobs^{1, 2}

6.1.2. Sr^{2+} -Doped Crystals

Three strontium-doped crystals were measured. The most heavily doped sample exhibited no intrinsic region. The lightest doped crystal had a long extrinsic region and the downward curvature in this region suggested the formation of cation impurity-vacancy complexes. The sudden drop in conductivity at the lowest temperatures is due to precipitation of strontium chloride. The doping level of the third crystal lay approximately mid-way between the other two. It therefore possessed both intrinsic and extrinsic regions and showed the same downward curvature in the extrinsic region. This crystal was measured in the double-cell configuration. The conductivity results for the three crystals are plotted in Figure 6-2.

6.1.3. S^{2-} -Doped Crystals

Six sulphide-doped crystals were measured, all but one (Figure 6-4) in the double cell configuration. The temperature ranges were not as wide as those for the cation-doped crystals since the sulphide precipitated at higher temperatures. The precipitation generally took the form of several small drops in conductivity in contrast to the strontium-doped crystals which tended to precipitate large amounts of the impurity but at lower temperatures. The results from four experiments are plotted in Figures 6-3, 6-4, 6-5, and 6-6 respectively. Three of these figures contain the data for the pure crystal which was measured simultaneously. Data for the other crystals were not plotted because their concentrations were similar to others already given and did not exhibit any additional features. This includes the crystal given to us by Dr. J. S. Dryden which contained 7.1 ppm S^{2-} (determined during data analysis) and exhibited ionic conductivity similar to the crystal doped with 8.6 ppm S^{2-} .

Figures 6-7 and 6-8 are plots of the ratio of the conductivities of the doped and pure crystals for the heaviest doped and a medium doped crystal. These plots emphasize the difference in the conductivities of the pure and doped crystals. This plotting technique is

extremely useful for the lightly doped crystals since it accentuates the small changes in conductivity due to the presence of the dopant

The conductivity of the heaviest doped crystal (60 ppm) (Figures 6-3 and 6-7) is the same as the pure crystal in the intrinsic region and becomes higher than the pure in the extrinsic region, much like the behaviour of divalent cation-doped crystals. This crystal exhibits some association in the extrinsic region, but the curvature in the lower extrinsic region of the plot is far too great to be due to the association of the impurity ions and vacancies alone and is probably a result of the onset of precipitation. The points in this temperature range were therefore excluded in the fitting. In general, regions of the plots which showed obvious precipitation or crystal deformation were removed before the fitting was started. Other less obvious regions were removed after the residuals were examined.

The conductivity of the lightly doped crystals has a lower value than that of a pure crystal in the intrinsic region, approaches the same values in the knee area and then drops below the pure crystal in the extrinsic region. The intrinsic behaviour is probably a result of the lower mobility of the anion vacancies compared to the cation vacancies. As the concentration of anion vacancies is increased compared to the cation vacancies, the conductivity will be depressed. However, as the concentration of the anion vacancies is further increased, the conductivity of the doped crystal will be higher than the pure crystal, as witnessed in the extrinsic region of the most heavily doped crystal. The lower conductivity in the extrinsic region might be attributed to the precipitation of CaS (Figure 6-5). This would result in the removal of both anion and cation divalent dopants and therefore the conductivity of the crystal would be less than that of the nominally pure Harshaw crystal.

Corish *et al*⁷⁹ found the same lowering of the conductivity in thallos chloride doped with divalent cation impurities. The cation vacancy migration energy was significantly

lower than that of the anion in thallos chloride and this resulted in an appreciable lowering of the conductivity. They were unable to achieve high enough doping levels to see the increase in conductivity in the extrinsic region but suggested that this would occur for the reasons outlined above.

Chemla and B ni re²⁴ noted in their work involving SO_4^{2-} -doped KCl crystals that the conductivity of the doped crystal was less than that of the pure crystal at low temperatures. They also assumed that this was due to the interaction of the dopant with background divalent cation impurities.

6.2. Calculation of Defect Energies Held Constant during the Fitting Procedure

The cation and anion Frenkel defect formation energies and the cation and anion interstitial migration energies were calculated using the HADES program and the TD potentials at 0 K. It was also necessary to calculate the vacancy pair association energy and the activation energy for cation and anion jumps into the pairs, in order to determine the diffusion coefficients. The values obtained in these calculations are listed in Table 6-1.

6.3. Conductivity Model

Four models for the conductivity of sodium chloride were tested. These took into account the possibility of only Schottky defects, Schottky plus cation Frenkel defects, Schottky plus anion Frenkel defects, and Schottky plus Frenkel defects on both sub-lattices. A particular model was chosen at the start of the fitting procedure. In the following analysis, the most general model is used and the other models may be selected by simply setting the relevant equilibrium constants to zero.

Each of the models also assumed that association of cation impurities with cation vacancies occurred and that a small amount of divalent cation impurity was present in the pure crystals. It was also assumed that the anion impurities would form impurity-

vacancy complexes. The amount of cation impurity in the anion-doped crystals was held at the concentration determined for the pure crystals (1.2ppm).

The values for the anion and cation Frenkel formation energies and the anion and cation interstitial migration energies were held constant at the values determined in the HADES calculations since it was assumed, based on the KCl work of Acuña⁷⁷, that if Frenkel defects were present, their concentration would be low and therefore insensitive to the fitting procedure.

6.4. Analysis of the Data

The purpose of the analysis was to determine the thermodynamic properties of the defects given in Table 6-2. The conductivity data was analysed according to the method outlined by Acuña and Jacobs^{1, 2} for KCl. Initial estimates of the thermodynamic properties were made and the equilibrium constants were calculated in terms of the activities, a_r , of each of the species, r , and the Gibbs energy of defects, $g_r = h_r - Ts_r$,

$$K'_S = a_{c_i} a_{a_v} = \exp(-g_S/kT) = K_S f_{c_i} f_{a_v} \quad (1)$$

$$K'_{Fa} = a_{a_v} a_{a_i} = \exp(-g_{Fa}/kT) = K_{Fa} f_{a_v} f_{a_i} \quad (2)$$

$$K'_{Fc} = a_{c_i} a_{c_i} = \exp(-g_{Fc}/kT) = K_{Fc} f_{c_i} f_{c_i} \quad (3)$$

Firstly, association was neglected and the mole fractions n_r , given by,

$$n_r = a_r / f_r \quad (4)$$

where f_r is the activity coefficient of species r , were substituted from Equations (1), (2), and (3) into the expression for charge neutrality,

$$n_{c_i} + n_{a_v} + c_M = n_{a_i} + n_{c_v} + c_X \quad (5)$$

with all the activity coefficients set equal to unity initially. The term c_M is the concentration of divalent cation impurity and c_X is the concentration of divalent anion impurity. The resulting quadratic in n_{c_v} was solved to give an initial estimate of the concentration of cation vacancies which was then used in calculating the activity coefficients. The S^{2-} -doped crystals were insensitive to the fitting in terms of the cation vacancy concentration and therefore a second set of equations, solved for n_{a_v} , were used for these crystals.

The association terms were then calculated as a function of the concentration of cation impurity-vacancy complexes, p , and anion impurity-vacancy complexes, p' , using Equations (6) and (7).

$$K_{ct} = \frac{p}{(1-p)f_M c_{cv} f_{cv}} = 12 \exp(-g_{ct}/kT) = K_{ct} f_M f_{cv} \quad (6)$$

$$K_{at} = \frac{p'}{(1-p')f_X c_{av} f_{av}} = 12 \exp(-g_{at}/kT) = K_{at} f_X f_{av} \quad (7)$$

Activity coefficients for neutral complexes are unity in the Debye-Huckel approximation

The Debye-Hückel screening constant κ was calculated from the formula.

$$\kappa^2 = \frac{8\pi q^2 n_i}{v \epsilon_s kT} \quad (8)$$

In the above equation, q is the charge on the ions, v is the unit cell volume, ϵ_s is the static dielectric constant, k is the Boltzmann constant and T is the temperature in Kelvin. The static dielectric constant and unit cell volume were calculated at each temperature^{46, 65}.

The activity coefficients, f_r , could then be calculated using Equation (9).

$$\log f_r = - \frac{q^2}{2\epsilon_s kT} \frac{\kappa}{(1 + \kappa R_r)} \quad (9)$$

where R_r is the distance below which the defects are assumed to be associated to form an impurity-vacancy complex or vacancy pair.

Once the activity coefficients were determined, the unprimed equilibrium constants were calculated from equations (1) to (3), (6), and (7). These values were then substituted into the equation for the conservation of mass, charge, and lattice sites (conservation of virtual charge).

$$n_{cv} - n_{av} = n_{ci} - n_{ai} + c_M - c_X - c_{ct} + c_{at} \quad (10)$$

The resulting fourth order equation was solved using Newton's method in terms of either the cation or anion vacancies. Both of these equations are given below.

$$\begin{aligned}
 & K_{ck} (K_S + K_{Fa}) n_{cv}^4 \tag{11} \\
 & + (K_S (1 + K_{ck} (C_X + K_{ak} (K_S + K_{Fa})))) + K_{Fa} n_{cv}^3 \\
 & + (K_S (K_S (K_{ak} - K_{ck}) - K_{Fc} K_{ck} + K_{Fa} K_{ak} + C_X - C_M)) n_{cv}^2 \\
 & - (K_S (K_{Fc} + K_S (1 + K_{ak} (C_M + K_{ck} (K_S + K_{Fc})))) n_{cv} \\
 & - K_S^2 K_{ak} (K_S + K_{Fc}) \\
 & = 0
 \end{aligned}$$

$$\begin{aligned}
 & K_{ak} (K_S + K_{Fc}) n_{av}^4 \tag{12} \\
 & + (K_S (1 + K_{ak} (C_M + K_{ck} (K_S + K_{Fc})))) + K_{Fc} n_{av}^3 \\
 & + (K_S (K_S (K_{ck} - K_{ak}) - K_{Fa} K_{ak} + K_{Fc} K_{ck} + C_M - C_X)) n_{av}^2 \\
 & - K_S (K_S (1 + K_{ck} (K_{ak} (K_S + K_{Fa}) + C_X)) + K_{Fa}) n_{av} \\
 & - K_S^2 K_{ck} (K_S + K_{Fa}) \\
 & = 0
 \end{aligned}$$

The concentration of the other defect species could then be calculated using the equilibrium expressions.

Once the concentrations of the defects were known, it was possible to calculate their mobilities and consequently their contributions to the total conductivity. The mobilities, u_r , were calculated using the following expression.

$$u_r = \bar{u} S_r |q_r| a_r^2 w_r / kT \tag{13}$$

Here \bar{u} is the Onsager-Pitts correction factor and is given by Equation (14), S_r is the number of equivalent sites into which the defect can jump, such that $S_r=4$ for vacancies and $S_r=2$ for interstitials, a_r is the component of the jump distance along the electric field, and w_r is the frequency with which the defect surmounts the energy barrier separating the initial and final equilibrium positions (Equation (15)), in which ν_0 is the Debye frequency.

$$\bar{u} = 1 - \frac{e^2 \kappa}{3\epsilon_r kT (\sqrt{2} + 1) (\sqrt{2} + \kappa R_r) (1 + \kappa R_r)} \tag{14}$$

$$n_i = v_i \exp(-\Delta g_i / kT) \quad (15)$$

The total conductivity is then the sum of the contributions from each of the species and can be calculated according to Equation (16).

$$\sigma = \sum \sigma_i = N \sum n_i u_i |q_i| \quad (16)$$

6.5. Results of the Non-linear Least Squares Fitting

The parameters from fitting the individual crystal data are given in Table 6-3. The final parameters were determined by averaging the values from the separate fittings. These values are listed in Table 6-4. The cation-doped crystals were sometimes insensitive to the variation of the anion parameters and vice versa, and therefore it was often necessary to fix these values during the minimization procedure. These parameters are in parentheses and were not included in the averaging.

The impurity concentration was also determined in the fitting and the values for the individual crystals were included in Table 6-3. Setting the cation impurity concentration to zero resulted in a small decrease (2 ppm) in the sulphide concentration when tested in the crystal containing 32 ppm S^{2-} . The two values for the cation association enthalpy and entropy reflect the influence of the impurity type on these parameters. The divalent cation impurity in the pure crystals was likely Ca^{2+} , however, Sr^{2+} was used as the cation dopant.

The root mean square of the residuals, used as the fitting criterion, is also given in Table 6-3. The square root of this quantity was generally less than two percent and never greater than three percent. The number of sign changes was also maximized and these are also included in this table. The temperature range over which the conductivity data was fitted is given for each of the crystals. It was often necessary to limit this temperature range due to the precipitation of impurities at low temperatures and deformation of the crystal at high temperatures.

Examples of the residuals for the final individual fittings are plotted in Figures 6-9.

6-10, and 6-11 for pure, cation-doped, and anion-doped crystals respectively. The fittings for the anion-doped crystals were generally not as good as the others. This could be due in part to the experimental difficulties at high temperatures, low dopant concentrations compared to the strontium-doped crystals, and problems with precipitation at low temperatures.

6.5.1. Discussion of the Model Type

Attempts were made to fit the data with all four defect models, Schottky, Schottky plus cation Frenkel, Schottky plus anion Frenkel, and Schottky plus Frenkel defects on both sub-lattices. Better results were achieved if anion Frenkel defects were excluded. There was very little difference in the results if cation Frenkel defects were included.

Allnatt and Pantelis⁸⁰ included Frenkel defects in their analysis but it was realized later that the satisfactory fitting with the Schottky model was due to the slow convergence of the steepest-descent algorithm. Nelson and Friauf¹⁶ found that the inclusion of cation Frenkel defects produced unrealistic values for the anion activation enthalpy determined from the fitting of the conductivity data. The inclusion of cation Frenkel defects in the diffusion analysis resulted in a larger contribution for cation diffusion by vacancy pairs compared to the anion diffusion through pairs. Since this was already at the maximum limit determined by the correlation factor, they concluded that there was no appreciable contribution from cation Frenkel defects. This is in marked contrast to KCl which exhibited an improvement in the conductivity fitting when Frenkel defects were included on both sub-lattices^{1, 2}.

The correct model for the defect structure of sodium chloride cannot be stated unequivocally. The fitting improved when anion Frenkel defects were excluded and therefore these defects are probably not present. It was not possible to determine whether or not cation Frenkel defects were present since the fitting was no better or no worse if they were included in the model. However, merely including four more parameters

would be expected to effect a slight improvement in the fitting, so that probably the cation Frenkel defect concentration is very small.

6.5.2. Discussion of Conductivity Parameters

The Schottky and cation energy parameters are in good agreement with the previously determined experimental values of 2.44 eV and 0.69 ± 0.01 eV determined by B ni re *et al.*²¹ and 2.4-2.5 eV and 0.65 eV determined by Allnatt, Pantelis, and Sime¹³ as well as the HADES calculated values of 2.32 and 2.54 eV and 0.66 and 0.67 eV²² (see also Table 1-1).

The main controversy in this field however lies in the anion vacancy parameters. As mentioned in Section 1.5, a broad range in values exists due to the difficulty in determining these parameters. The values obtained from the present experiments were in agreement with the value of 0.77 eV determined from diffusion experiments by B ni re *et al.*²¹. The Arrhenius energy is also close to the value of 1.92 eV determined by Barr *et al.*²⁸, since from the present parameters $(h_S/2) + \Delta h_{an} = 1.95$ eV. The values determined in the HADES calculations (Table 1-1) are also in agreement with this lower value. The small difference in migration energies is consistent with the linearity of the high temperature region of the plot.

The current values do disagree with the results of Cook and Dryden^{31, 32}. Their experiments were carried out on quenched crystals and it was assumed that neither association nor precipitation were occurring. If the concentration of S^{2-} ions is not constant the slope of the conductivity plot will be too high as can be seen in the lower extrinsic region of the most heavily anion-doped crystal (excluded in the analysis). In addition, the final values found here for h_{ak} and s_{ak} indicate a high degree of association and this would also increase the slope of the conductivity plot.

Attempts were made to fit the conductivity data with the higher anion migration value of Cook and Dryden³¹. This was done by fixing the anion migration enthalpy and

varying the other parameters. Association was included in one trial but not in the other since it had been excluded in their work. In both instances, it was found necessary to decrease the Schottky formation enthalpy to unacceptably low values in order to fit the data.

6.6. Transport Numbers and Complex Concentrations

Transport numbers, t_p , were calculated for all of the samples as the ratio of the conductivity of a given species to the total conductivity. Several examples of these results from the individual crystal fittings are given in Figure 6-12.

The transport numbers for the pure crystal indicate that the cation is only slightly more mobile than the anion. At high temperatures, the transport number for the cation vacancies approaches 0.5, with very little temperature dependence above 840 K, which would account for the linearity of the conductivity plots in the intrinsic region. The value for t_{cv} approaches 1.0 at lower temperatures as the conductivity becomes extrinsic. The value at 800 K is in good agreement with a value determined by B  ni  re, B  ni  re, and Chemla²¹ for pure NaCl.

The cation vacancy transport number was also plotted for the Sr^{2+} -doped crystals. The heavier doped crystal has no intrinsic conductivity and the transport is almost entirely by cation vacancies. The lightest doped crystal approaches intrinsic conductivity at high temperatures.

Similar calculations were carried out for the S^{2-} -doped crystals. The heaviest doped crystal was measured over a limited temperature range due to sulphide precipitation, however the increase in the anion vacancy transport can be observed. The lighter doped crystals indicate that cation vacancy transport still dominates at high temperatures (intrinsic region); however its contribution to the conductivity drops and approaches zero in the extrinsic region. The variation in t_{cv} in the intrinsic region is a measure of the sensitivity of this quantity to small variations in defect parameters.

The concentration of vacancy-impurity complexes was also calculated and these values were plotted as the fraction of complexes to free impurities p versus temperature, for both the cation and anion-doped crystals (Figures 6-13 and 6-14). The plots for the cation complexes show the expected increase in association with decreasing temperature and an increase in the degree of association with increasing impurity concentration. The anion complexes exhibit the same trends, however there is some crossing of the curves at high temperature resulting in less association of the 32 ppm crystal than the 8.6 ppm crystal at higher temperatures. The minima observed are due to the fact that, at high temperatures, the increase in p due to the rising vacancy concentration from the Schottky equilibrium outweighs the decrease in p due to the temperature dependence of the equilibrium constant K_{vk} . At higher impurity concentrations, the minimum therefore occurs at increasingly higher temperatures. The same effect is in fact evident in Figure 6-13, although only for the lowest concentration is the minimum reached. These plots also support the suggestion that even at 600 °C, the temperature at which Cook and Dryden quenched their samples, the heavier doped samples are showing appreciable anion association.

The association was also extrapolated to lower temperatures using the parameters from the individual fittings. This gave an approximation of the anion impurity-vacancy association at lower temperatures and although the association for the 32 ppm sample is less than that for the 8.6 ppm sample at high temperatures, the relative concentrations of complexes are as one would expect at lower temperatures.

6.7. Diffusion Coefficient Calculations

The theory of ionic diffusion has been given by several authors^{81, 19, 21, 6}. The diffusion coefficient of a species r , which is diffusing by a random walk, is given by,

$$D_r = \Gamma_r r^2 / 6 \quad (17)$$

The quantity r^2 is the mean square displacement and Γ_r is the jump frequency. However, diffusion in crystals is not necessarily random. In the case of tracer diffusion, D^* , when

the tracer ion jumps into a nearby vacancy, the next jump of the vacancy is random but the tracer ion is most likely to jump back into its original position. The relationship between the tracer (D_r^*) and self-diffusion (D_r) coefficients can be expressed in terms of the correlation factor, f_r ,

$$f_r = D_r^* / D_r \quad (18)$$

The self-diffusion coefficient may be calculated from the conductivity data using the Nernst-Einstein relation,

$$D_r = \frac{kT}{ne^2} \sigma_r \quad (19)$$

where n is the number of ions per unit volume.

Assuming that Schottky defects dominate, the jump frequencies, ν_r , can be calculated from the defect parameters determined in the conductivity fitting using the following equation,

$$\nu_r = \nu_0 \exp(\Delta s_r / k) \exp(-\Delta h_r / kT) \quad (20)$$

The jump rate is then the product of the jump frequency and the number of equivalent sites.

$$\Gamma_r = 12 n_r \nu_0 \exp(-\Delta g_r / kT) \quad (21)$$

These equations can then be substituted into Equation (17) for the diffusion coefficients for the free cation and anion vacancies resulting in the following equations,

$$D_{cv} = 4a^2 f_S n_{cv} \nu_{cv} \quad (22)$$

$$D_{av} = 4a^2 f_S n_{av} \nu_{av} \quad (23)$$

where f_S is the geometrical correlation factor and is equal to 0.78146 for alkali halides.

The presence of vacancies pairs also contributes to the diffusion; however, since the pairs are neutral, they do not contribute to the conductivity. Lidiard⁶ proposed that diffusion through excess transport found when comparing ionic conductivity and diffusion experiments. Subsequent experimental investigations found this mechanism to be true^{19, 20, 21, 17, 16, 18}.

The concentration of vacancy pairs is given by the following expression.

$$c_p = 6 \exp(-g_p/kT) \quad (24)$$

The factor 6 arises from the orientational entropy and $g_p = g_s + g_{vp}$ i.e. the pair formation Gibbs energy is equal to that for the formation of a Schottky defect plus the change in Gibbs energy on formation of the pair. The expressions for the jump frequencies are similar to those for the single vacancies,

$$v_{cp} = v_0 \exp(-\Delta g_{cp}/kT) \quad (25)$$

$$v_{ap} = v_0 \exp(-\Delta g_{ap}/kT) \quad (26)$$

and the mean square displacement is the same as that for the single vacancies. In this case however, the correlation factor is not constant and is a function of the ratio of the jump frequencies, i.e. $f_{cp} = \phi(v_{ap}/v_{cp})$ and $f_{ap} = \phi(v_{cp}/v_{ap})$. The migration through vacancy pairs can then be expressed as,

$$D_{cp} = (4/3) a^2 f_{cp} c_p v_{cp} \quad (27)$$

$$D_{ap} = (4/3) a^2 f_{ap} c_p v_{ap} \quad (28)$$

The defect energies determined in the HADES calculations were used for the enthalpy of vacancy pair association and the enthalpy of the cation and anion jumps into the pair. The entropy terms were determined by setting them equal to -1.0 k for the association and 1.0 k for the jumps, and then varying these values to fit the experimental results of B ni re *et al.*^{20, 21} and Rothman *et al.*¹⁸. Varying the entropies merely shifts the calculated diffusion curve up or down the ordinate and so amounts to fitting the experimental data at one temperature. The agreement between the calculated and experimental D over the whole temperature range is an excellent test of the final parameter sets. Since the correlation coefficients had been set equal initially to the ratio of the jump frequencies, the entropies were then in error by a scaling factor. The actual correlation factor was determined at 800 K from the work of Compaan and Haven⁸² and Howard⁸³ and the entropies were adjusted. It is only possible to determine the differences $s_{vp} - s_{cp}$ and $s_{vp} - s_{ap}$ and therefore the value for s_{vp} was set somewhat arbitrarily; however on a simple Einstein model it should be approximately one-sixth the value of the Schottky formation entropy (see Mott and Gurney⁸⁴, page 26).

6.8. Diffusion Coefficient Results

Diffusion coefficients were calculated using each of the individual parameter sets and the average parameter set. The individual contributions from the vacancies and vacancy pairs as well as the total cation and anion diffusion coefficients were calculated. Three sets of values were plotted in Figures 6-15 through 6-32. These correspond to values calculated from the average parameter set with the impurity concentration of a nominally pure crystal, the parameter set for NaCl doped with 27 ppm Sr^{2+} , and the parameter set for the sample doped with 19 ppm S^{2-} . The experimental values of B ni re *et al*^{20, 21} and Rothman *et al.*¹⁸ were also plotted for comparison.

The total cation diffusion for the strontium-doped crystal agrees with the experimental data in both the intrinsic and extrinsic regions (Figures 6-15 and 6-16 respectively). The curve for the contribution from the vacancy pairs is actually higher than B ni re's. The cation vacancy pair contribution would be difficult to determine experimentally since none of the crystals were doped with divalent anion impurities. The slope of the total anion diffusion coefficient differs from the experimental one due to the difference in the single vacancy pair parameters as can be seen by comparing the individual contributions of the single vacancies and the pairs to the diffusion data.

The parameters for the anion doped crystal reproduce the total cation diffusion fairly well but give values for the total anion diffusion which are higher than the experimental. The difference in the cation diffusion lies primarily in the vacancy pair diffusion since the single vacancy diffusion is very close to the experimental curve. The opposite is true for the anion diffusion where the agreement with the experimental curve is very good.

The average parameters produce diffusion coefficient curves with the same overall results as the individual fits. The values for the total cation diffusion are quite good, the difference in the results lying in the contribution from vacancy pairs. Attempts were made to improve this situation by varying the entropies but they were unsuccessful. The

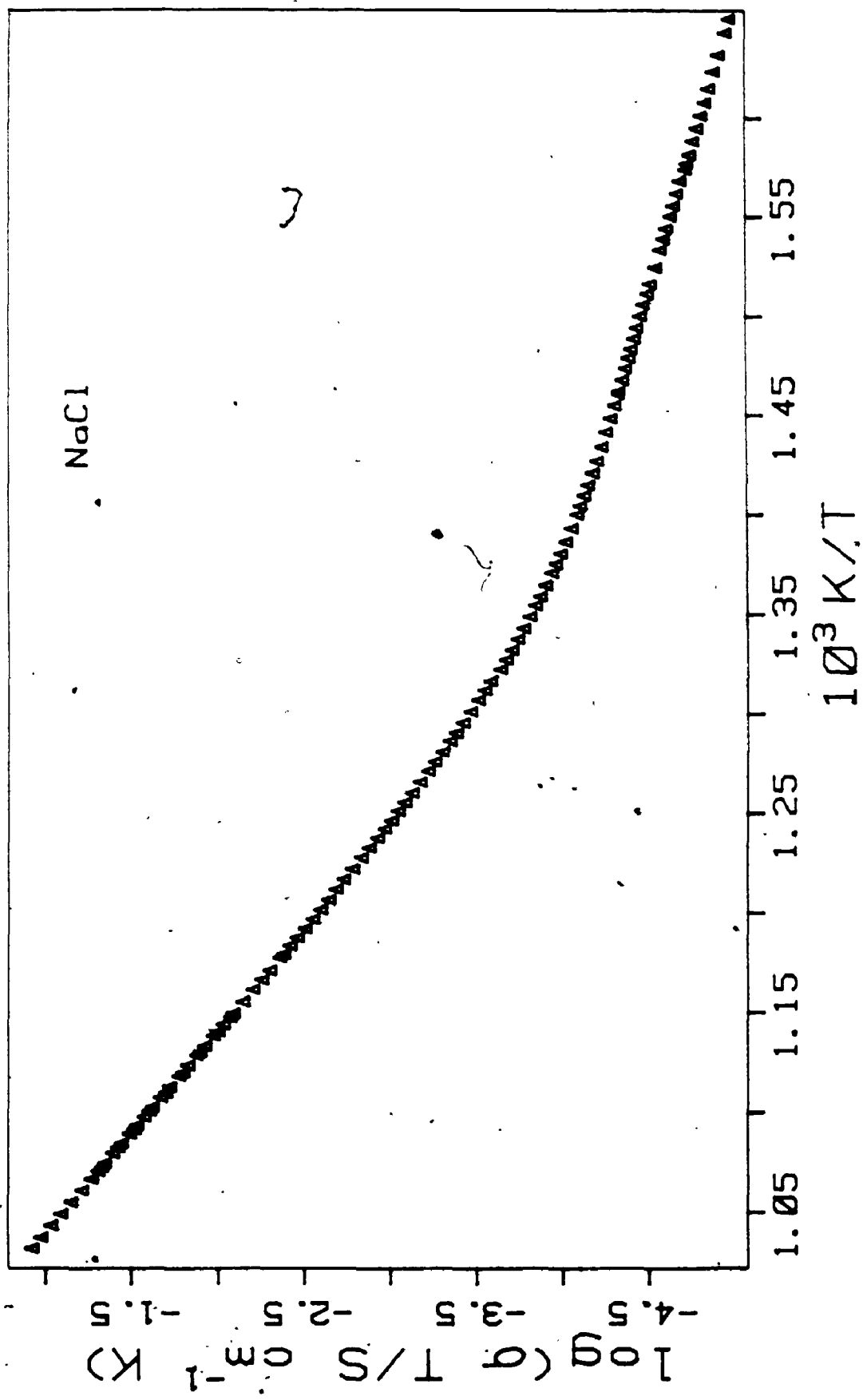


Table 6-1: Calculated Frenkel and vacancy pair energies for NaCl

Symbol	Energy	Units	Description
u_{Fc}	3.32	eV	cation Frenkel formation energy
u_{Fa}	3.47	eV	anion Frenkel formation energy
Δu_{ci}	0.17	eV	cation interstitial migration energy
Δu_{ai}	0.17	eV	anion interstitial migration energy
u_{vp}	-0.86	eV	vacancy pair association energy
Δu_{cp}	0.98	eV	cation jump into vacancy pair
Δu_{ap}	0.93	eV	anion jump into vacancy pair

Table 6-2: Thermodynamic properties determined during fitting of temperature dependence of conductivity

Symbol	Units	Description
h_S	eV	Schottky formation enthalpy
s_S	k	Schottky formation entropy
Δh_{cv}	eV	cation vacancy migration enthalpy
Δs_{cv}	k	cation vacancy migration entropy
Δh_{av}	eV	anion vacancy migration enthalpy
Δs_{av}	k	anion vacancy migration entropy
h_{ck}	eV	cation impurity-vacancy association enthalpy
s_{ck}	k	cation impurity-vacancy association entropy
h_{ak}	eV	anion impurity-vacancy association enthalpy
s_{ak}	k	anion impurity-vacancy association entropy
c_M	ppm	cation impurity mole fraction
c_A	ppm	anion impurity mole fraction
h_{vp}	eV	vacancy pair association enthalpy ^a
s_{vp}	k	vacancy pair association entropy
Δh_{cp}	eV	cation jump into pair enthalpy ^b
Δs_{cp}	k	cation jump into pair entropy
Δh_{ap}	eV	anion jump into pair enthalpy ^c
Δs_{ap}	k	anion jump into pair entropy

^a $h_{vp} = u_{vp} (0 \text{ K})$ (fixed)

^b $\Delta h_{cp} = \Delta u_{cp} (0 \text{ K})$ (fixed)

^c $\Delta h_{ap} = \Delta u_{ap} (0 \text{ K})$ (fixed)

Table 6-3: Final defect parameters for each crystal

Property	Crystals				
	1	2	3	4	5
c_M^2	16	15	370	90	27
c_S^2	0	0	0	0	0
h_S	2388	2397	2420	2521	2478
s_S	8816	8936	9086	10217	9778
Δh_{ev}	0654	0632	0635	0619	0621
Δs_{ev}	1257	4010	1022	1029	1079
Δh_{av}	0750	0741	(0741)	(0741)	(0741)
Δs_{av}	2271	2242	(2242)	(2242)	(2242)
h_{ck}	0609	0614	0639	0644	0647
h_{jk}	2680	2337	2523	2274	2181
s_{jk}	-	-	-	-	-
RSS $\times 10^4$	0817	1464	1877	0518	0465
T. upper	1031.1	1004.6	869.8	1022.9	1026.1
T. lower	629.9	608.8	667.7	699.5	364

Table 6-3: cont

Property	Crystals				
c_{M^2}	(1 2)	(1 2)	(1 2)	(1 2)	(1 2)
c_S	60	32	19	8 6	7 1
h_S	2 347	2 285	2 429	2 305	2 533
s_S	7 931	7 404	9 221	7 179	10 391
Δh_{cv}	0 621	0 619	0 620	0 620	0 621
Δs_{cv}	1 047	1 050	1 052	1 055	1 053
Δh_{jv}	0 718	0 756	0 768	0 743	0 734
Δs_{jv}	2 367	2 251	2 282	2 184	2 310
h_{ck}	(0 644)	(0 644)	(0 644)	(0 644)	(0 644)
s_{ck}	(2 224)	(2 224)	(2 224)	(2 224)	(2 224)
h_{jk}	0 750	0 716	0 775	0 782	0 733
s_{jk}	1 339	1 619*	1 086	1 616	1 429
$RSS \times 10^4$	5 429	2 496	5 712	1 232	0 856
T. upper	964 8	998 2	1036 6	1021 8	979 7
T. lower	842 5	801 7	683 8	757 5	750 2

Table 6-4: Final average defect parameters

Parameter	Value
h_S	2.410
s_S	8.896
$\Delta h_{c,c}$	0.626
$\Delta s_{c,c}$	1.065
$\Delta h_{d,c}$	0.744
$\Delta s_{d,c}$	2.272
$-h_{c,k}$	0.643 ^a , 0.612 ^b
$-s_{c,k}$	2.326 ^a , 2.508 ^b
$-h_{d,k}$	0.751
$-s_{d,k}$	1.418
$-h_{v,p}$	0.865
$-s_{v,p}$	1.200
$\Delta h_{c,p}$	0.976
$\Delta s_{c,p}$	2.850
$\Delta h_{d,p}$	0.928
$\Delta s_{d,p}$	2.965

^a Association parameters for Sr²⁺ doped crystals

^b Association parameters for naturally-occurring impurity,
probably Ca²⁺

Figure 6-1: Arrhenius plot for pure NaCl

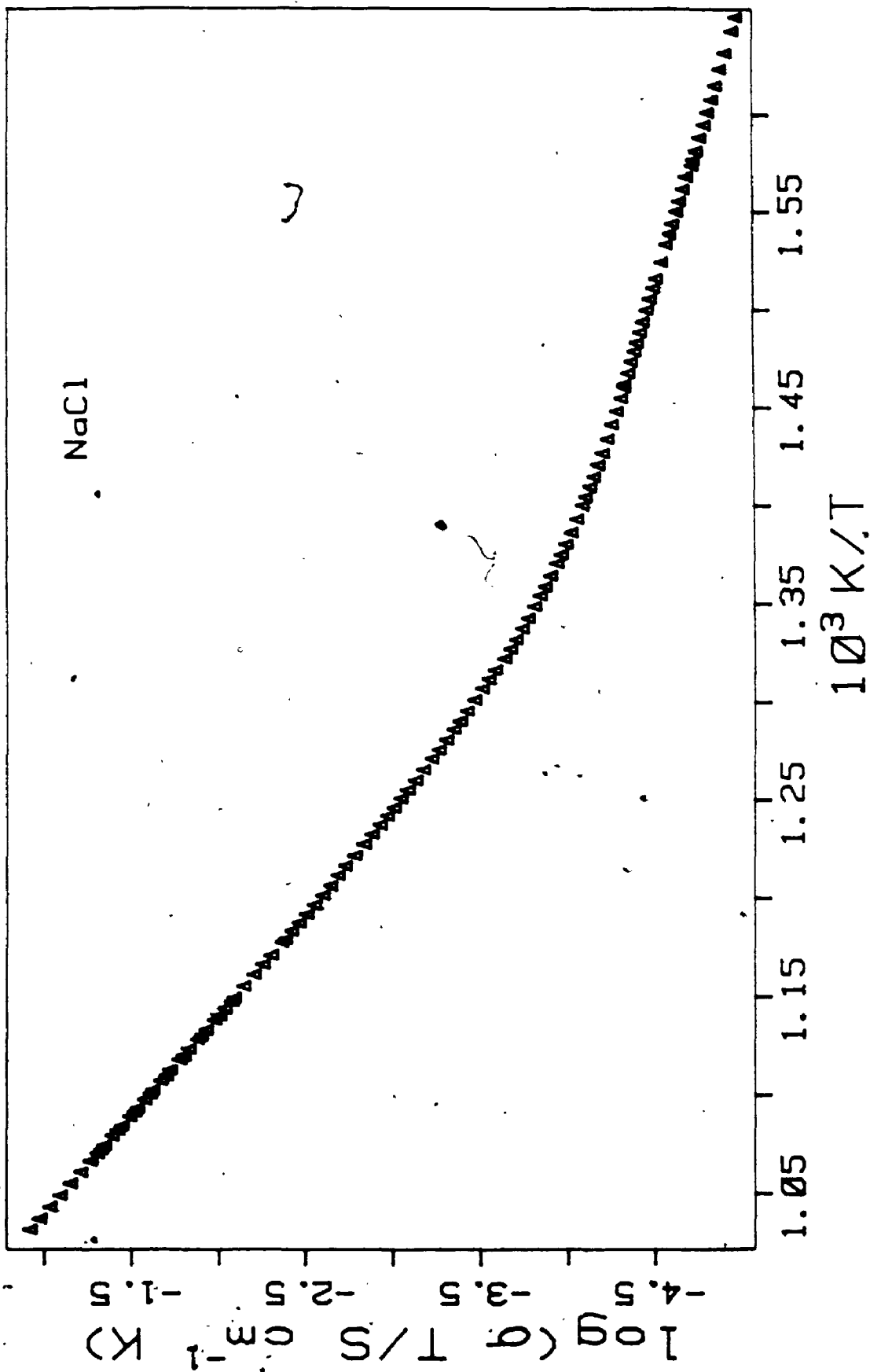


Figure 6-2: Arrhenius plot for three NaCl crystals doped with 360, 190, and 27 ppm strontium



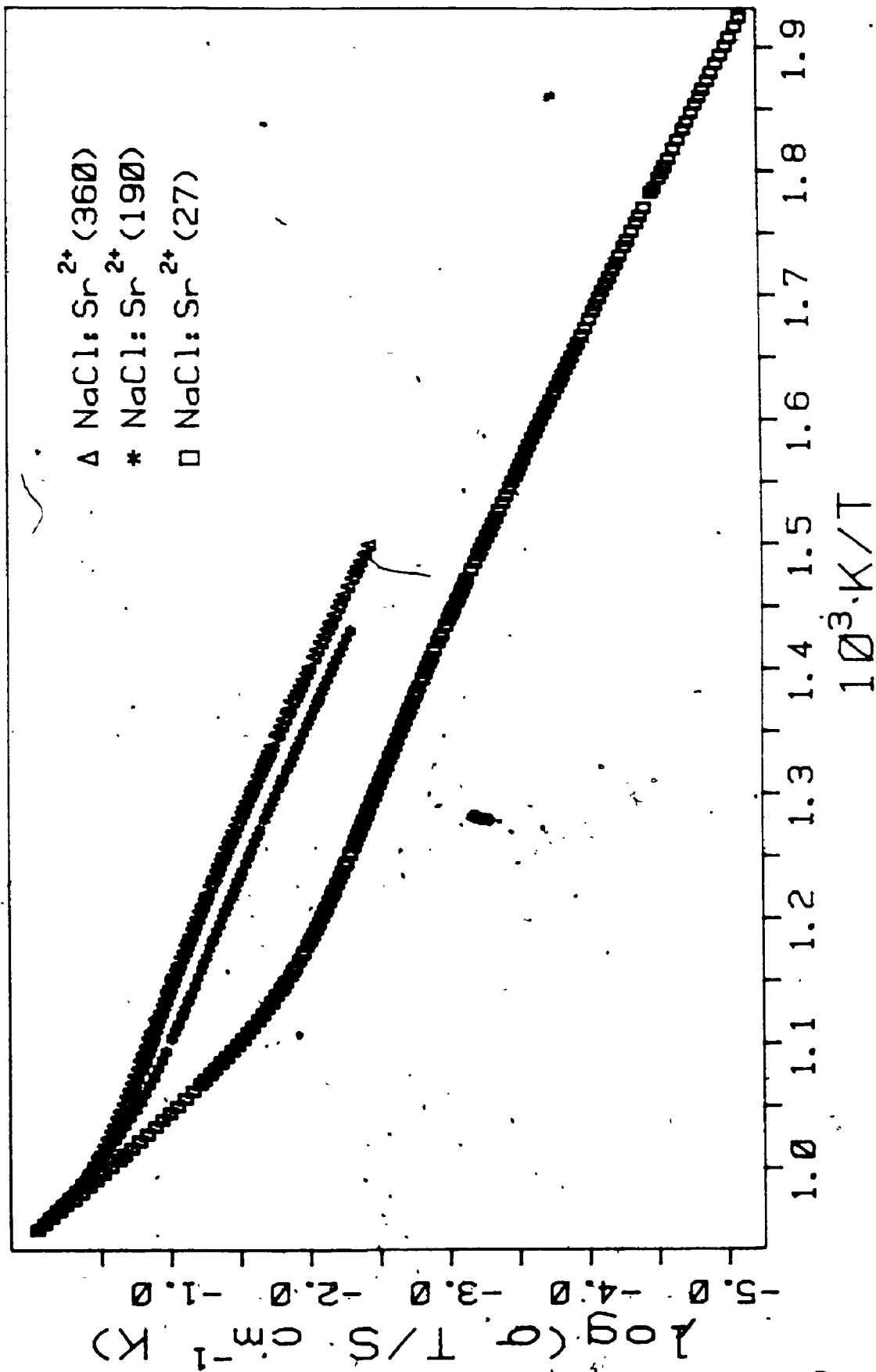


Figure 6-3: Arrhenius plots of pure NaCl and NaCl doped with 60 ppm S²⁻

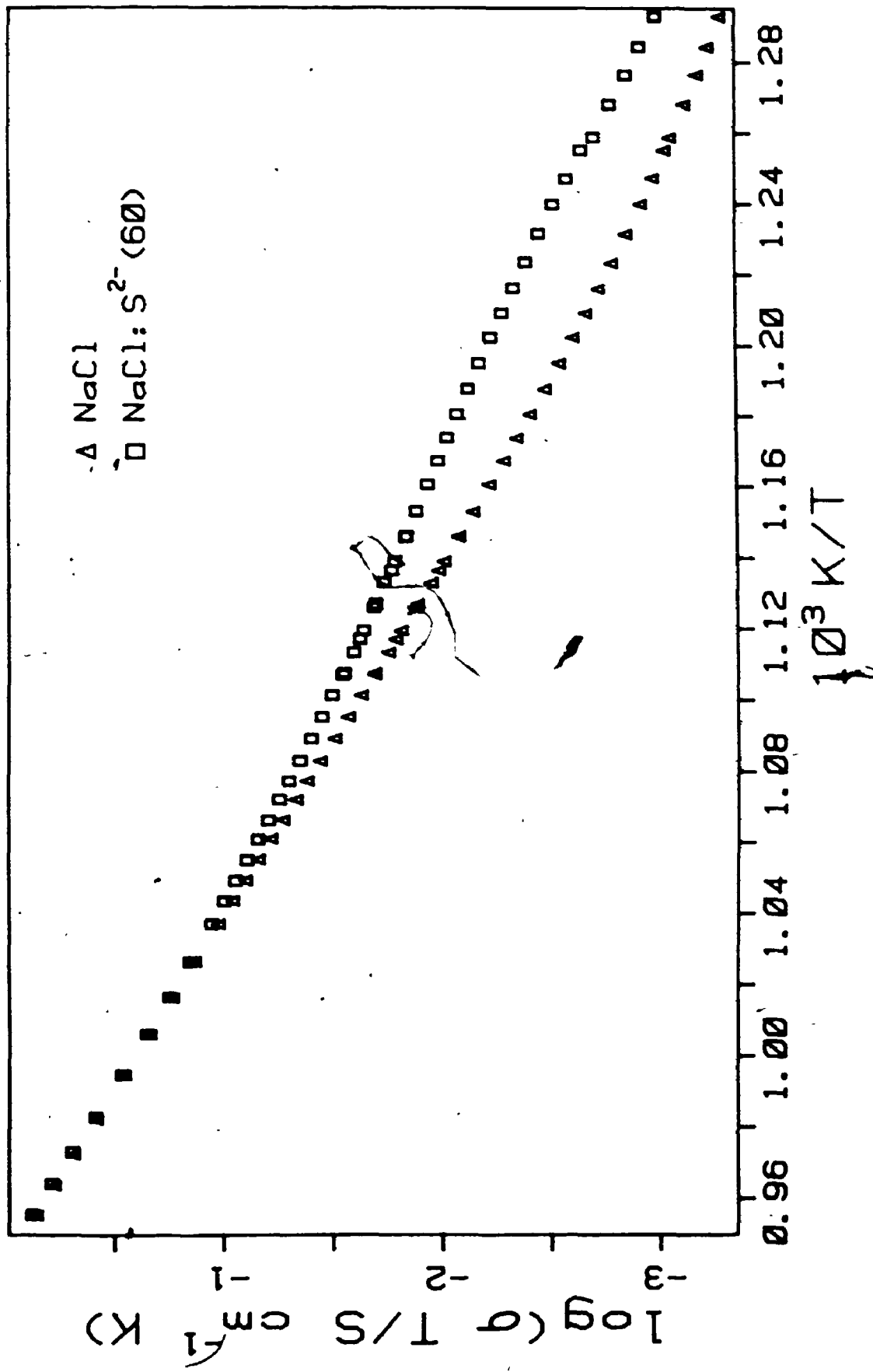
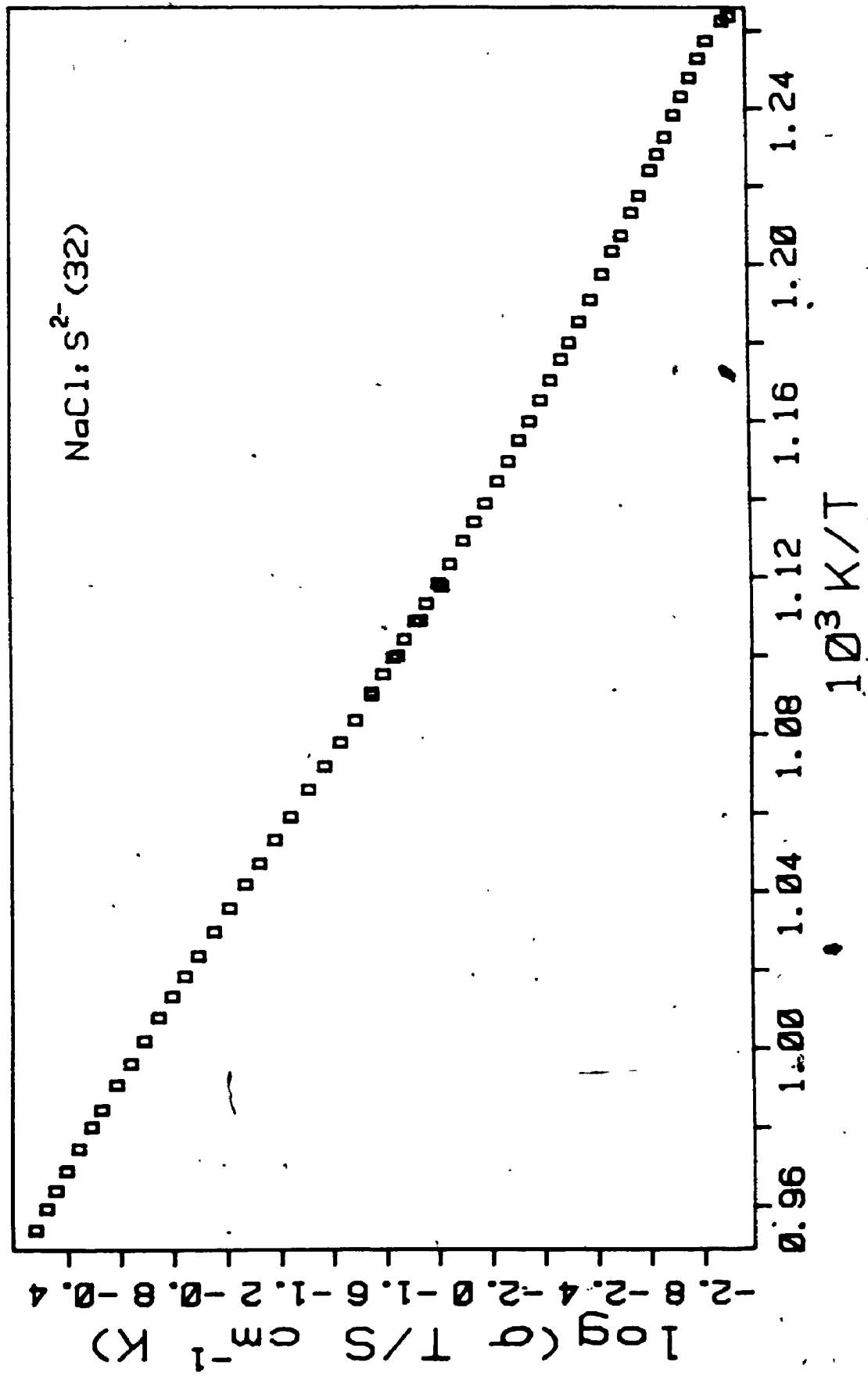


Figure 6-4: Arrhenius plot of NaCl doped with 32 ppm S²⁻



2

Figure 6-5: Arrhenius plots of pure NaCl and NaCl doped with 19 ppm S²⁻

—

—

60

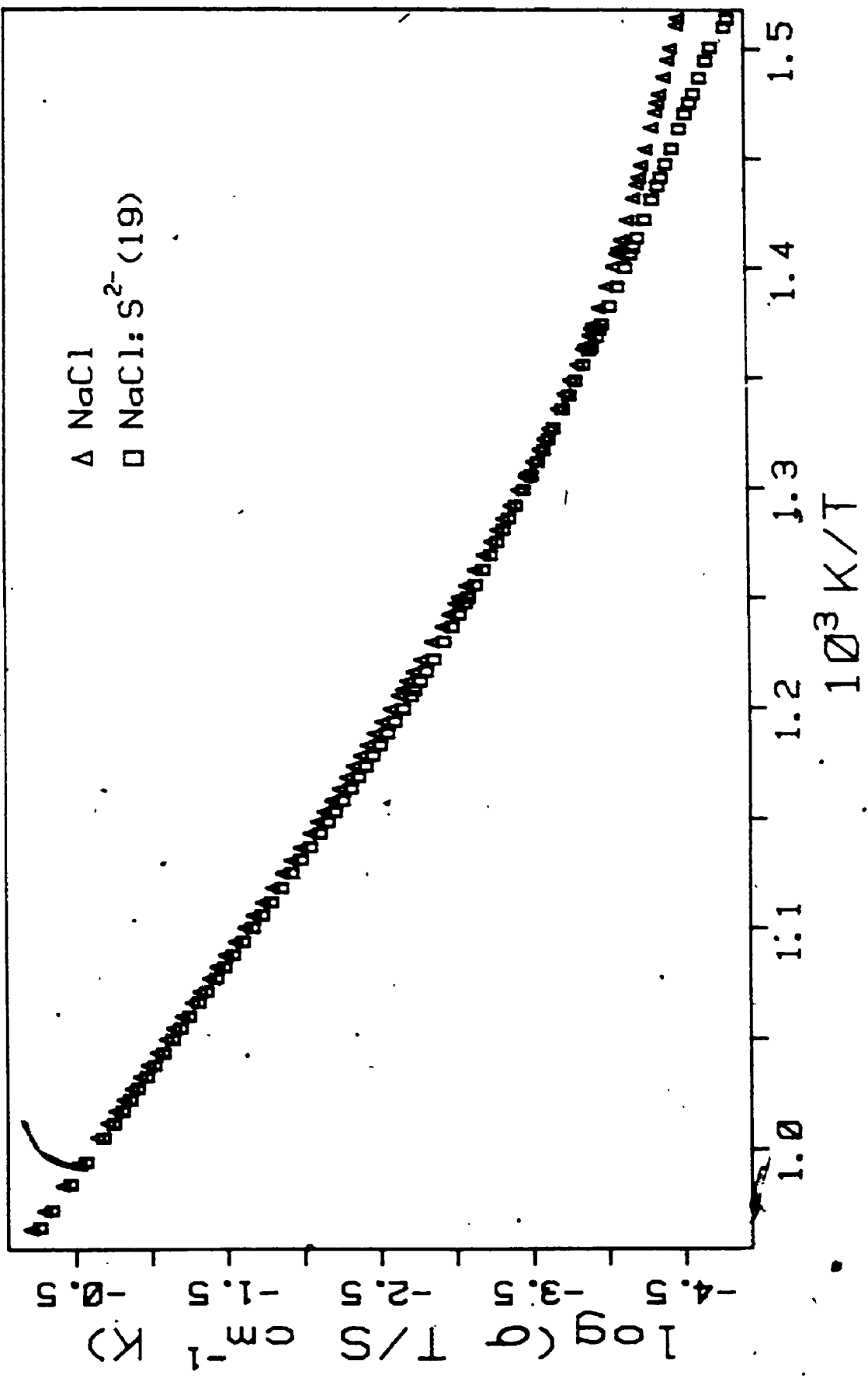


Figure 6-6: Arrhenius plots of pure NaCl and NaCl doped with 8.6 ppm S²⁻

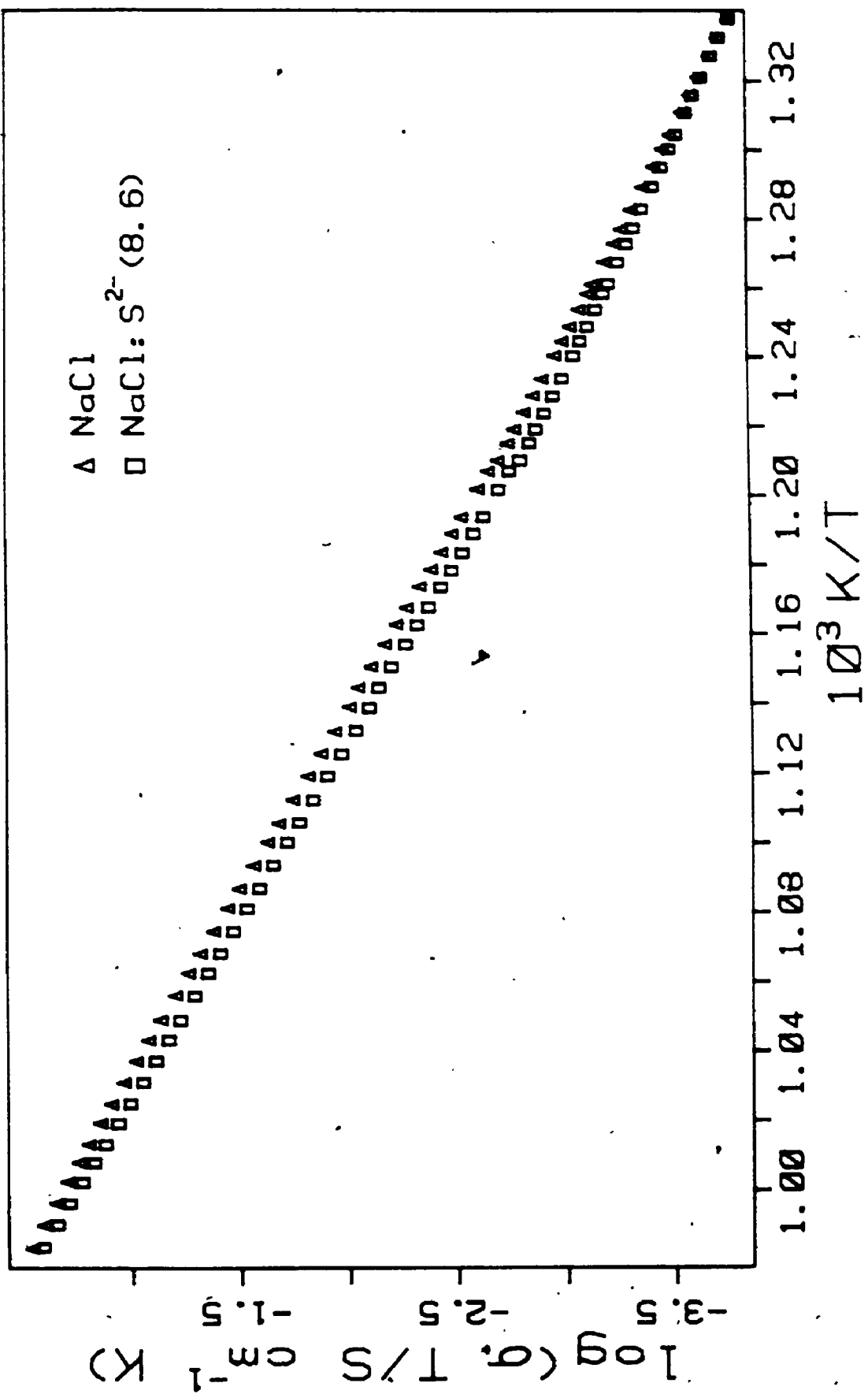


Figure 6-7: Plot of the ratio of the conductivities of NaCl doped with 60 ppm S^{2-} and pure NaCl

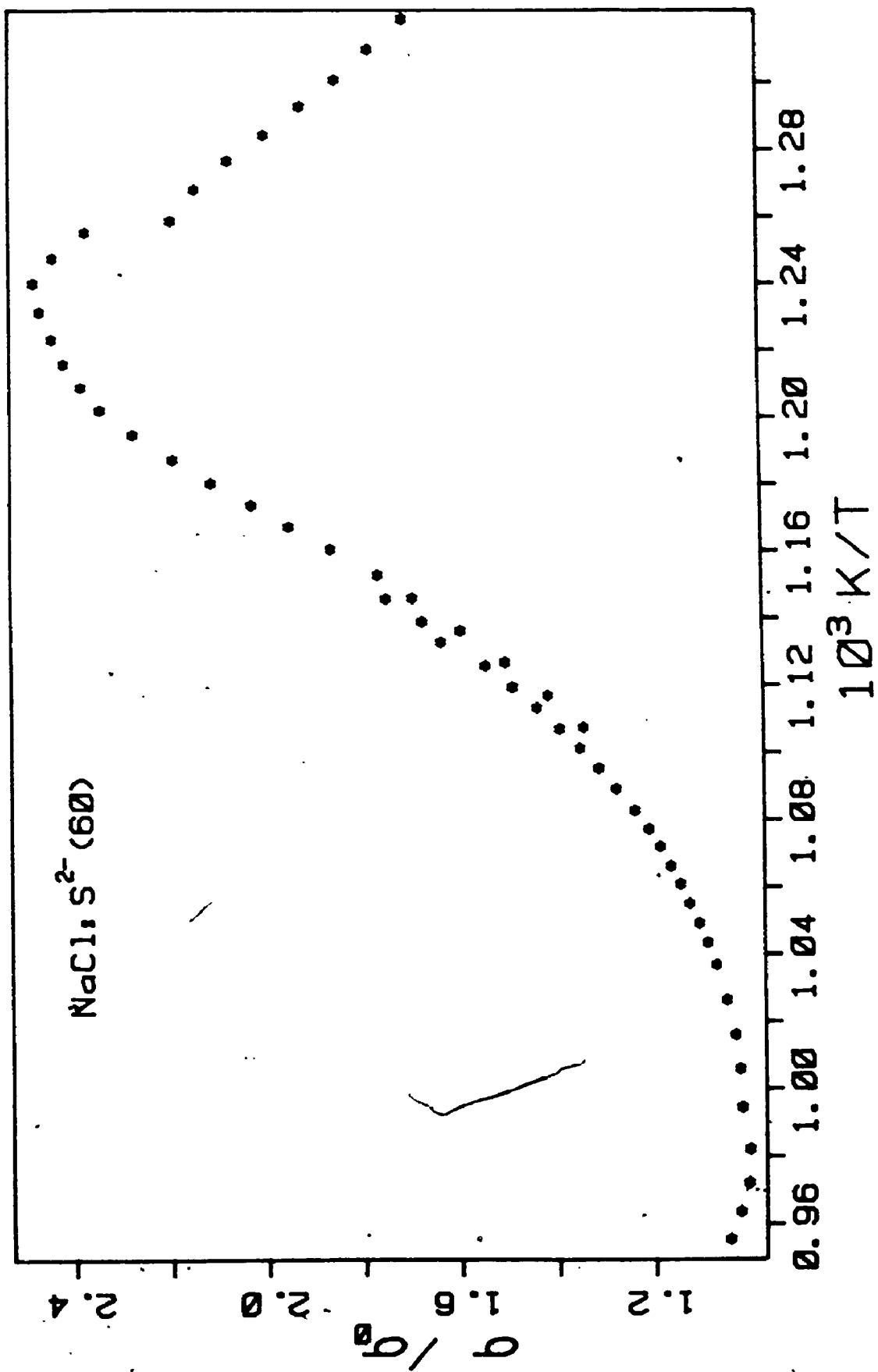


Figure 6-8: Plot of the ratio of the conductivities of NaCl doped with 19 ppm S^{2-} and pure NaCl

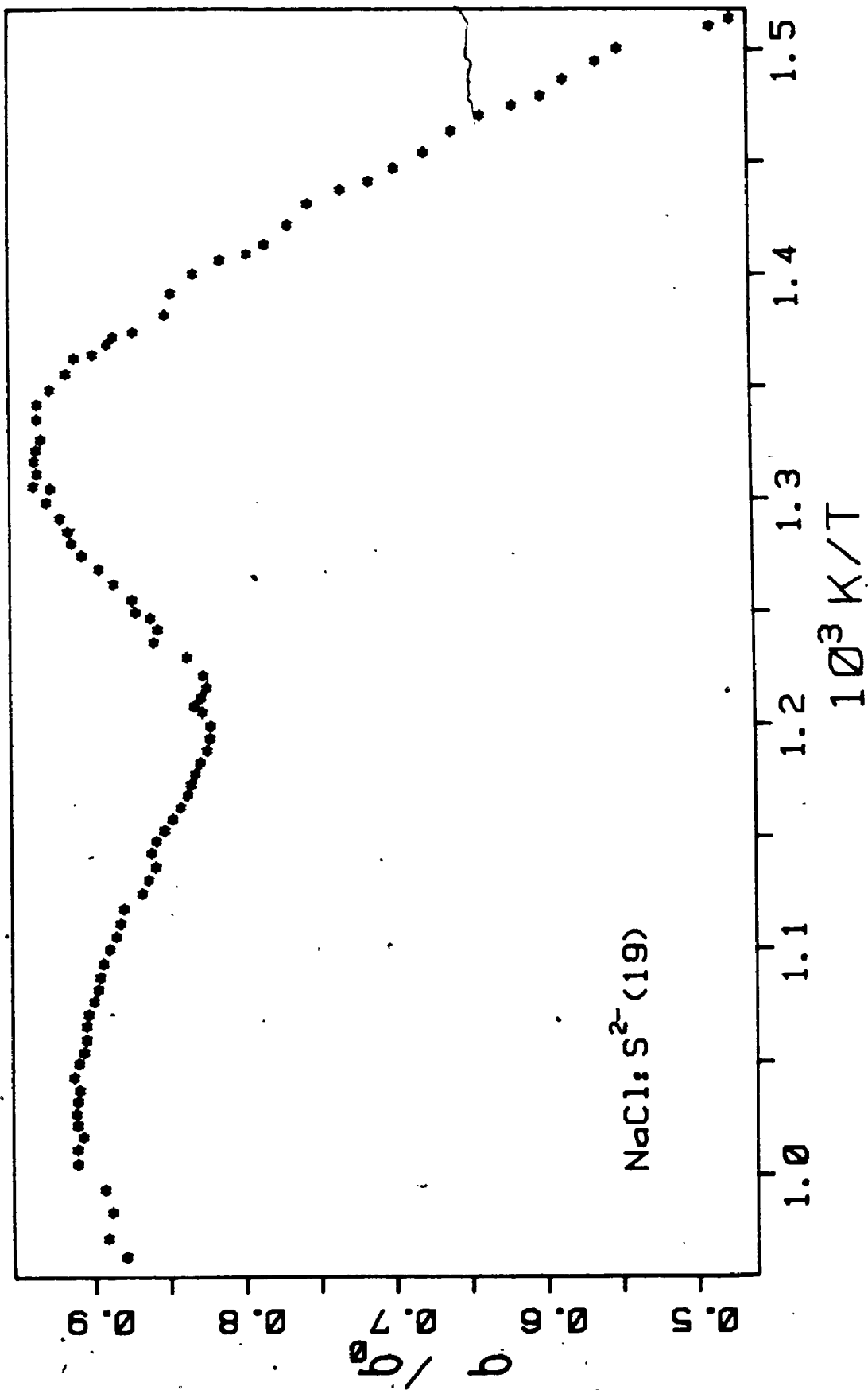


Figure 6-9: Residuals from fitting of pure NaCl crystal

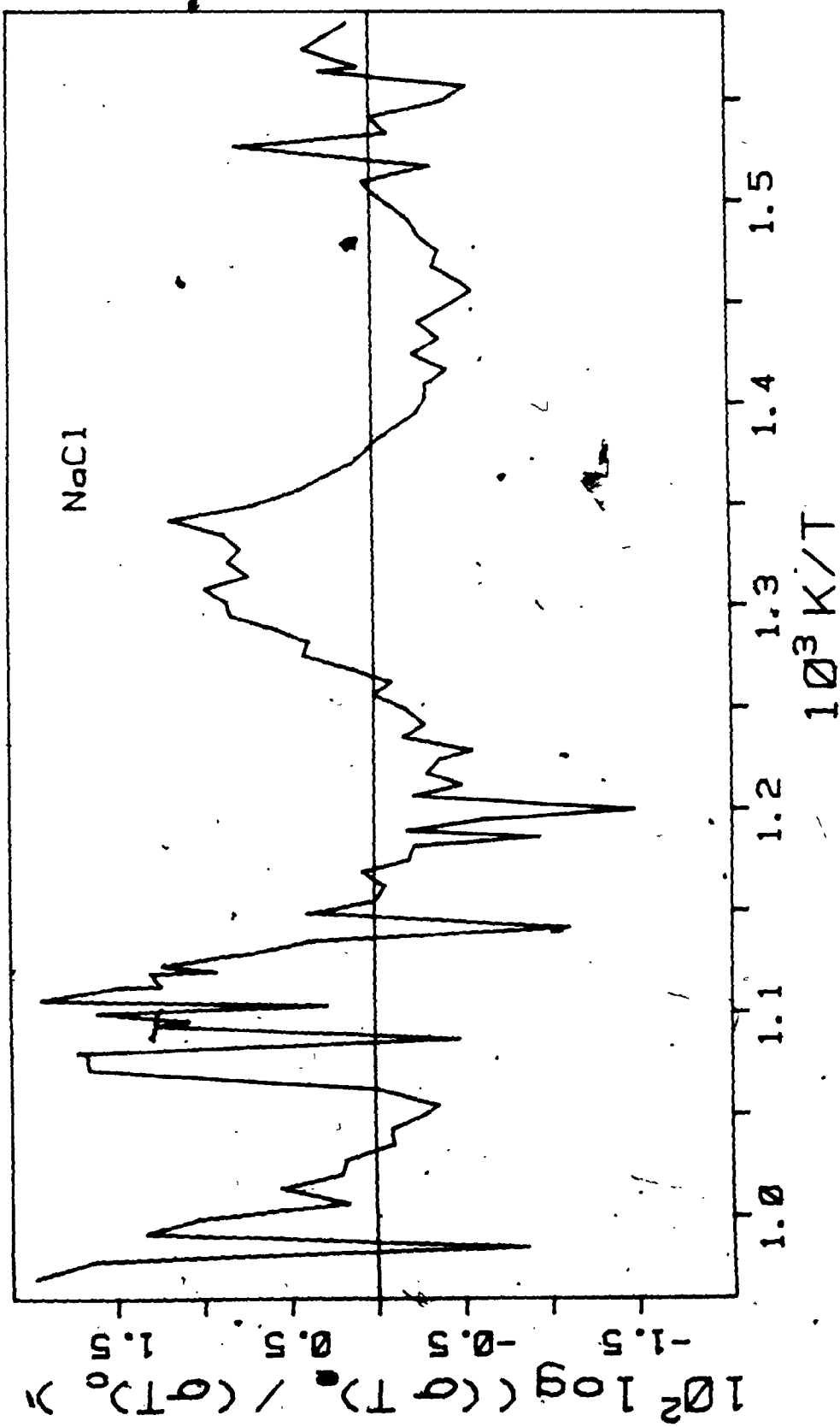


Figure 6-10: Residuals from fitting of NaCl crystal doped with 27 ppm Sr^{2+}

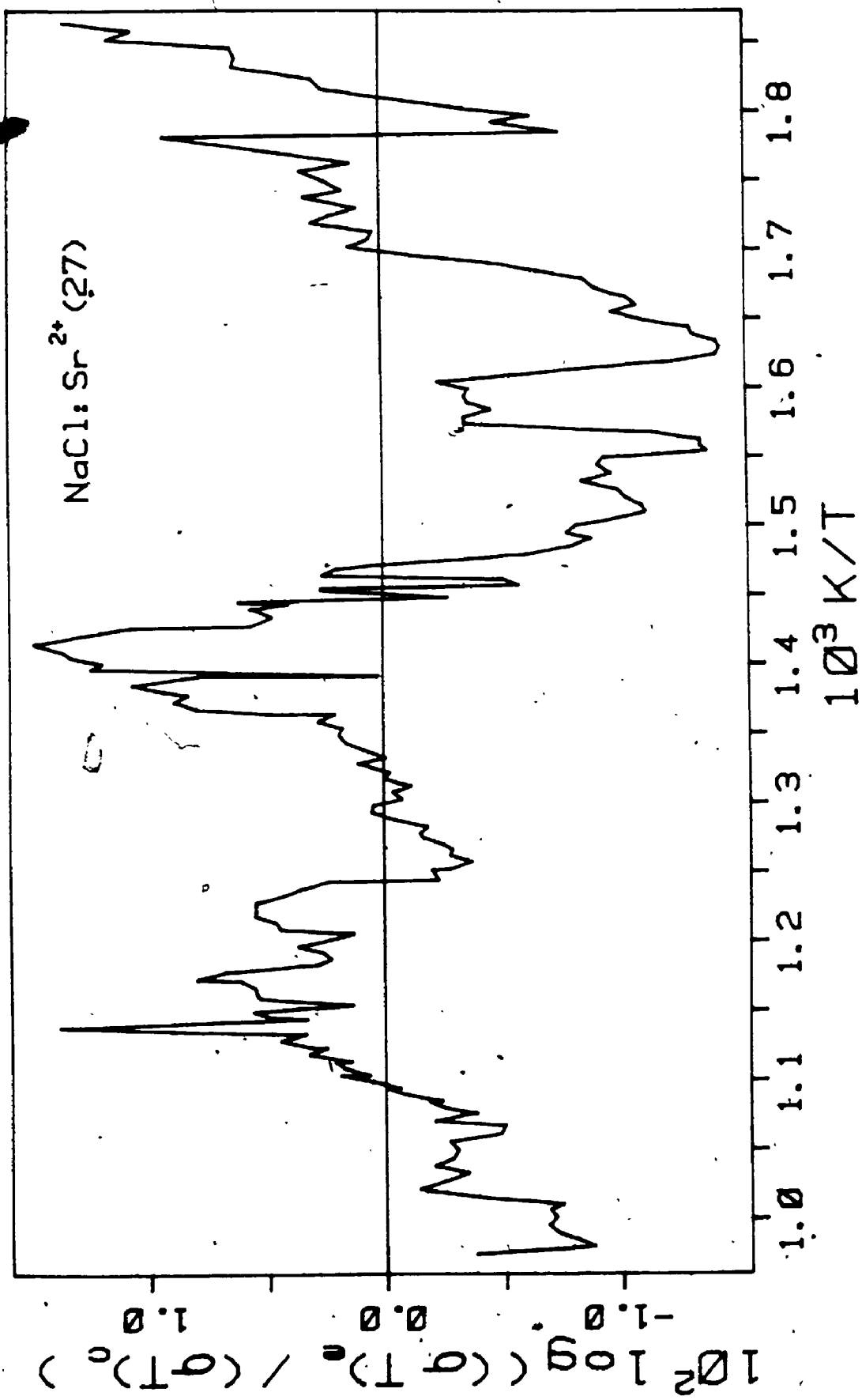
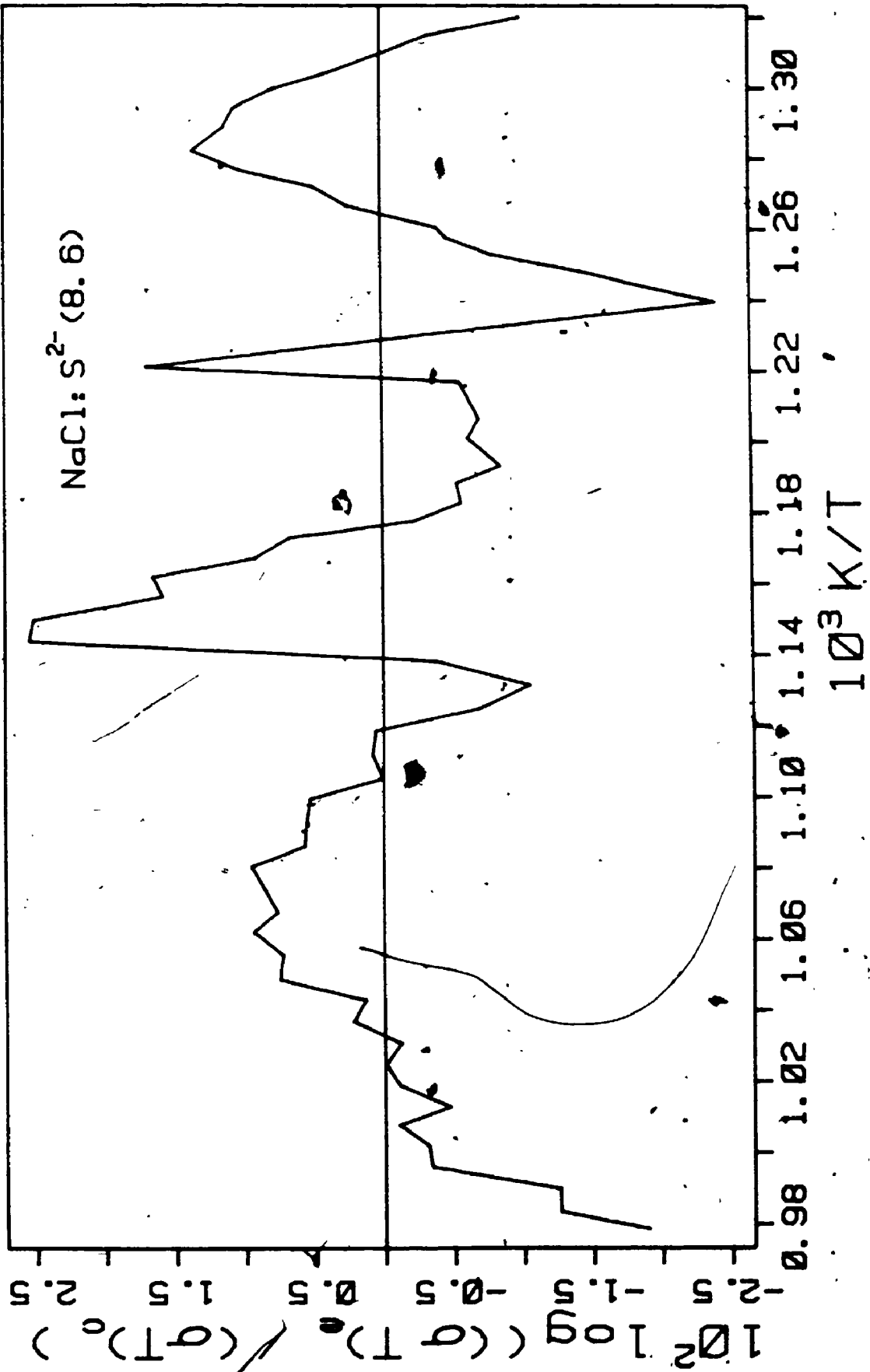
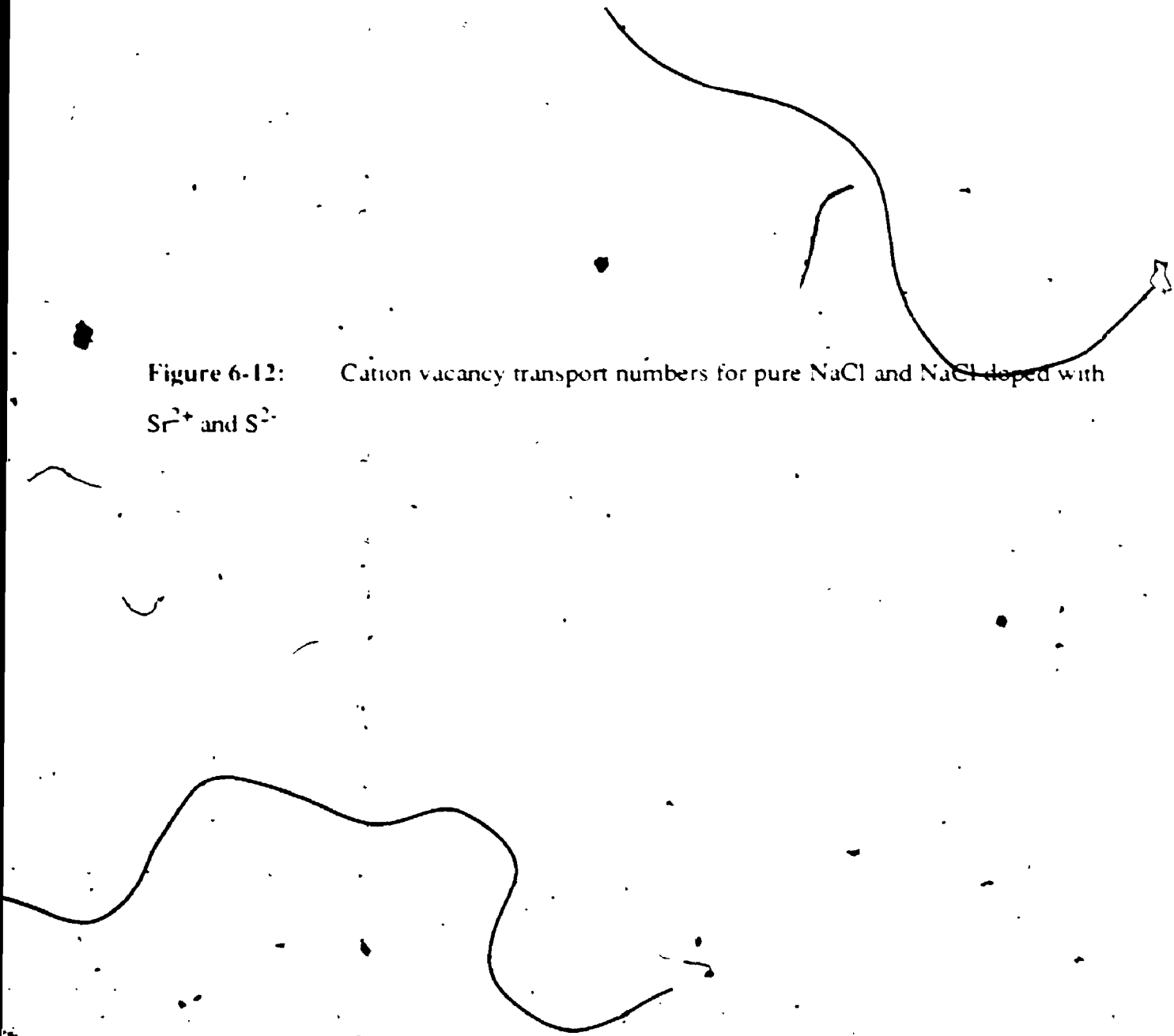


Figure 6-11: Residuals from fitting of NaCl crystal doped with 8.6 ppm S²⁻



sk

Figure 6-12: Cation vacancy transport numbers for pure NaCl and NaCl doped with Sr^{2+} and S^{2-}



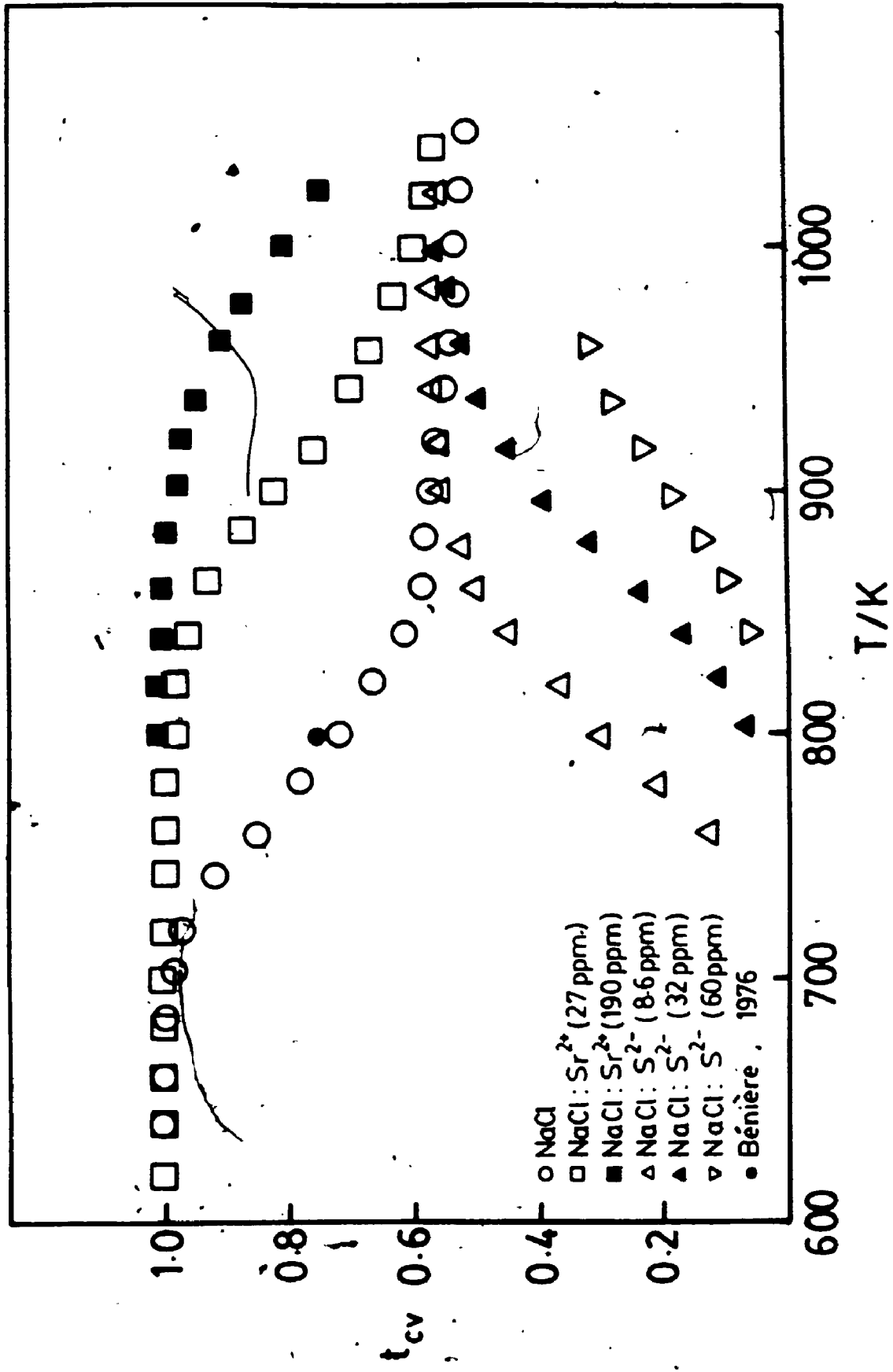


Figure 6-13: Fraction of complexed impurity in Sr^{2+} -doped NaCl crystals

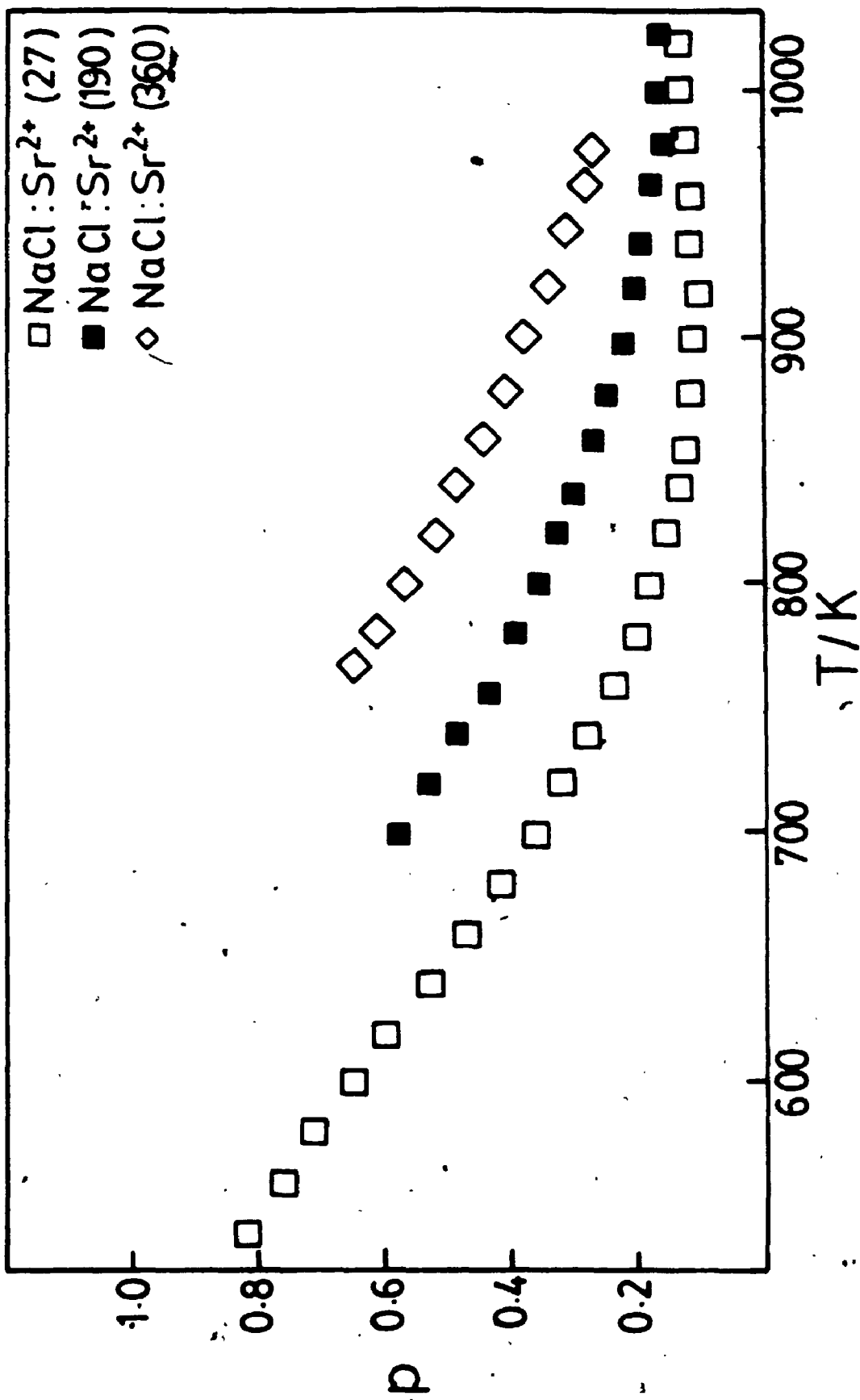


Figure 6-14: Fraction of complexed impurity in S^{2-} -doped NaCl crystals. The broken line represents values calculated from the final parameters.

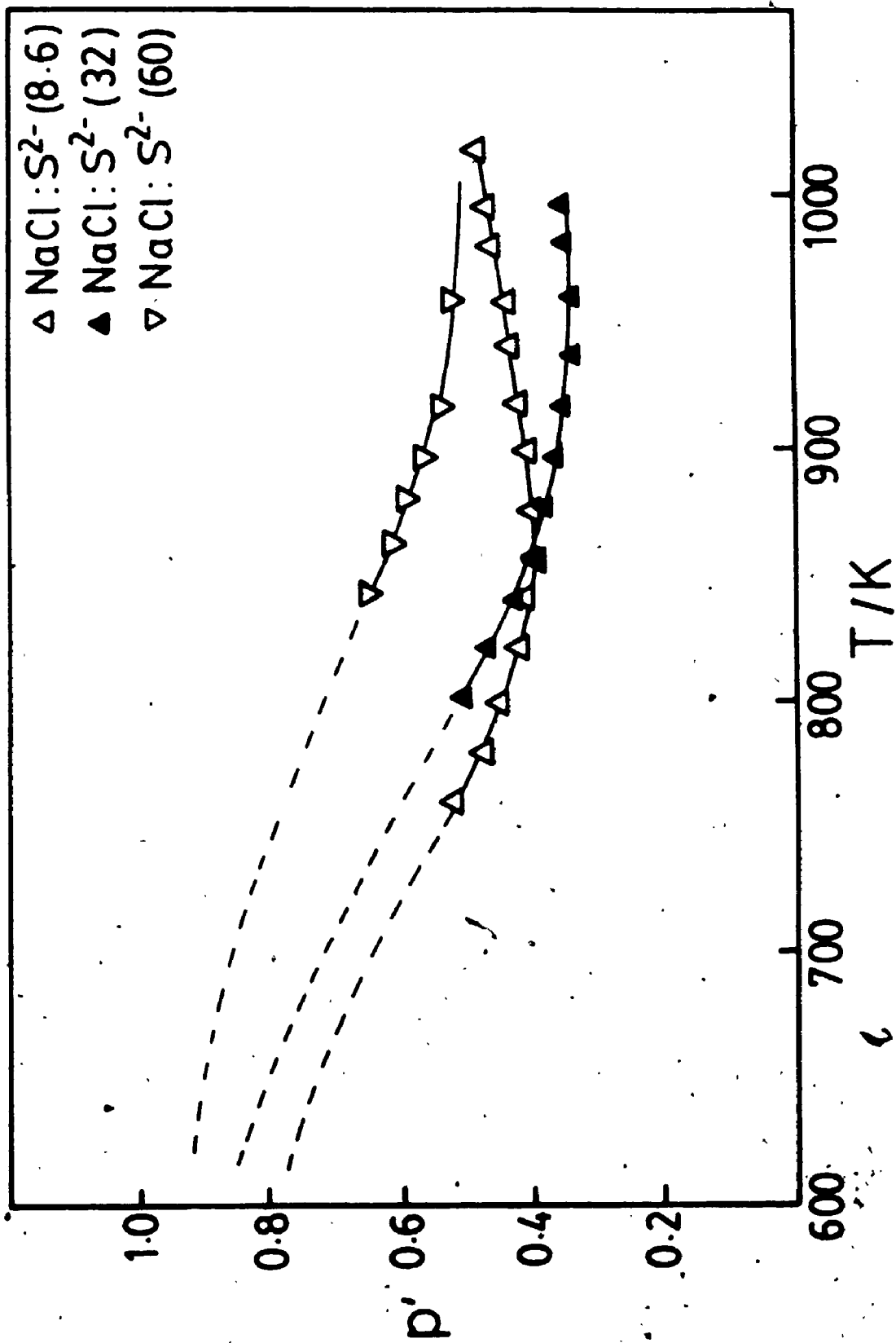
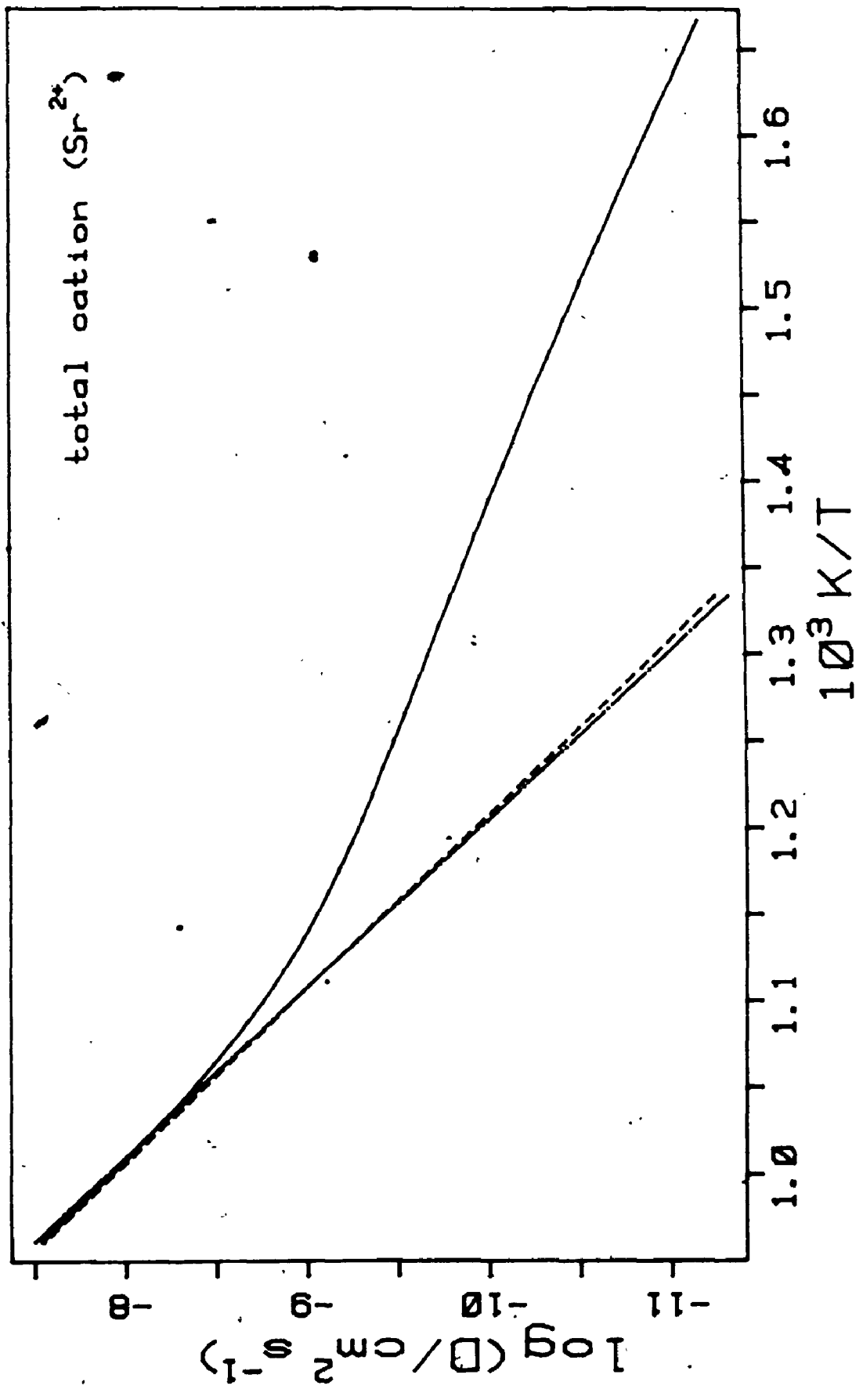


Figure 6-15: Total cation diffusion in NaCl doped with 27 ppm Sr^{2+} . The evenly broken line represents B ni re's²¹ data, and the unevenly broken line represents Rothman's¹⁸ data, for pure NaCl. The diffusion coefficients calculated from the results of the present investigation are given by the solid line.

5



631

Figure 6-16: Cation diffusion via single vacancies in NaCl doped with 27 ppm Sr^{2+} . The evenly broken line represents Bènière's²¹ data for a pure crystal and the unevenly broken represents his data for a strontium-doped crystal. The diffusion coefficients calculated from the results of the present investigation are given by the solid line.

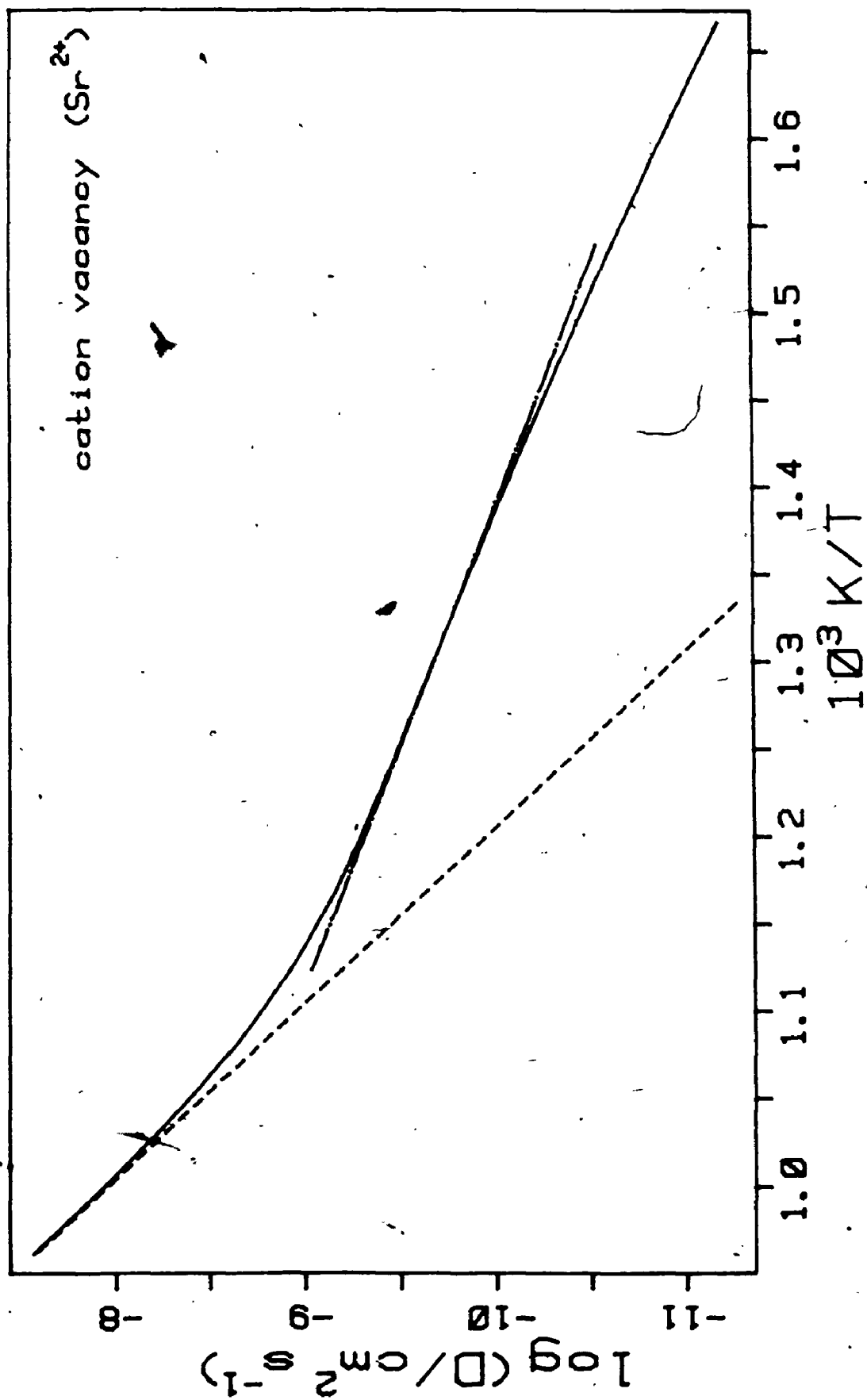




Figure 6-17: Cation diffusion via vacancy pairs in NaCl doped with 27 ppm Sr^{2+} . The broken line represents B ni re's²⁰ data and the solid line represents the diffusion coefficients calculated from the results of the present investigation.

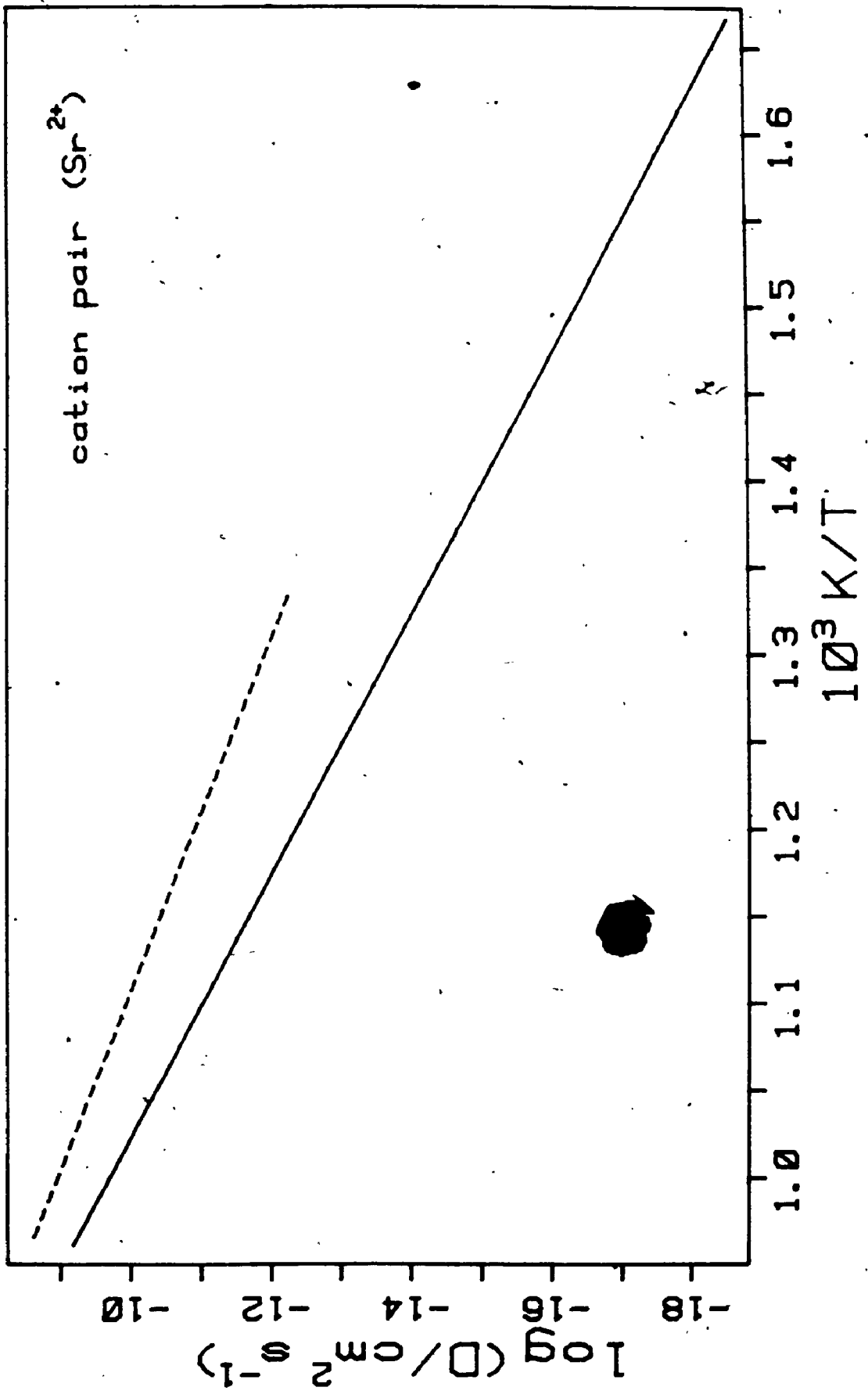




Figure 6-18: Total anion diffusion in NaCl doped with 27 ppm Sr^{2+} . The broken line represents B ni re's²¹ data for pure NaCl and the diffusion coefficients calculated from the results of the present investigation are given by the solid line.

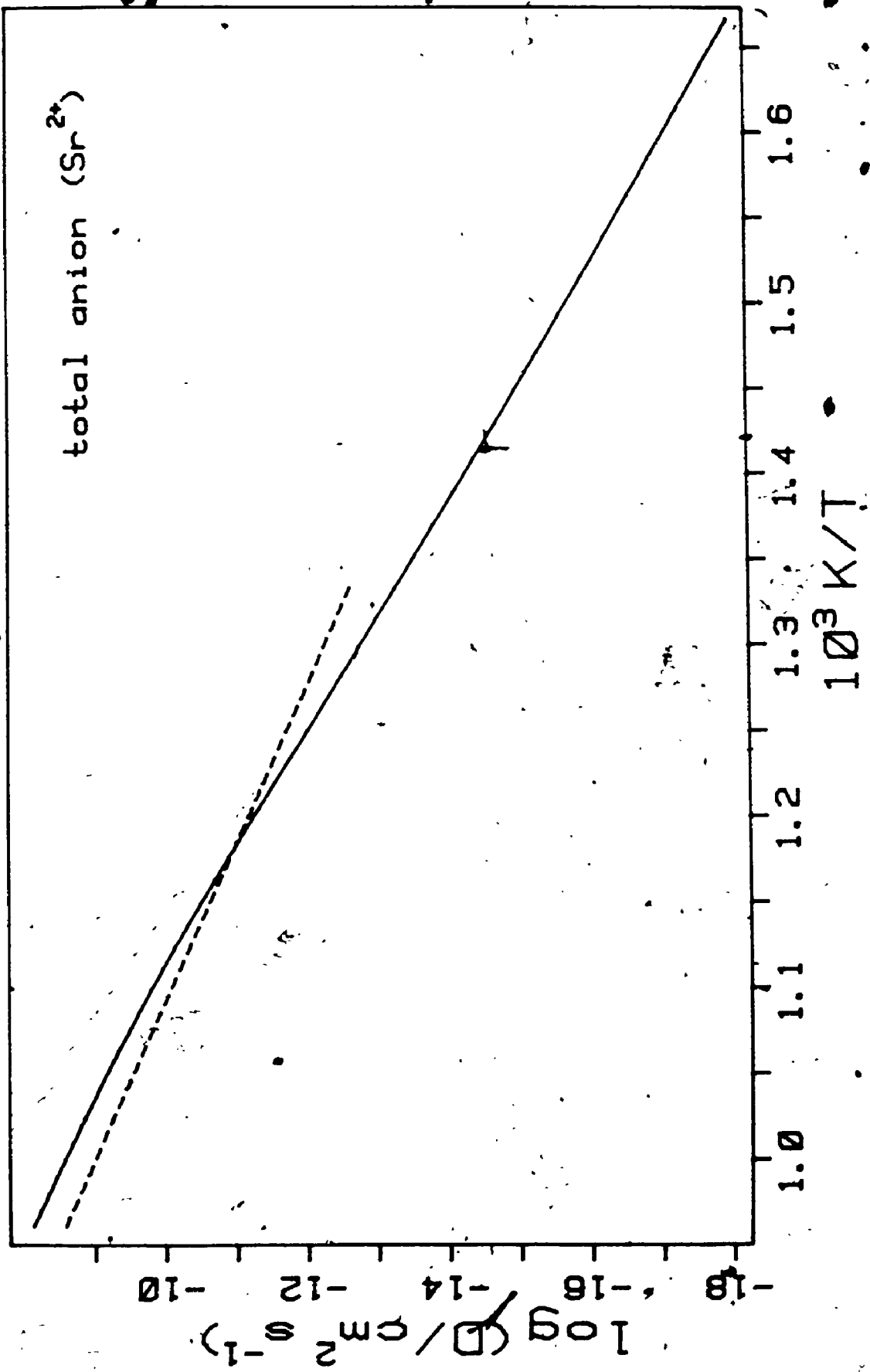


Figure 6-19: Anion diffusion via single vacancies in NaCl doped with 27 ppm Sr^{2+} . Bénére's²⁴ data for pure NaCl are represented by the broken line and the diffusion coefficients calculated from the results of the present investigation are given by the solid line.



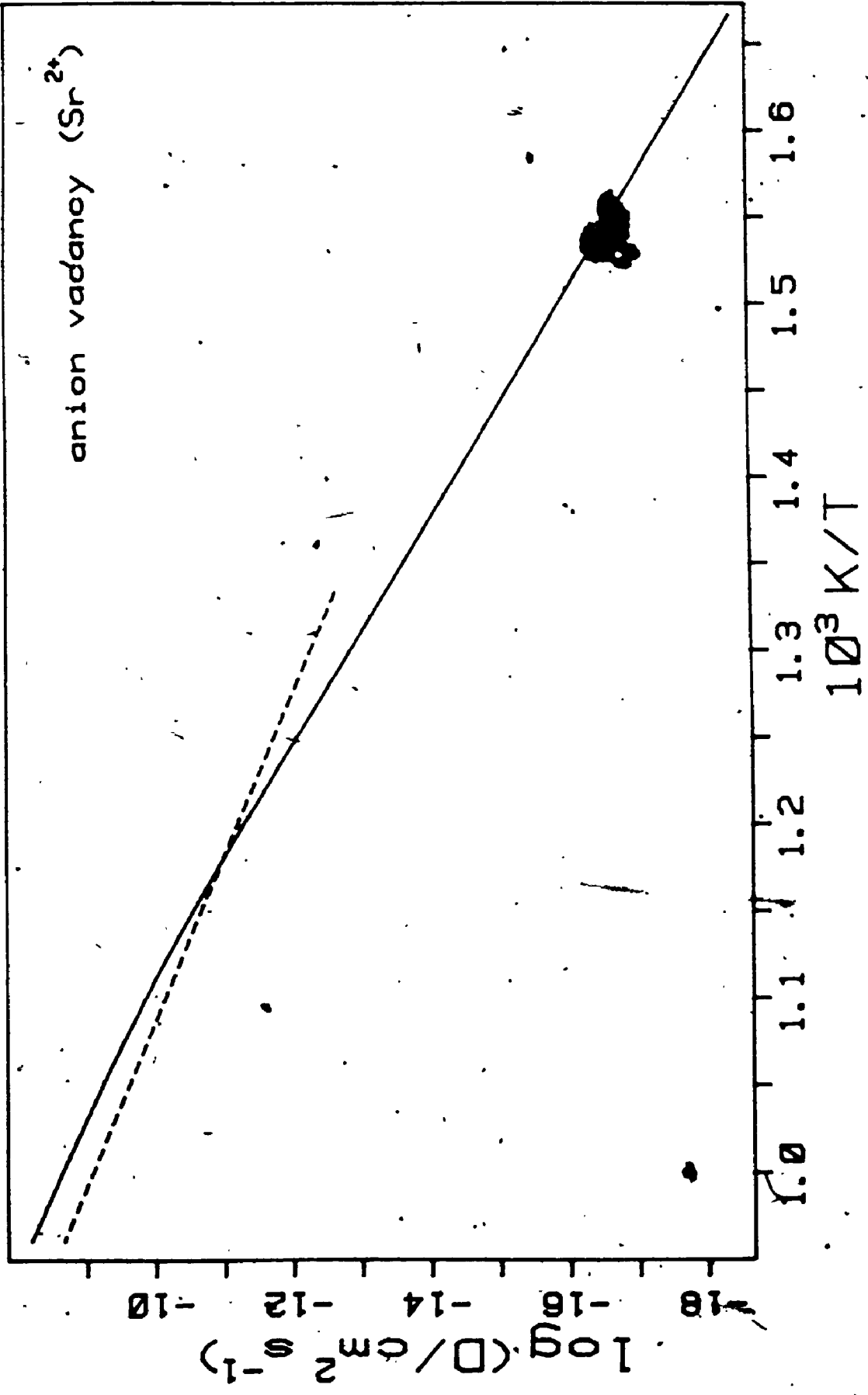


Figure 6-20: Anion diffusion via vacancy pairs in NaCl doped with 27 ppm Sr^{2+}
Bénière's²⁰ data are represented by the broken line and the diffusion coefficients
calculated from the results of the present investigation are given by the solid line

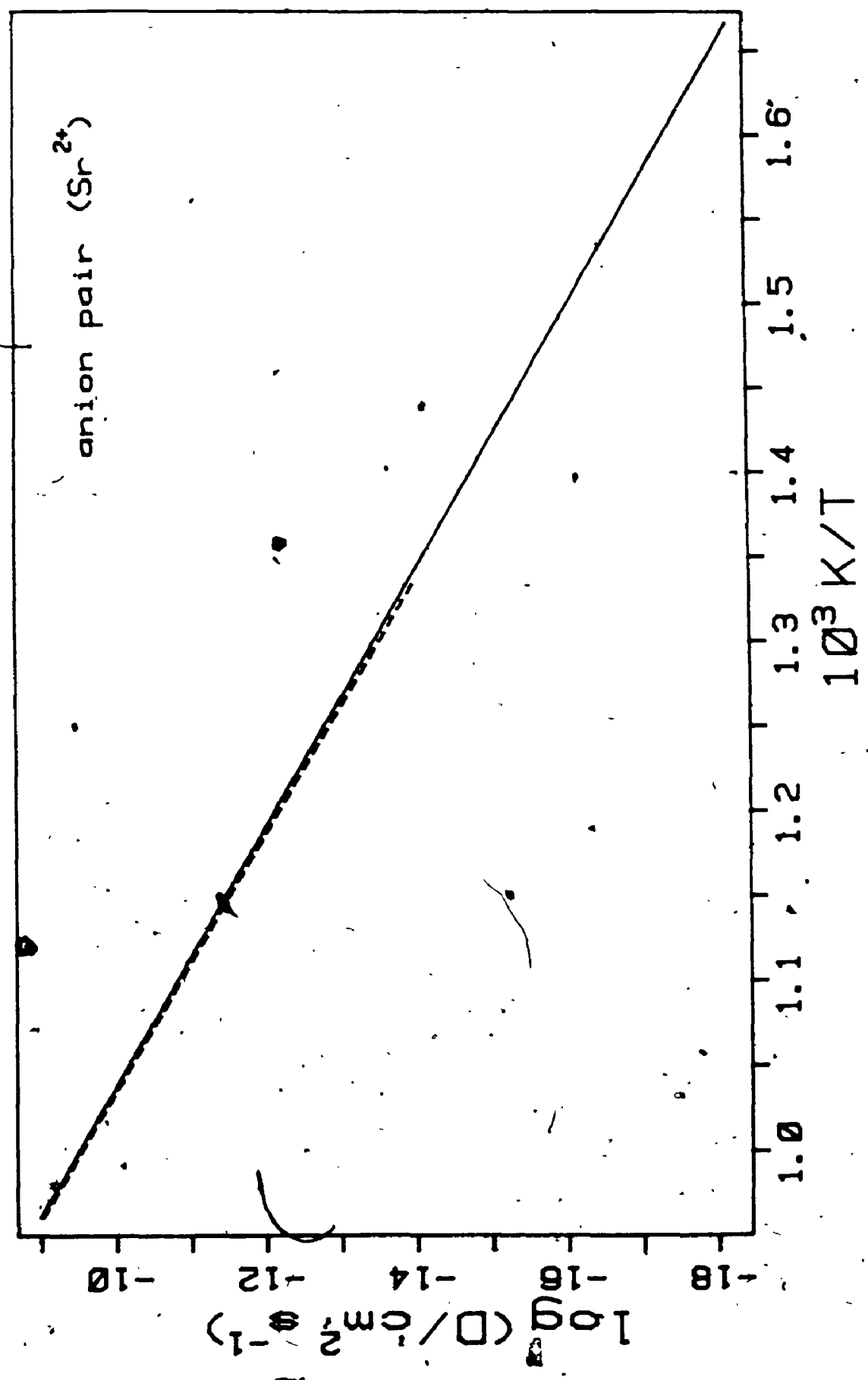


Figure 6-21: Total cation diffusion in NaCl doped with 19 ppm S^{2-} . The evenly broken line represents Bénére's²¹ data and the unevenly broken line represents Rothman's¹⁸ data, for pure NaCl. The diffusion coefficients calculated from the results of the present investigation are given by the solid line.

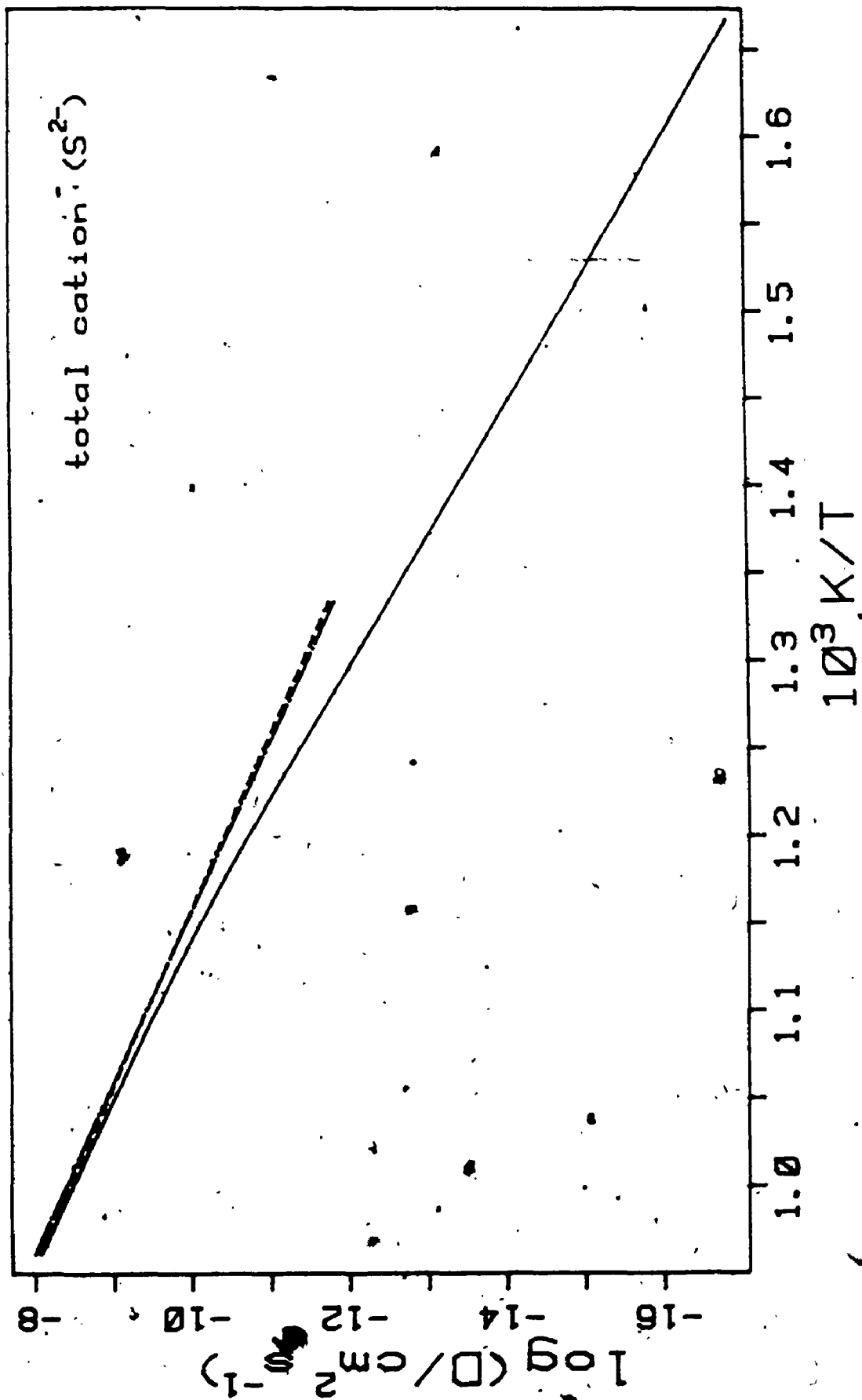


Figure 6-22: Cation diffusion via single vacancies in NaCl doped with 19 ppm S^{2-} . The broken line represents B ni re's²¹ data for pure NaCl and the solid line represents the diffusion coefficients calculated from the results of the present investigation.

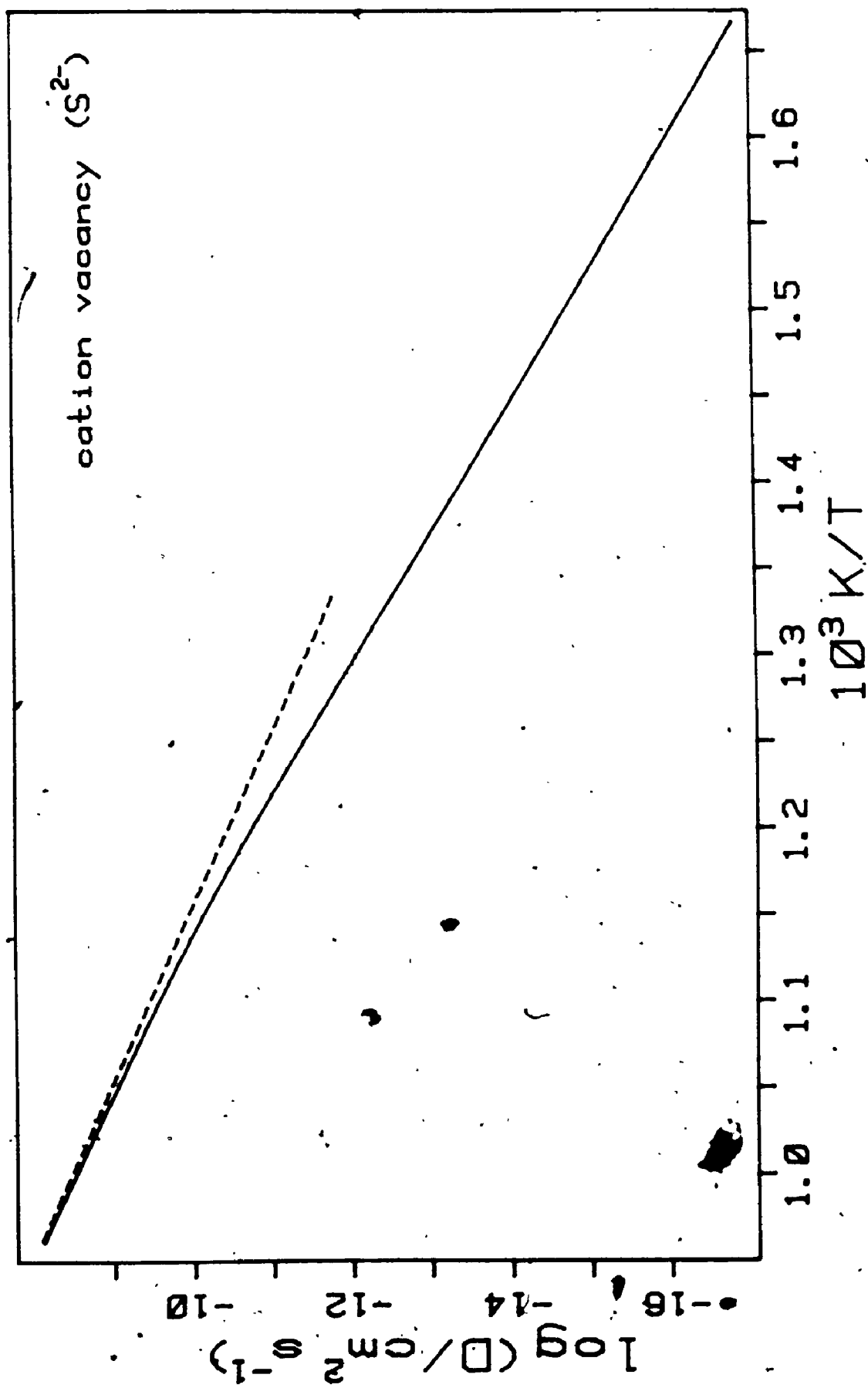


Figure 6-23: Cation diffusion via vacancy pairs in NaCl doped with 19 ppm S^{2-} . The broken line represents Bénéière's²⁰ data for pure NaCl and the solid line represents diffusion coefficients calculated from the results of the present investigation.

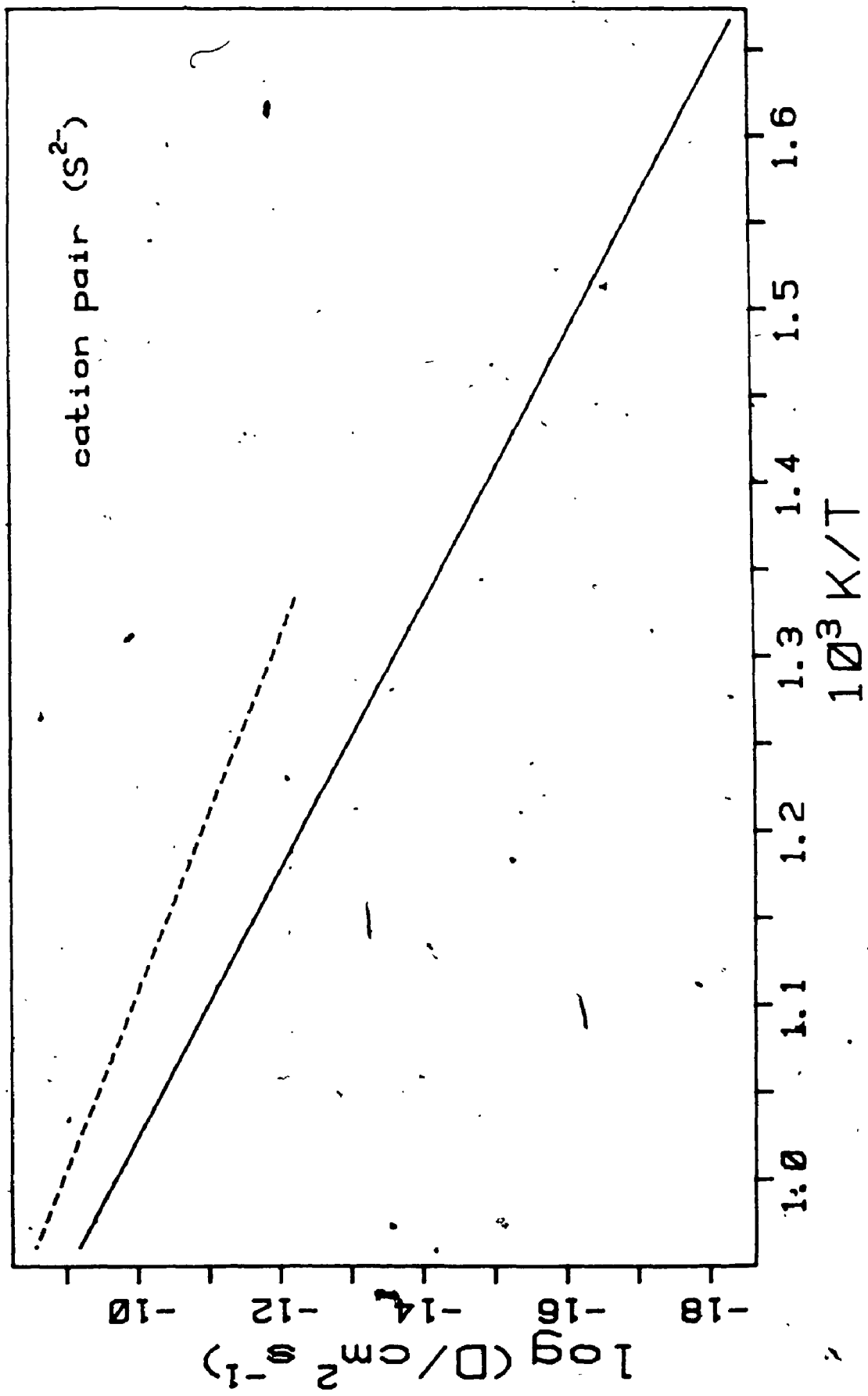
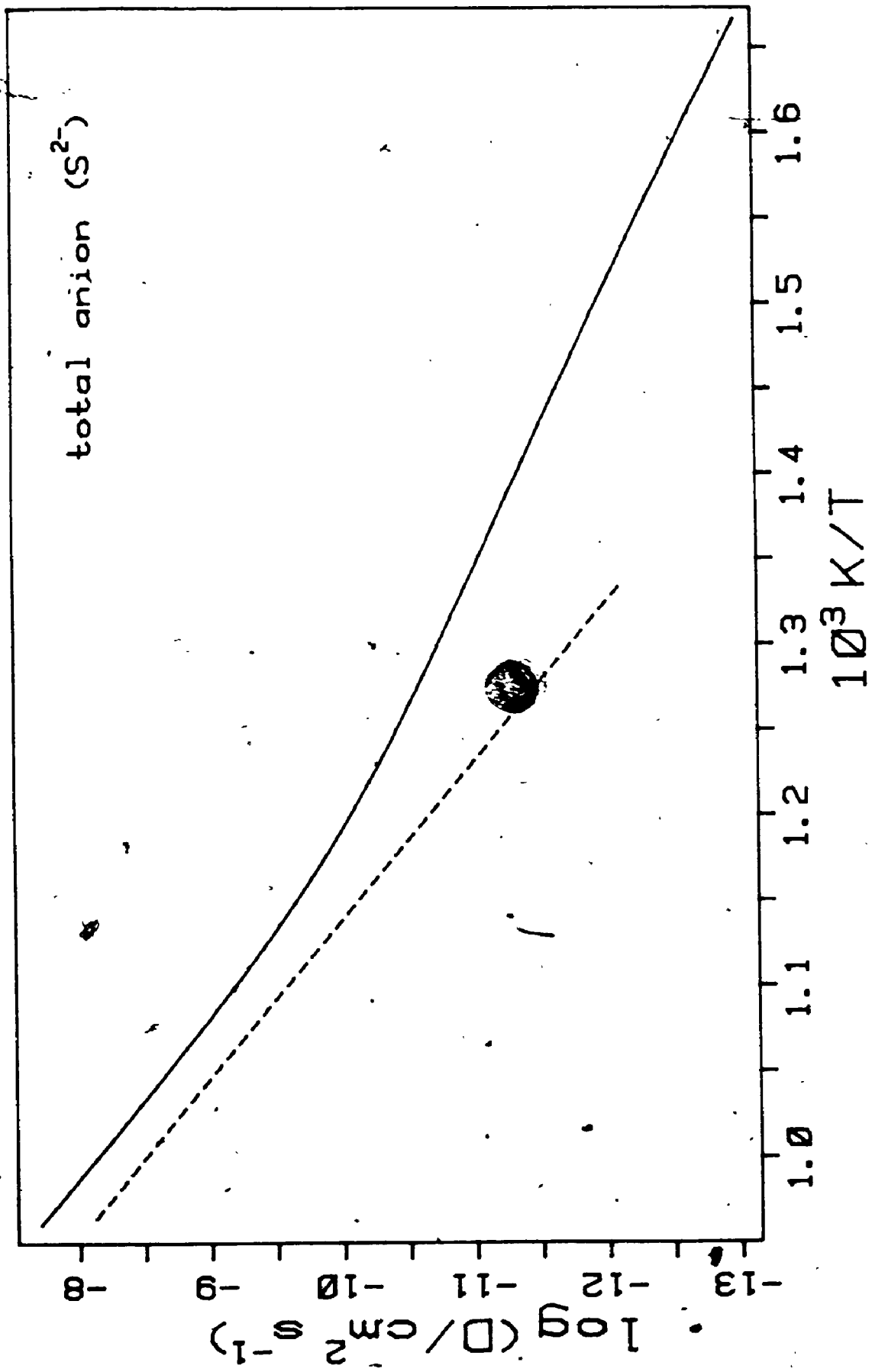


Figure 6-24: Total anion diffusion in NaCl doped with 19 ppm S^{2-} . The broken line represents B ni re's²¹ data for pure NaCl and the solid line represents diffusion coefficients calculated from the results of the present investigation.



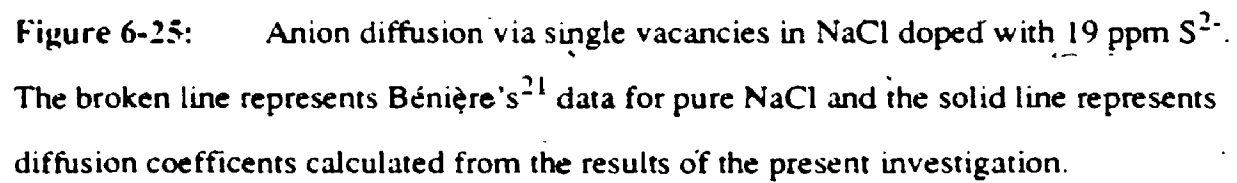
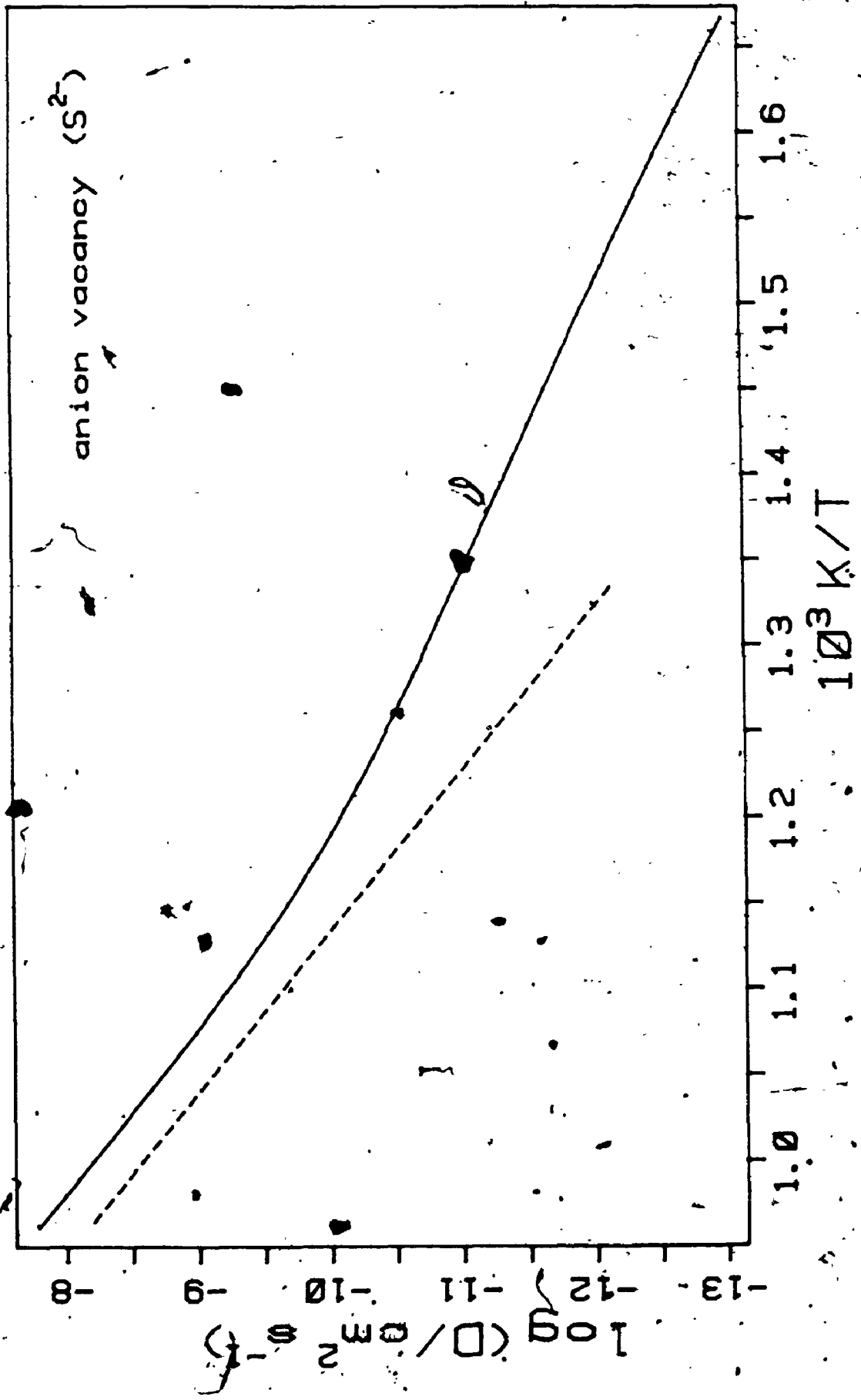


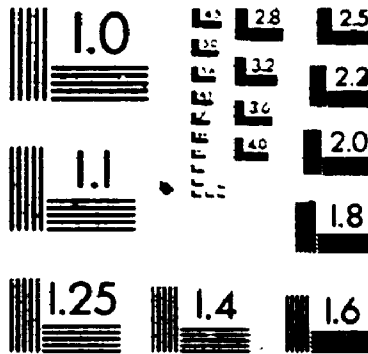
Figure 6-25: Anion diffusion via single vacancies in NaCl doped with 19 ppm S^{2-} . The broken line represents Bènière's²¹ data for pure NaCl and the solid line represents diffusion coefficients calculated from the results of the present investigation.



3

of/de

3



METRO

381

Figure 6-26: Anion diffusion via vacancy pairs in NaCl doped with 19 ppm S^{2-} .
The broken line represents Bènière's²⁰ data and the solid line represents the diffusion coefficients calculated from the results of the present investigation

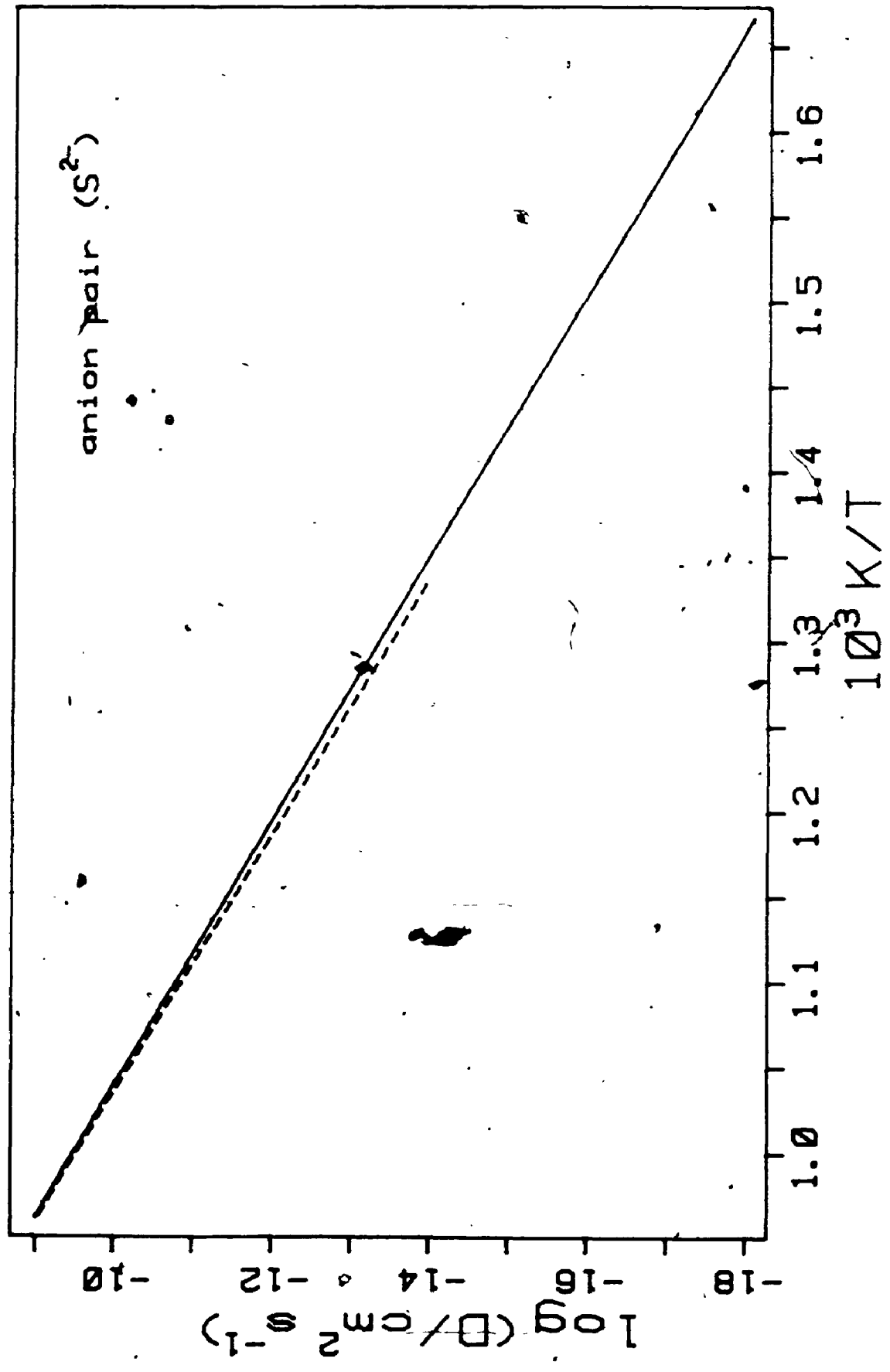


Figure 6-27: Total cation diffusion in nominally pure NaCl calculated using the average parameter set. The evenly broken line represents B ni re's²¹ data and the unevenly broken line represents Rothman's¹⁸ data, for pure NaCl. The diffusion coefficients calculated from the results of the present investigation are given by the solid line.

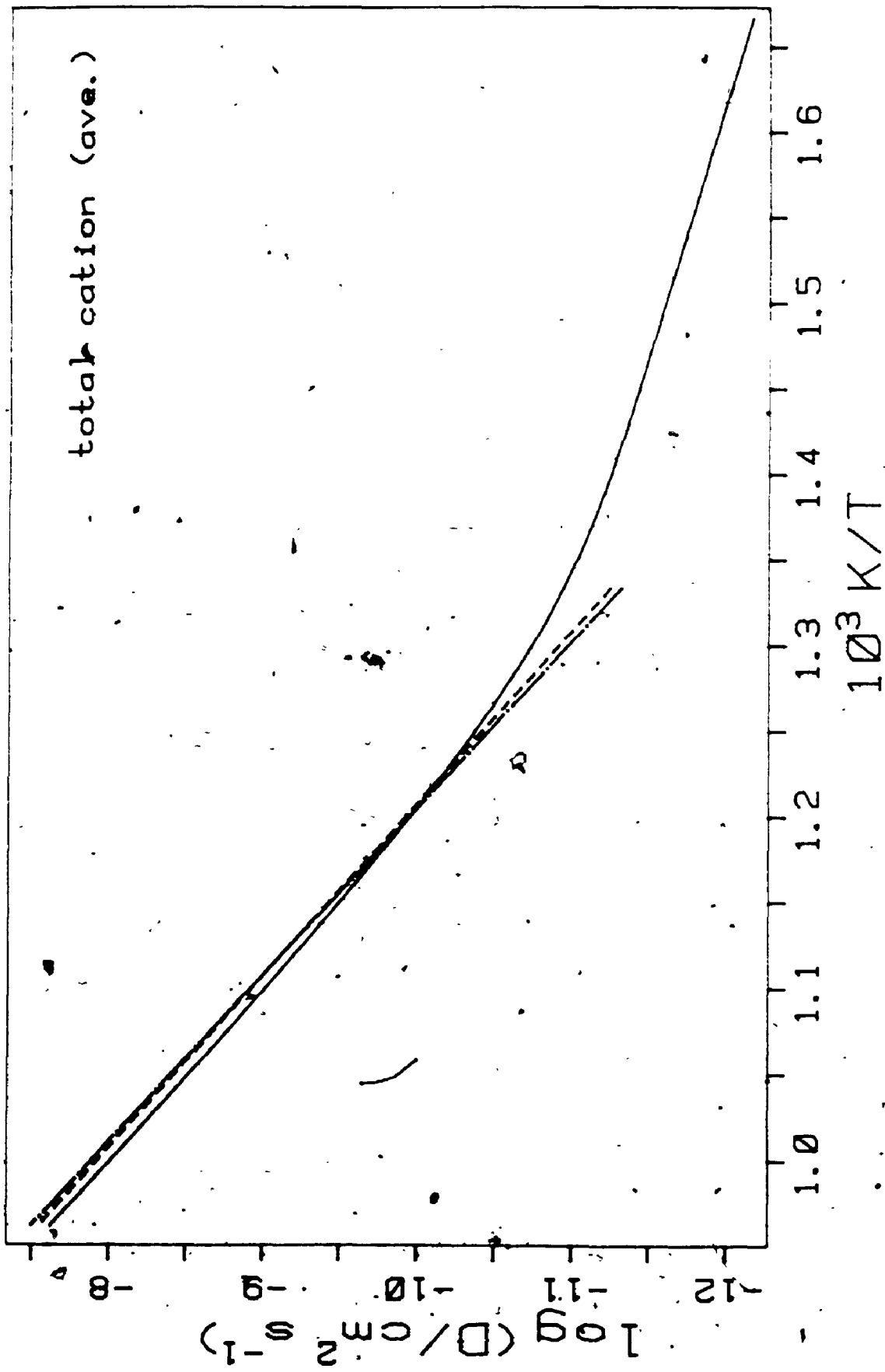


Figure 6-28: Cation diffusion via single vacancies in nominally pure NaCl calculated using the average parameter set. Bènière's²¹ data for pure NaCl are represented by the broken line and the diffusion coefficients calculated from the results of the present investigation are given by the solid line.

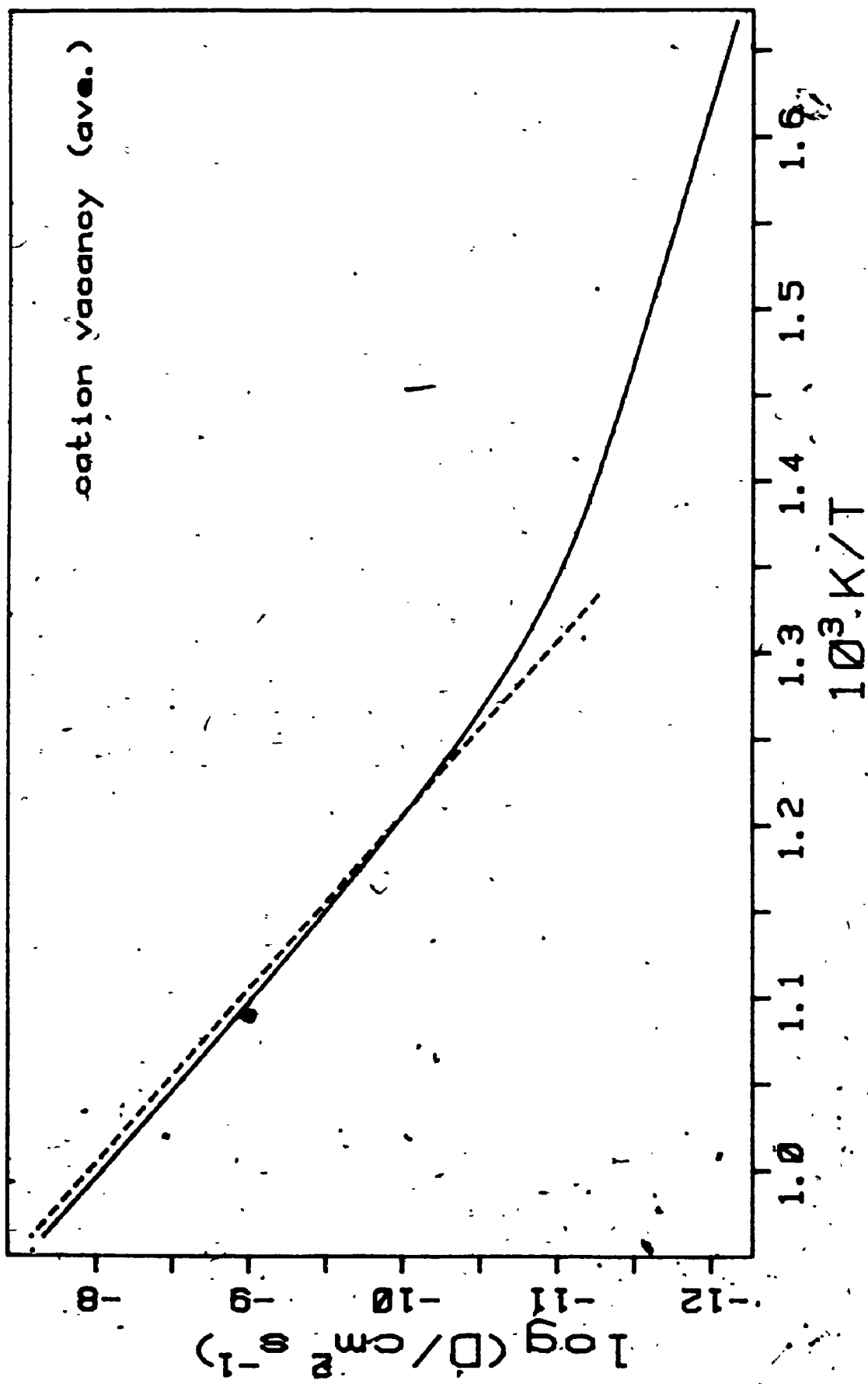
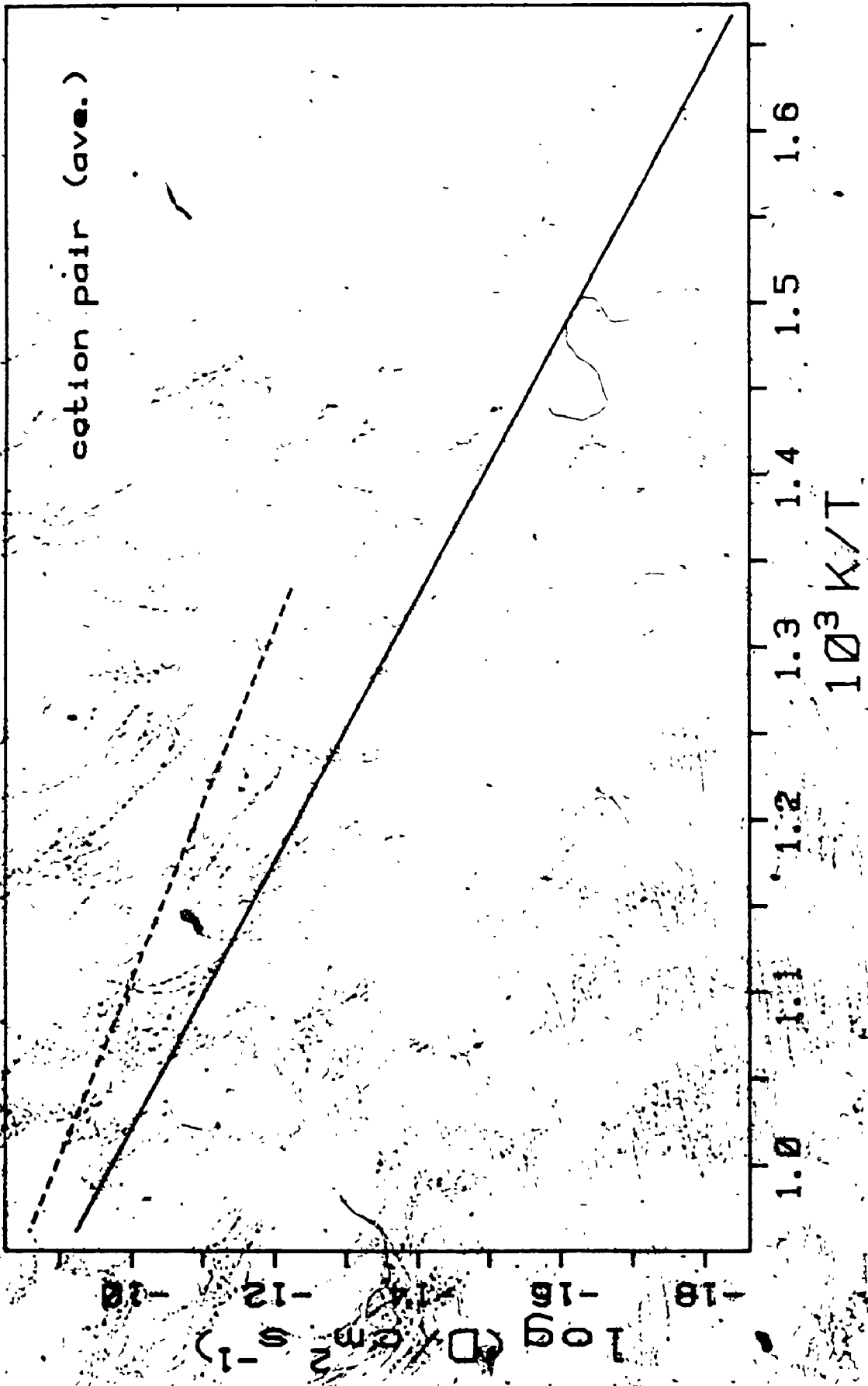


Figure 6-29: Cation diffusion via vacancy pairs in nominally pure NaCl calculated using the average parameter set. Bénéjère's²⁰ data are represented by the broken line and the diffusion coefficients calculated from the results of the present investigation are given by the solid line.



191

Figure 6-30: Total anion-diffusion in nominally pure NaCl calculated using the average parameter set. Bènière's²¹ data for pure NaCl are represented by the broken line and the diffusion coefficients calculated from the results of the present investigation are given by the solid line.

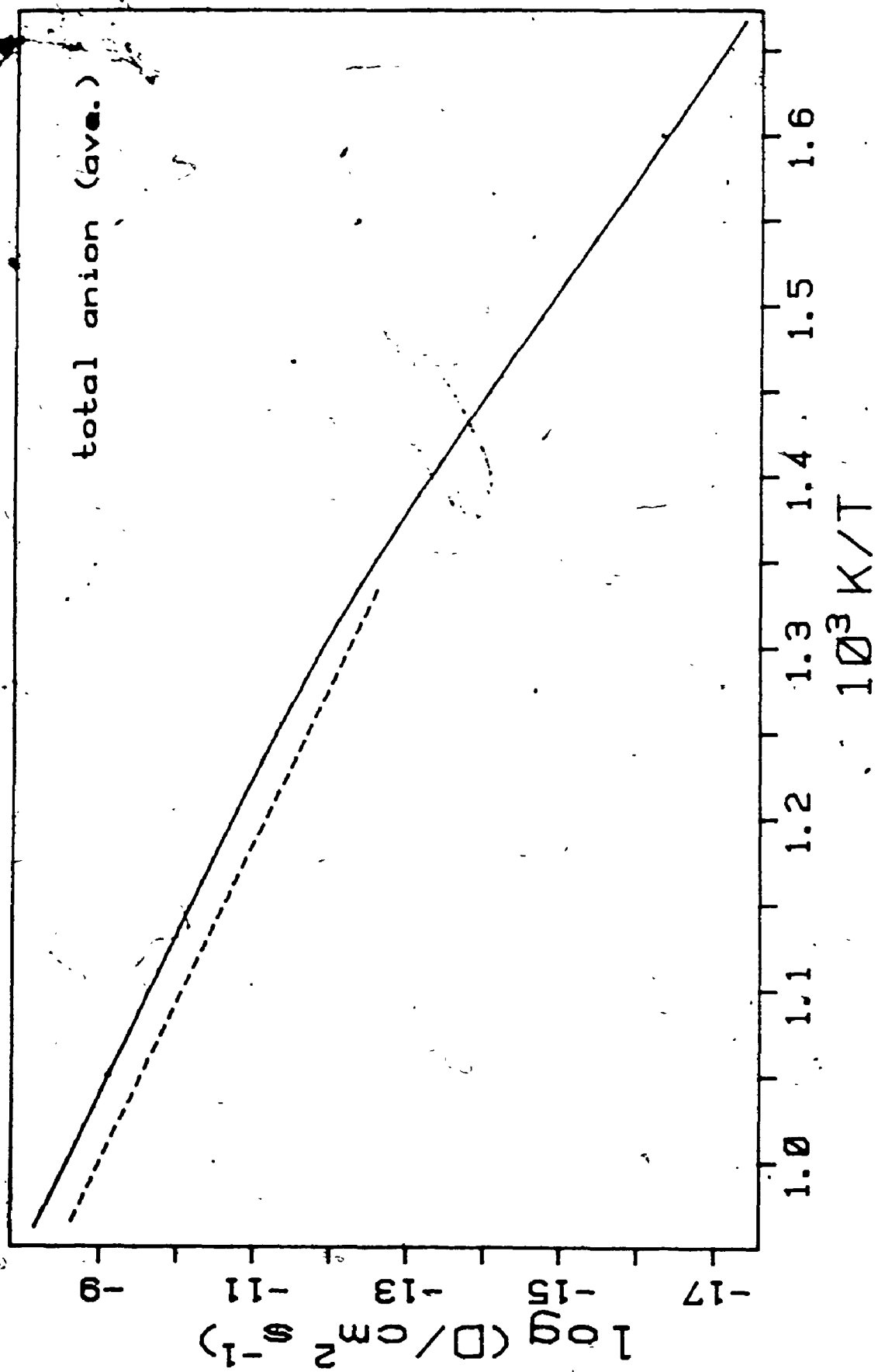


Figure 6-31: Anion diffusion via single vacancies in nominally pure NaCl calculated using the average parameter set. The broken line represents Bénére's²¹ data for pure NaCl and the solid line represents the diffusion coefficients calculated using the results from the present investigation.

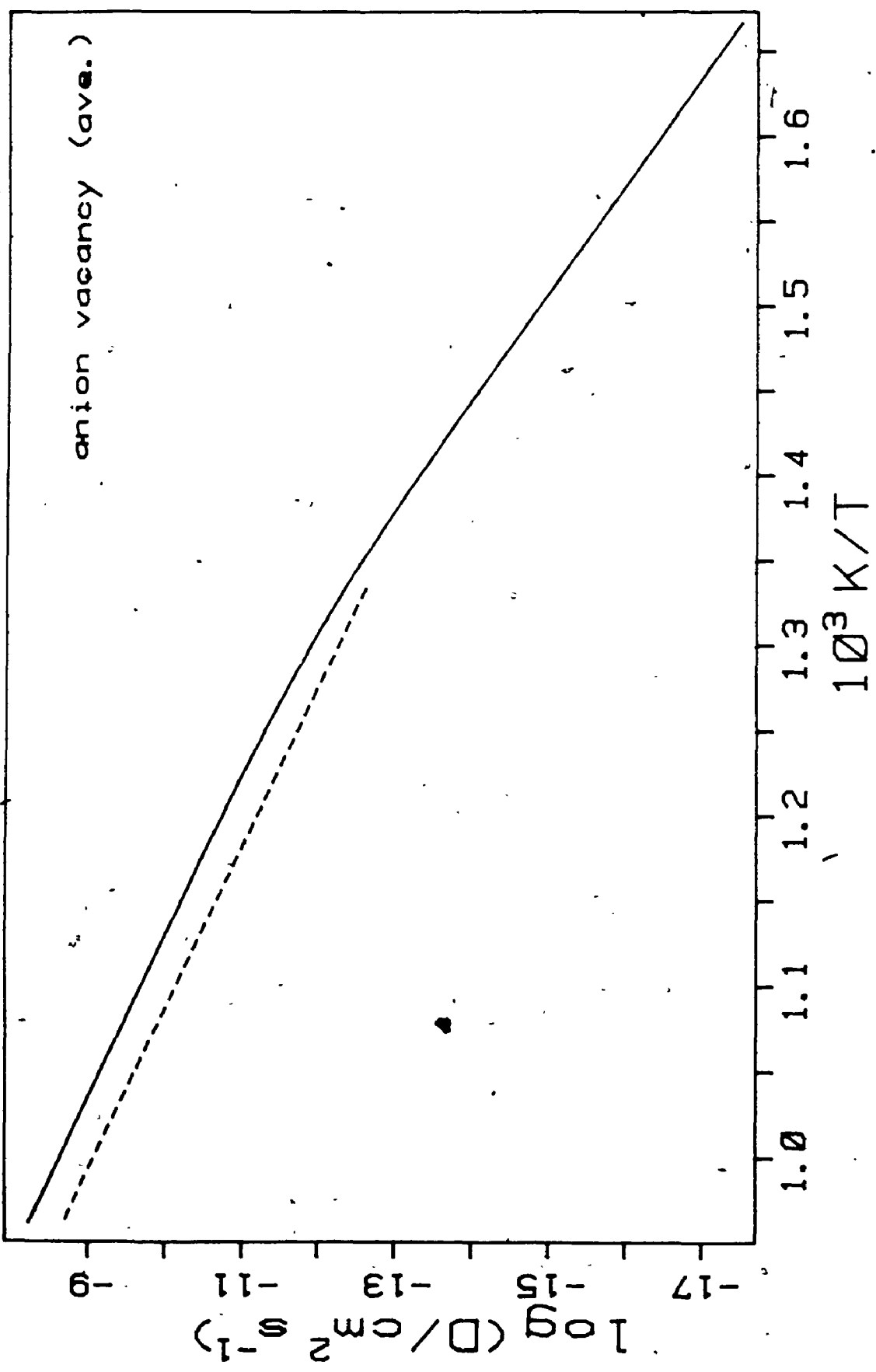
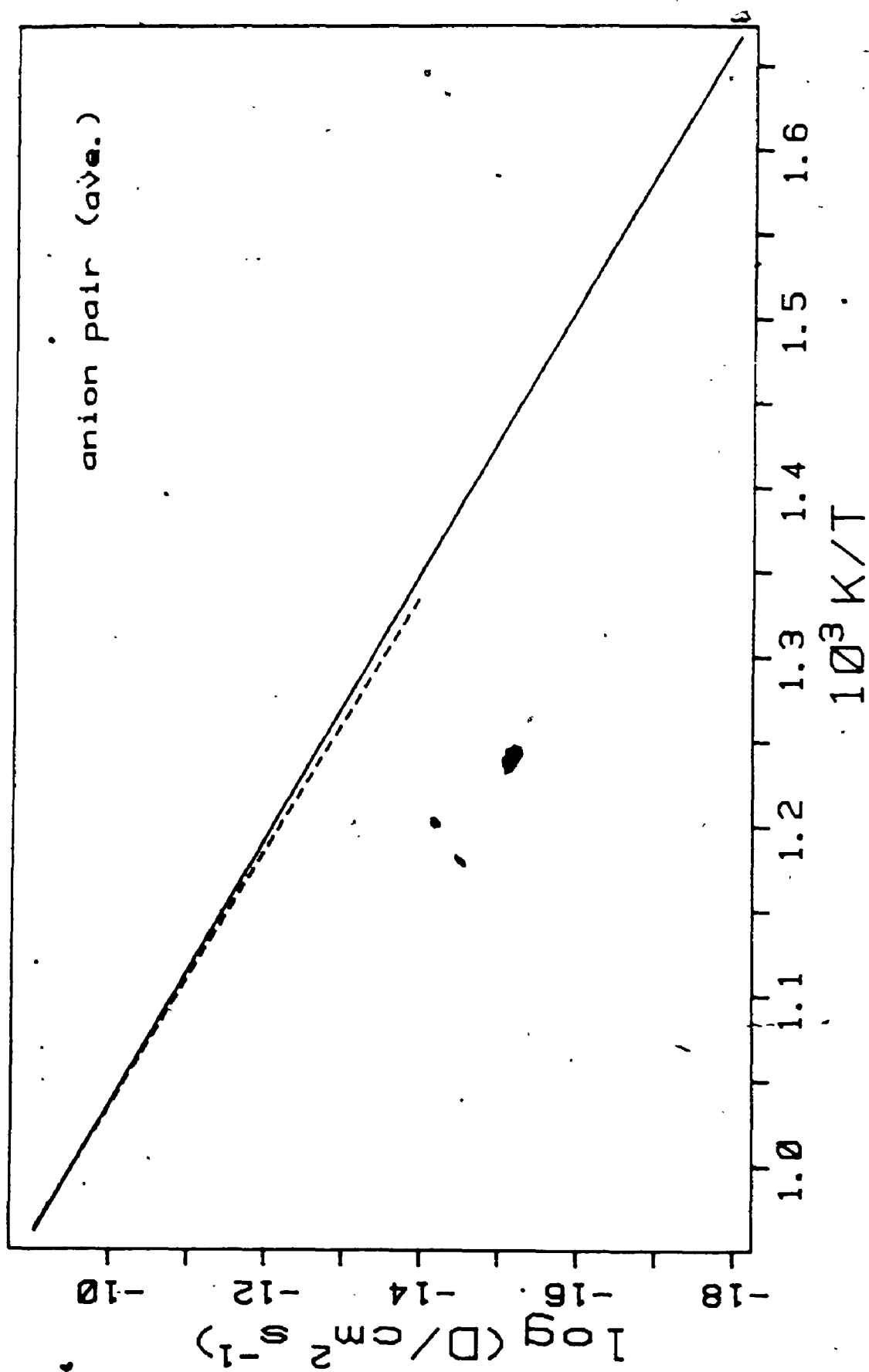


Figure 6-32: Anion diffusion via vacancy pairs in nominally pure NaCl calculated using the average parameter set. The broken line represents B ni re's²⁰ data and the solid line gives the diffusion coefficients calculated using the results from the present investigation.



Chapter Seven

Alkali Halide Quasi-harmonic Calculations

7.1. Introduction

The defect parameters determined in the conductivity analysis were assumed to be temperature independent however, it has been suggested that this might not be the true for KCl^{77, 1, 2} and therefore, by analogy, similar arguments would be expected to hold for NaCl. It has been demonstrated by means of HADES calculations that an increase of 1% in the lattice constant of KCl resulted in a decrease of 1.6% in the Schottky formation energy of KCl²². It should be kept in mind that the calculated defect energies are determined at constant volume whereas the experimental values are determined at constant pressure.

The effect of temperature dependent defect parameters is more pronounced in AgCl where the free energy of Frenkel pair formation decreases more rapidly than would be predicted using a temperature independent enthalpy and entropy. Through a combination of static lattice simulations and the fitting of ionic conductivity data, it has been discovered that while the enthalpy of defect formation, h^p , increases with increasing temperature, the energy at constant volume, u^v decreases^{85, 86, 43}. Thus at the melting point, h^p is approximately 50% higher than u^v . Catlow *et al*⁸⁵ found that by using the quasi-harmonic approximation,

$$u(V, T) = u(V(T)) \quad (1)$$

they were able to describe the temperature dependence of the defect formation energies of AgCl. As implied by Equation (1), defect energies were calculated by assuming that the temperature and volume changes could be introduced by including the temperature dependence of the lattice parameter.

The success with AgCl led Corish, Catlow, and Jacobs⁴ to carry out similar calculations on NaCl and KCl. They calculated the enthalpy of formation of Schottky

defects and the vacancy migration energies at constant volume over a wide temperature range. The CDN spline potentials, derived at 0 K by a combination of theoretical calculations and the simultaneous fitting of all the alkali halides to their 0 K properties, were used and the defect energies were calculated using the HADES program and the quasi-harmonic approximation. They found that the values of u^V decreased by 19 and 21% for KCl and NaCl respectively and h^P increased by 10 and 9% over the same temperature range.

Temperature dependent defect energies have in general been calculated at various temperatures by using potentials derived at 0 K and introducing the change in lattice parameter due to the thermal expansion of the crystal. The following investigation was undertaken in order to determine the temperature dependence of the potentials themselves by fitting the potentials to the physical properties of the crystal over a wide temperature range.

7.2. Comparison of Results Using Temperature Dependent and Temperature Independent Potentials

The crystal properties were calculated for NaCl, KCl, and KBr from 0 K to their melting points using both the temperature dependent (TD) potentials derived in Section 2.2 and the Catlow, Diller, and Norgett (CDN)⁵ potentials derived at 0 K. The unsplined potential was used for NaCl and the splined potentials were used for KCl and KBr.

Since the results are similar for each of the alkali halides investigated only the results for NaCl have been included. The most dramatic difference in the two potentials is the calculated bulk strains. The bulk strain for the TD potential was less than 1 part in 10^4 over the entire temperature range since this requirement was incorporated into the fitting procedure. The CDN potentials produced bulk strains which reached 7% at the highest temperatures (Figure 7-1) which is not surprising since the potential was derived at 0 K. The elastic properties have also been plotted in Figures 7-2 and 7-3. The values

determined using the TD potential agree with the experimental data; however, the CDN values are slightly lower in the case of the bulk modulus and higher in the case of c_{44} . The values for c_{44} calculated using the CDN potential show very little temperature dependence. The values for the static dielectric constant are much higher than the experimental at high temperatures when a temperature independent potential is used (Figure 7-4). Only two experimental values were available for the high frequency dielectric constant and therefore considerable scatter resulted for the values calculated using the temperature dependent potentials (Figure 7-5). The CDN potential produced smoothly varying values however they are much lower at high temperatures than would be expected from a linear extrapolation of the two available experimental points. The same situation arises for the transverse optic mode; however, in this case the values produced by the TD potentials are also smoothly varying and lie below the two experimental points. The CDN potential produced values lower than the TD potentials (Figure 7-6).

The Schottky formation and cation and anion migration energies have been calculated for each of the alkali halides using both sets of potentials. Once again only the NaCl results are given (Figures 7-7 to 7-9). The TD potentials in general produce energies lower than those calculated using the temperature independent potential. The only instance for which this is not invariably true is in the case of the vacancy migration energies for NaCl. The defect energies are also closer in value for NaCl than for KCl or KBr. The results indicate that the effect of using a 0 K potential to calculate defect energies over a wide temperature range, and thereby introducing lattice strain, is not as great as might perhaps have been expected. The difference in migration energies and Schottky formation energy resulting from the two sets of potentials for KCl and KBr is somewhat larger, approximately 0.3-0.4 eV and 0.6 eV respectively.

7.3. Calculation of Thermodynamic Properties

The thermodynamic properties have been calculated according to the equations set out by Catlow *et al.*⁴³. It was necessary to begin by equating the Gibbs energy and Helmholtz energy,

$$g^P = f^V \quad (2)$$

a relation which follows from the quasi-harmonic approximation. The values for g^P were calculated from the individual values of h^P and s^P determined by experiment for the Schottky formation and the cation and anion migration energies (NaCl, B  ni  re *et al.*²¹; KCl, Acu  a and Jacobs²; KBr, Dawson⁸¹)

The unit cell volume $v(T)$ was then calculated from the lattice parameter $a(T)$, $v=2a^3$, and hence the expansivity determined from,

$$\beta^V(T) = (1/v) (\partial v / \partial T)_P \quad (3)$$

From f^V and $v(T)$, df^V/dv , and then the following thermodynamic properties were calculated,

$$v^P = K_T v (\partial f^V / \partial v)_T \quad (4)$$

$$h^P = u^V + v^P (T \beta^P / K_T) \quad (5)$$

$$s^P = s^V + v^P (\beta^P / K_T) \quad (6)$$

Here K_T is the isothermal compressibility⁸⁷ and s^V was calculated from $(u^V - f^V)/T$. While this is not a completely theoretical method of calculating s^V it was the only way available since defect entropy calculations are not yet routine and are very elaborate⁸⁸. In this way the volume, enthalpy, and entropy at constant pressure can be calculated. Note that the calculation of v^P is independent of u^V .

The quasi-harmonic results were plotted in Figures 7-10 to 7-15 for NaCl and Figures 7-16 to 7-21 for KBr. The results for KCl have been published elsewhere⁴⁹. These calculations were carried out for the Schottky formation and cation and anion migration energies. Values for the Gibbs energy, the enthalpy, the energy, the entropies at constant volume and constant pressure, and the volume of formation were plotted.

The Schottky defect formation energy and Gibbs energy for NaCl showed a decrease of 18 and 25% respectively with increasing temperature. The enthalpy increased gradually with temperature by 6%. Both the entropy at constant volume and the entropy at constant pressure increased asymptotically with temperature. The volume of formation decreased with increasing temperature but levelled off at a fairly low temperature. The energy, Gibbs energy, and enthalpy for the cation and anion vacancy migration all decreased with increasing temperature. This effect was most pronounced for the energy, 23 and 28% for the cation and anion respectively, however, the decrease of 6 and 14% for the cation and anion migration enthalpies should be noted. The entropy at constant pressure, the entropy at constant volume, and the volume of formation for the cation vacancy migration exhibited the same trends as the corresponding properties for Schottky defect formation. The anion vacancy migration behaved differently in that the volume of formation increased asymptotically with temperature. The values for the entropy at constant volume for the cation vacancy migration and the entropy at constant pressure for the anion vacancy migration were negative.

The energy at constant volume and the Gibbs energy for the Schottky defect formation for KBr decreased (21 and 17% respectively) with increasing temperature and the enthalpy increased by 3%. There was some scatter in the entropies however they did increase slightly with temperature while the volume of formation decreased slightly. The energy and Gibbs energy for the cation vacancy migration decreased with increasing temperature by 27 and 20% respectively and the enthalpy increased very slightly (2%). The entropies increased asymptotically with temperature and the volume of formation decreased gradually. The values for the entropy at constant volume were negative. The energy and Gibbs energy for the anion vacancy migration decreased with increasing temperature and the enthalpy increased slightly. The entropies again increased and were negative except in the case of the entropy at constant pressure at high temperatures. The volume of formation was almost temperature independent.

The energy and Gibbs energy for Schottky formation for KCl decreased with increasing temperature by 18 and 17% respectively but the enthalpy remained constant. The entropy at constant volume decreased with increasing temperature however the entropy at constant pressure and the volume of formation exhibited no temperature dependence. The energy and Gibbs energy for the cation vacancy migration decreased with increasing temperature (21 and 20%) and the enthalpy increased slightly. Both entropies increased asymptotically with temperature and the volume of formation decreased and then increased again. The energy and Gibbs energy for anion vacancy migration again increased with decreasing temperature as expected (24 and 29%); however, the enthalpy was independent of temperature. The entropy at constant volume, entropy at constant pressure, and the volume of formation decreased slightly with increasing temperature. The values for the entropy at constant volume for the cation vacancy migration were again negative.

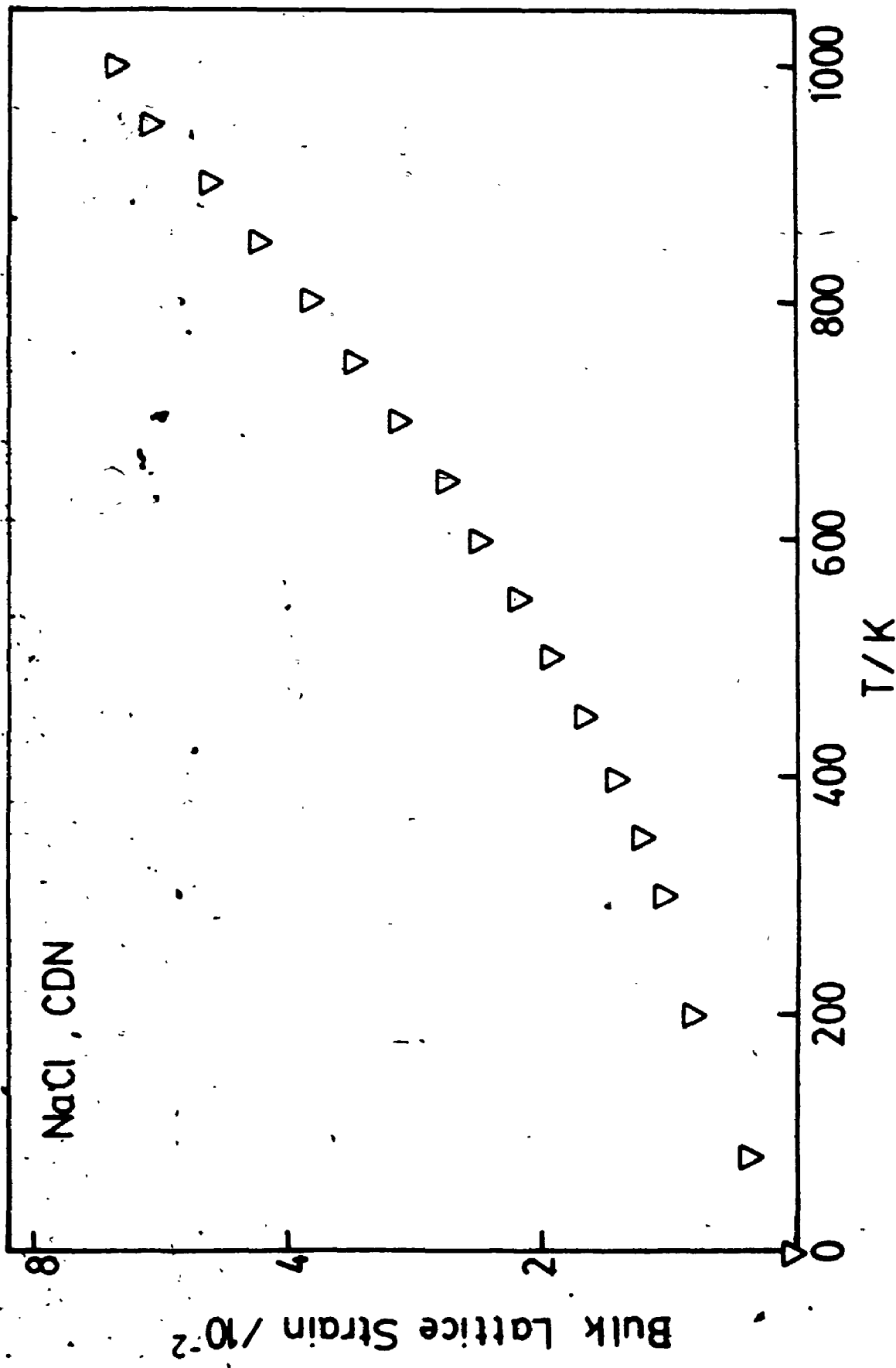
In general, the enthalpy changed less with increasing temperature than the energy at constant volume. It is also interesting to note that as in the case of the silver halides and the alkali halide calculations of Catlow *et al.*⁴, the Schottky formation energy decreased while the enthalpy increased for NaCl and KBr but was temperature independent for KCl. This is also true for the migration energies and enthalpies of KBr but the enthalpies decreased with increasing temperature for the vacancy migration in NaCl and were either temperature independent or increased slightly with temperature for KCl.

The Schottky defect formation enthalpy and entropy at constant pressure are in fairly good agreement with the experimentally determined values for NaCl. The experimental values are shown in the figures as horizontal lines through the temperature range over which they were determined. The enthalpy of cation vacancy migration also agrees with the experimentally determined value however the entropy is low. The comparison of the experimental and calculated values for the anion migration parameters is the least satisfactory but not entirely unacceptable.

7.4. Temperature Dependence of Conductivity Parameters

It is possible that the modification of the conductivity analysis to include temperature dependent parameters would improve the fit to the conductivity data. It is expected though that unlike the silver halides this correction would be small⁴. This procedure is not feasible however until a better understanding of the temperature dependence of the defect parameters is achieved.

Figure 7-1: Bulk strain in NaCl as a result of increasing temperature calculated using the CDN potential.



208

Figure 7-2: Experimental⁴⁵ values of the bulk modulus for NaCl and values calculated using the TD and CDN potentials

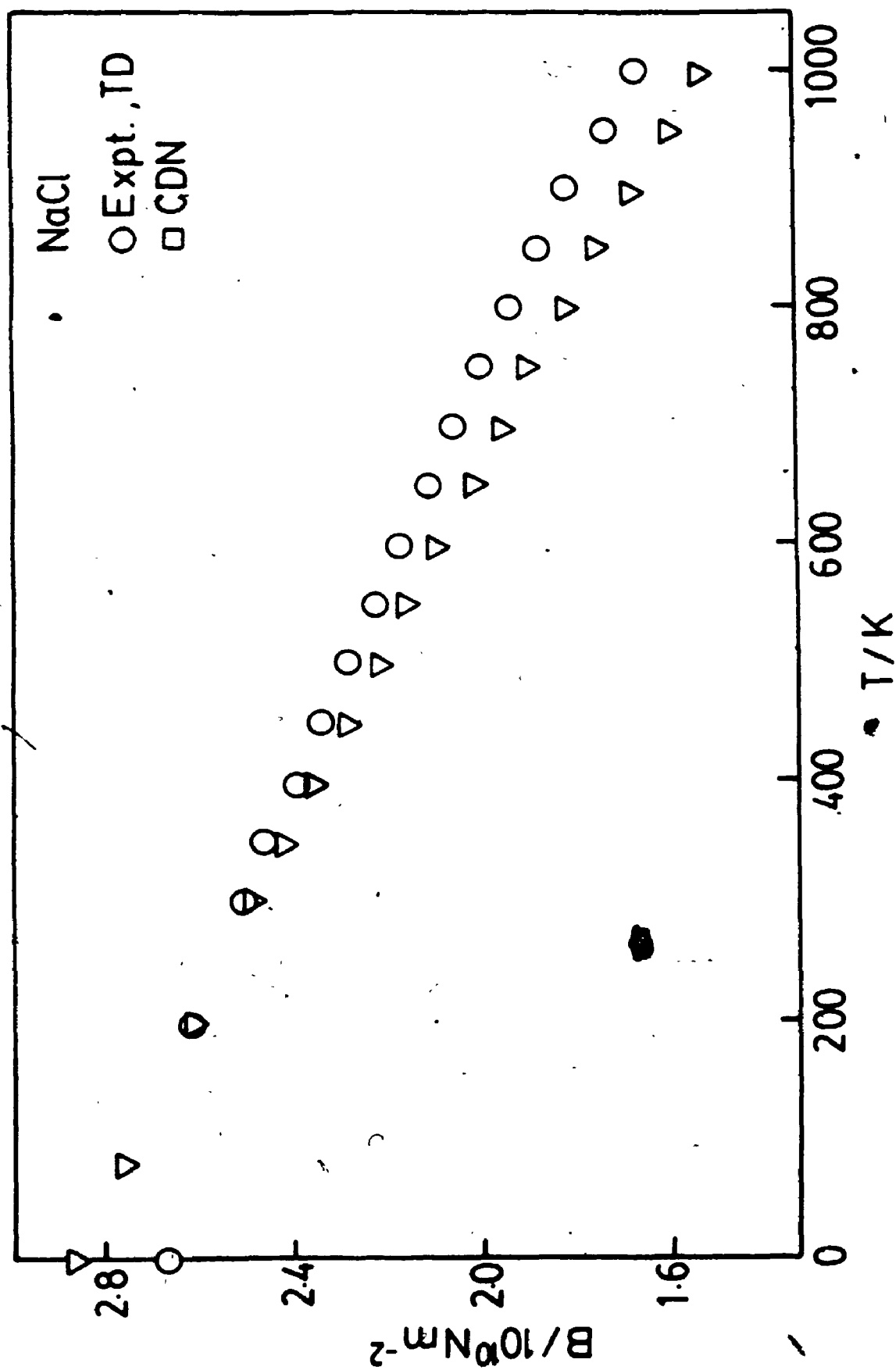


Figure 7-3: Experimental⁴⁵ values of the elastic constant c_{44} for NaCl and values calculated using the TB and CDN potentials

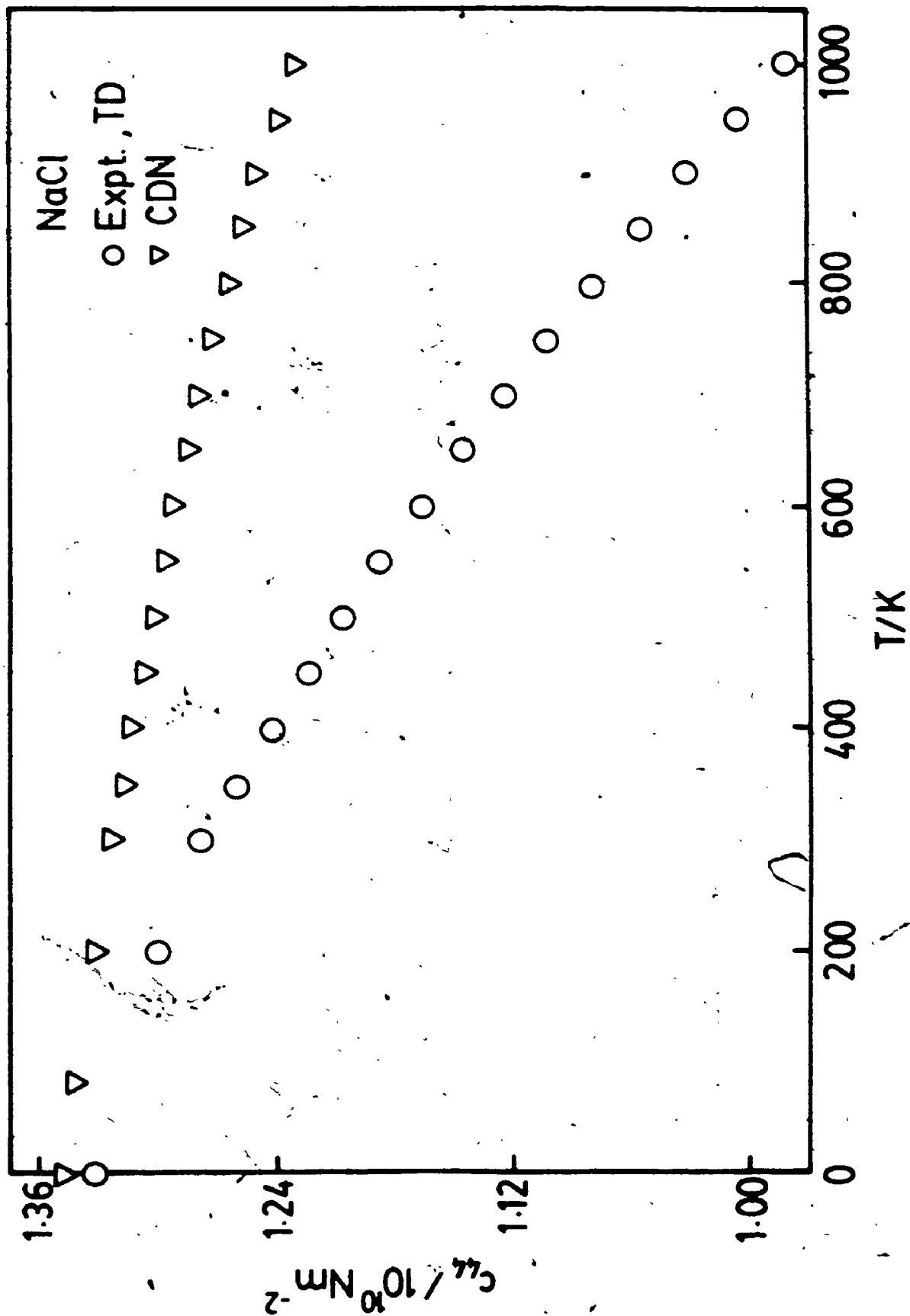


Figure 7-4: Experimental⁴⁶ values of the static dielectric constant for NaCl and values calculated using the TD and CDN potentials

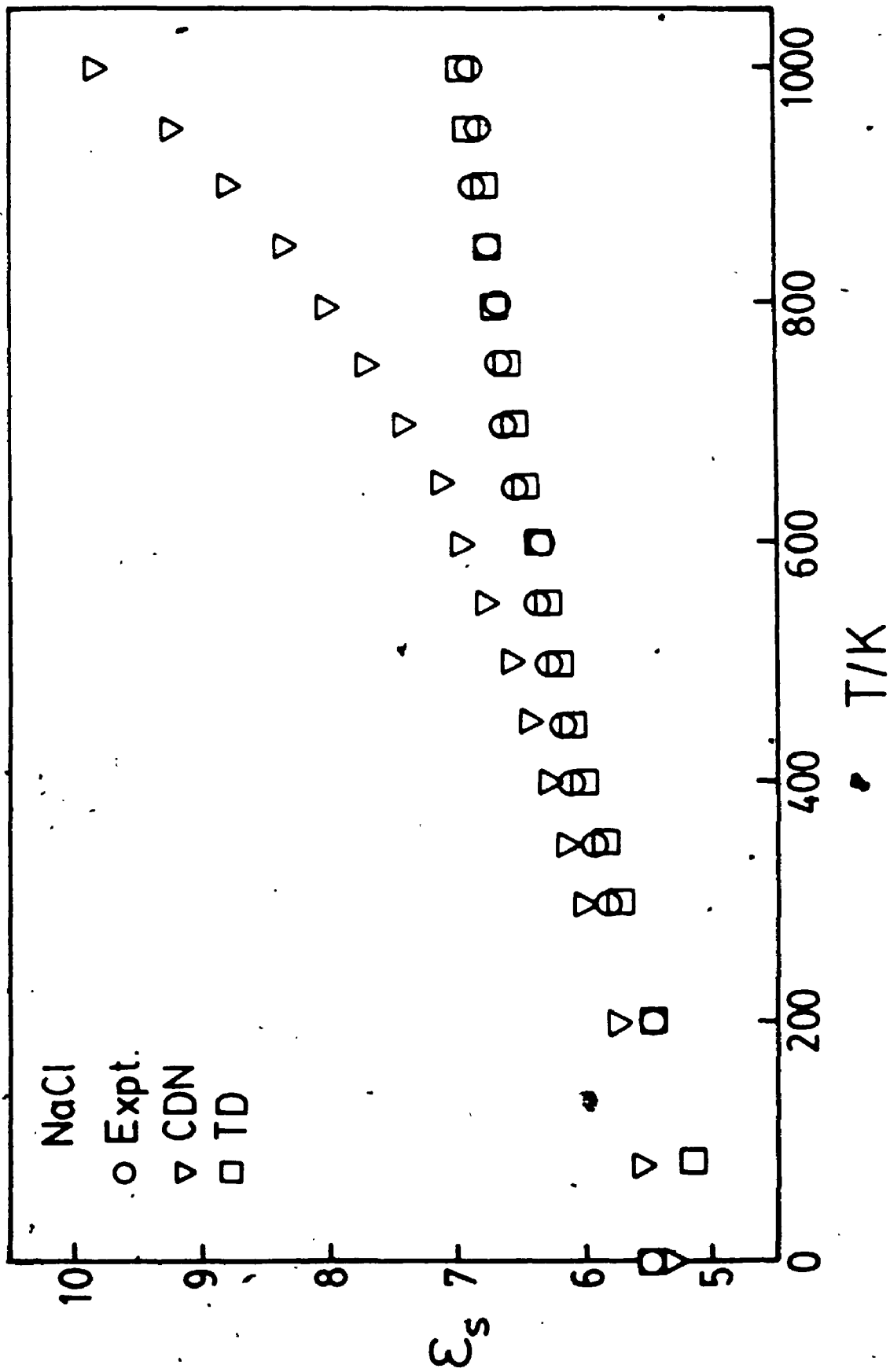


Figure 7-5: Experimental ϵ'' values for the high frequency dielectric constant for NaCl and values calculated using the TD and CDN potentials

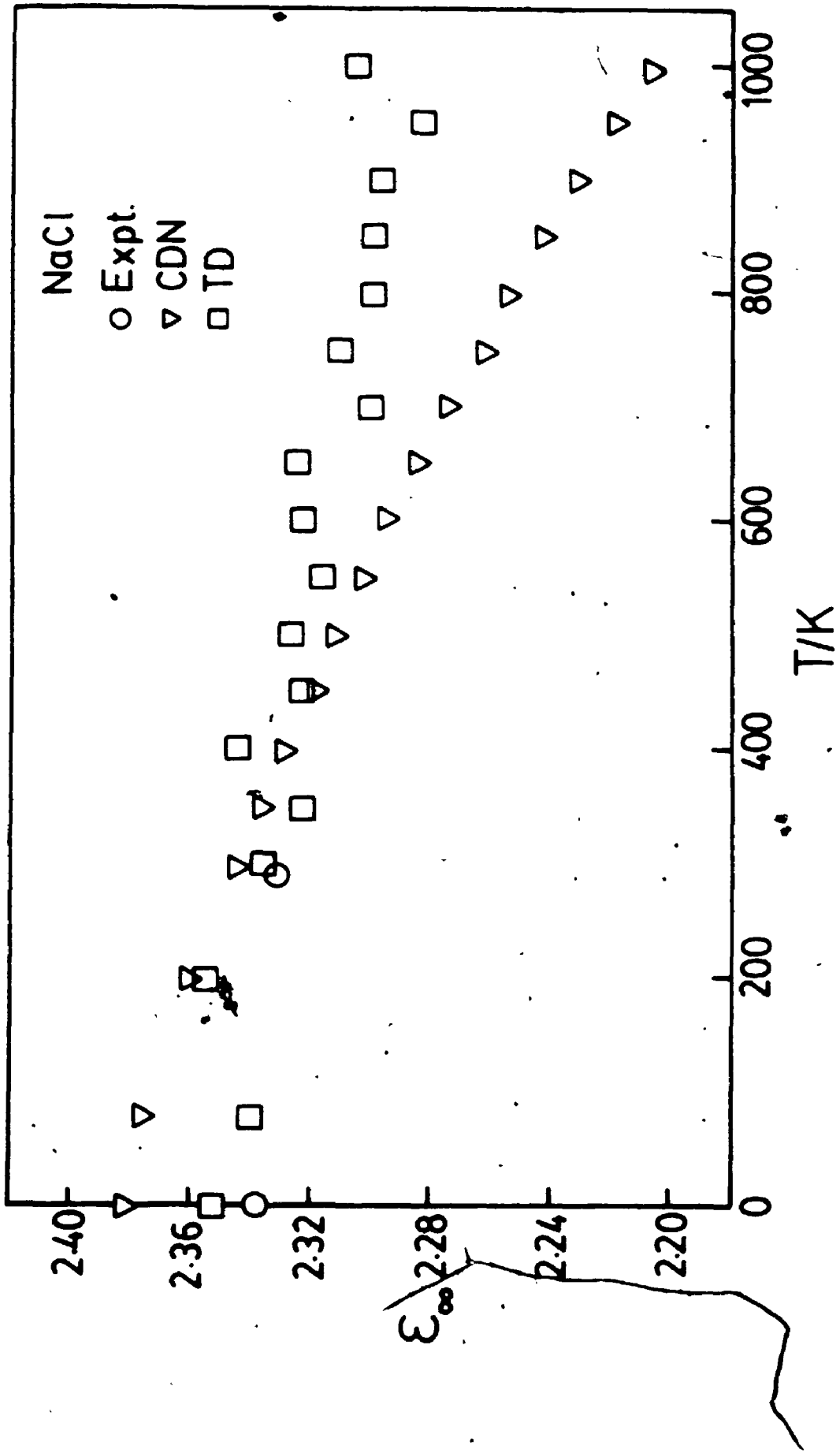


Figure 7-6: Experimental⁴⁷ values for the transverse optic mode for NaCl and values calculated using the TD and CDN potentials

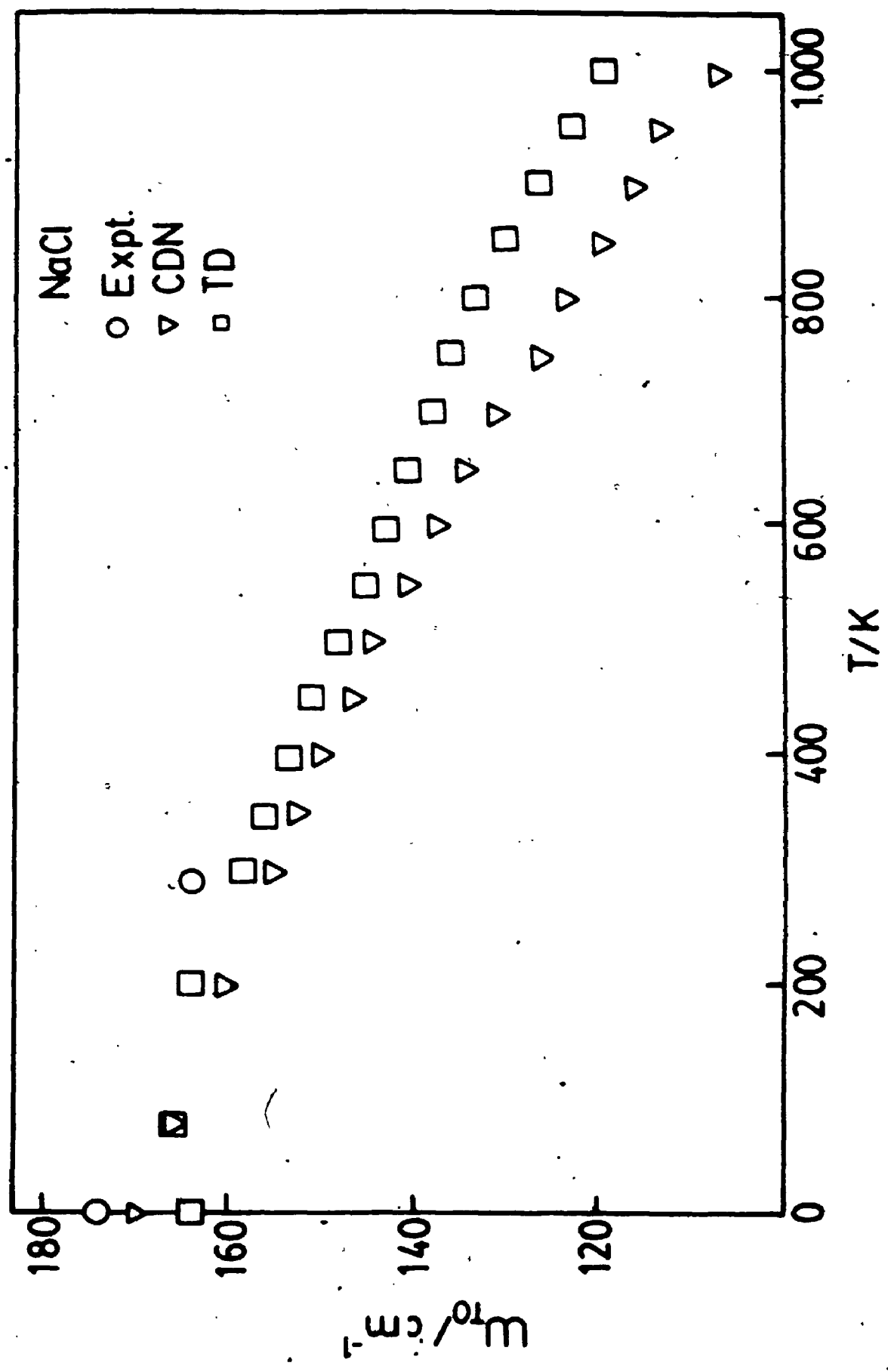


Figure 7-7: Values of u_s for NaCl calculated using the TD and CDN potentials

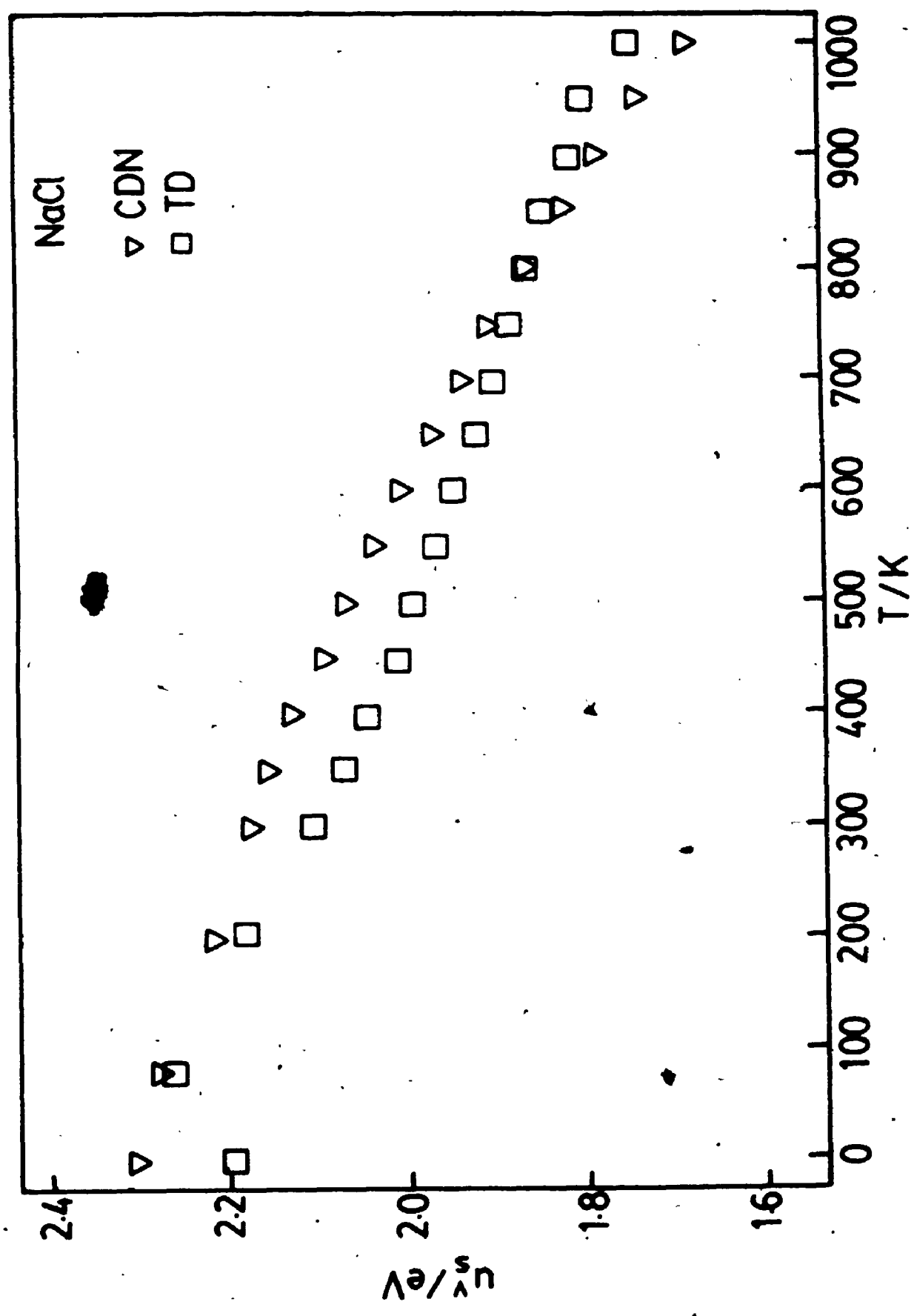


Figure 7-8: Values of Δu_{cv} for NaCl calculated using the TD and CDN potentials

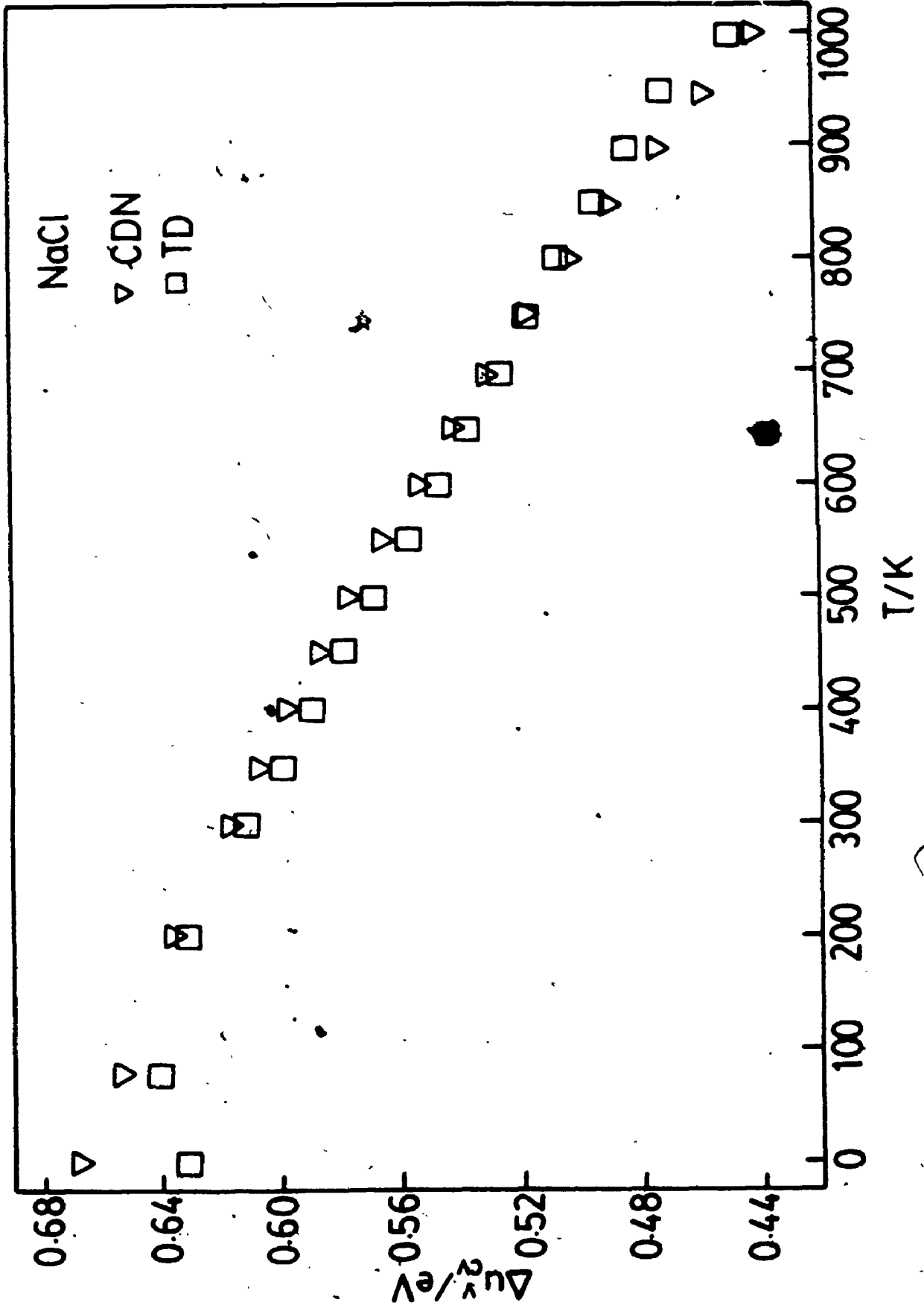


Figure 7-9: Values of Δu_{jv} for NaCl calculated using the TD and CDN potentials

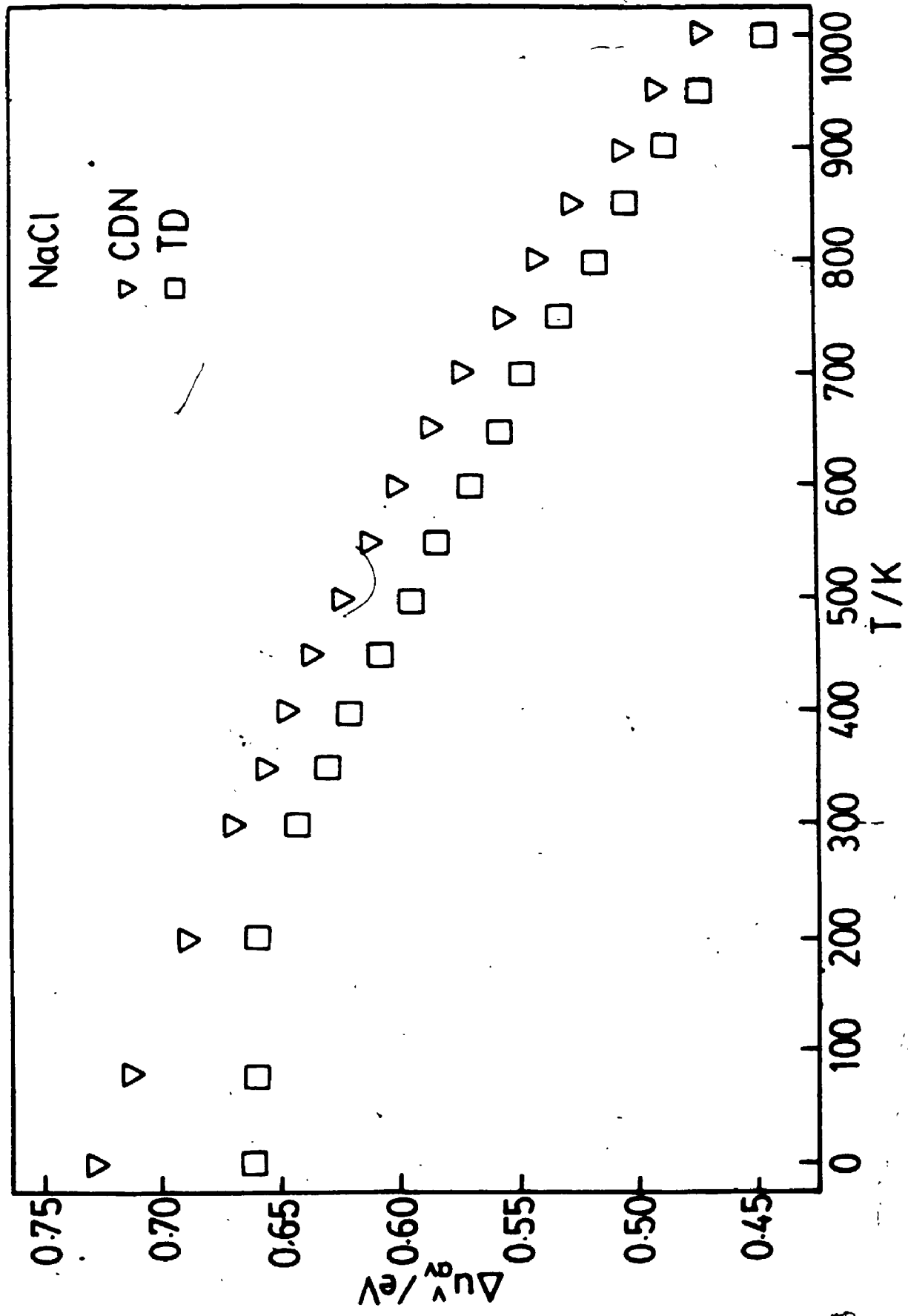


Figure 7-10: Values of g_S^0 , h_S^0 , and u_S^0 for NaCl calculated using the TD potentials
The solid line represents the value of h_S^0 determined experimentally over the indicated temperature range

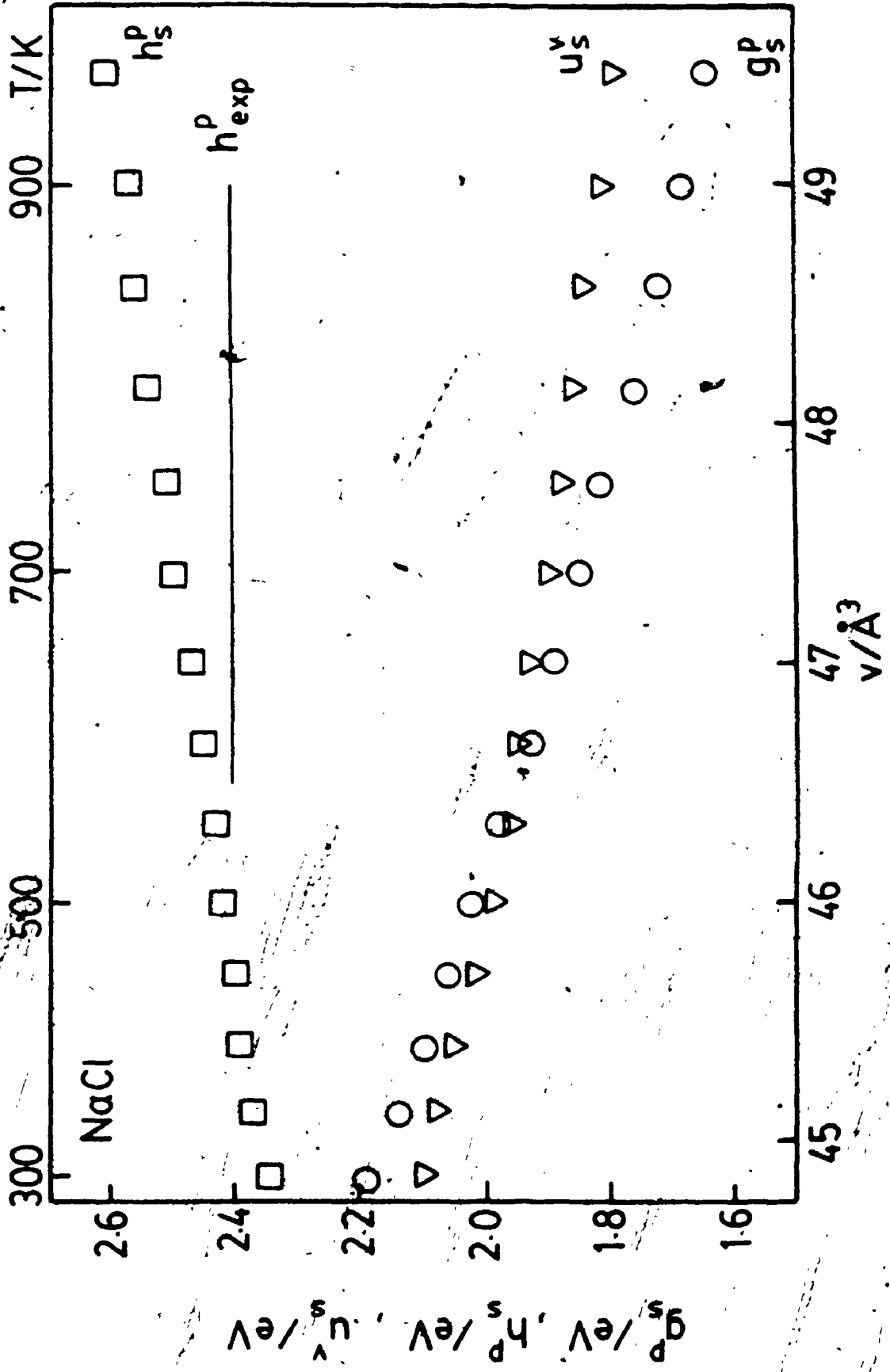
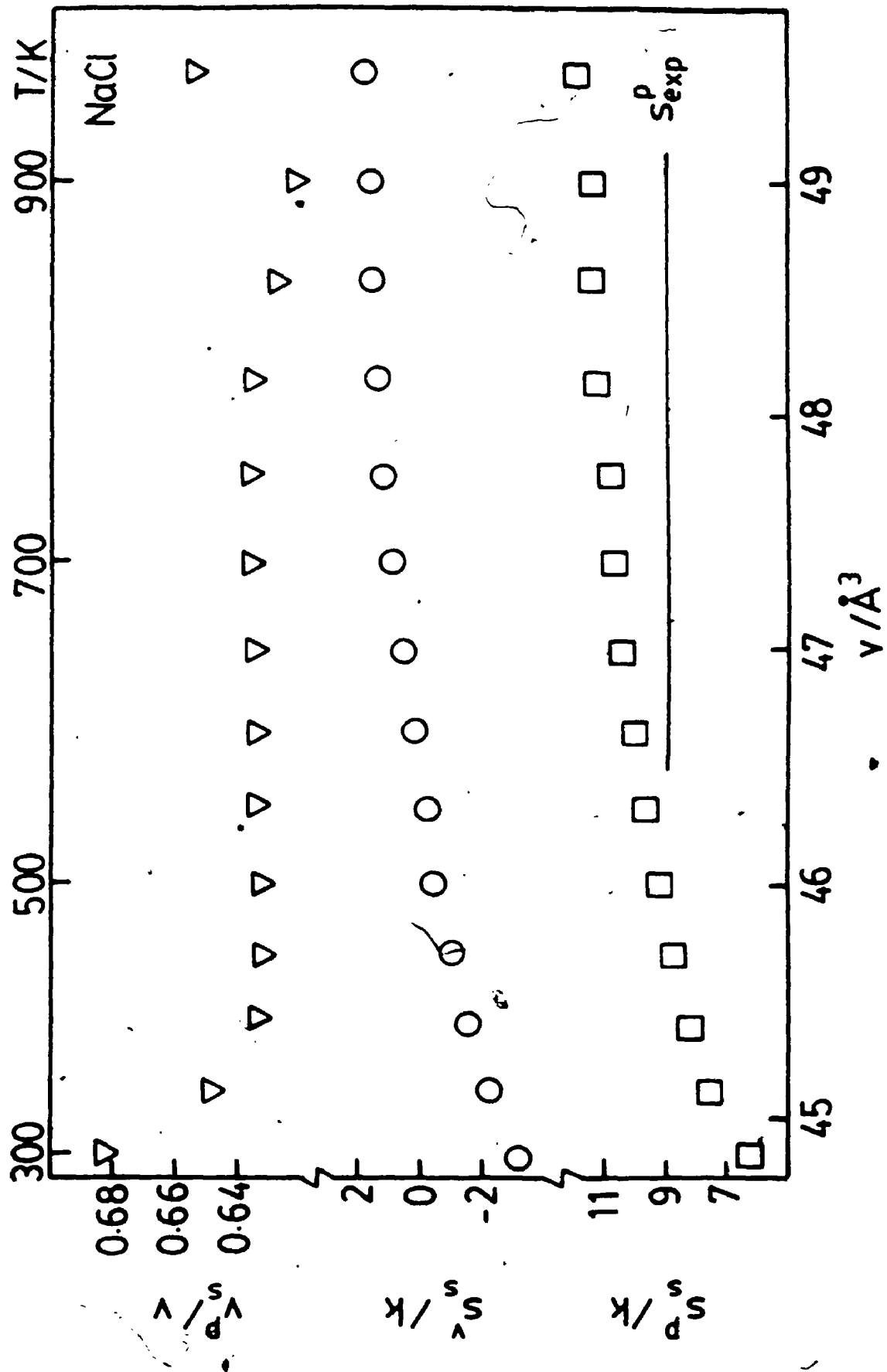


Figure 7-11: Values of s_p , s_s , and v_p/v for NaCl calculated using the TD potentials
The solid line represents the value of s_s determined experimentally over the indicated temperature range



*

Figure 7-12: Values of $\Delta g_{\text{Cu}}^{\text{P}}$, $\Delta h_{\text{Cu}}^{\text{P}}$, and $\Delta u_{\text{Cu}}^{\text{P}}$ for NaCl calculated using the TD potentials. The solid line represents the value of $\Delta h_{\text{Cu}}^{\text{P}}$ determined experimentally over the indicated temperature range.

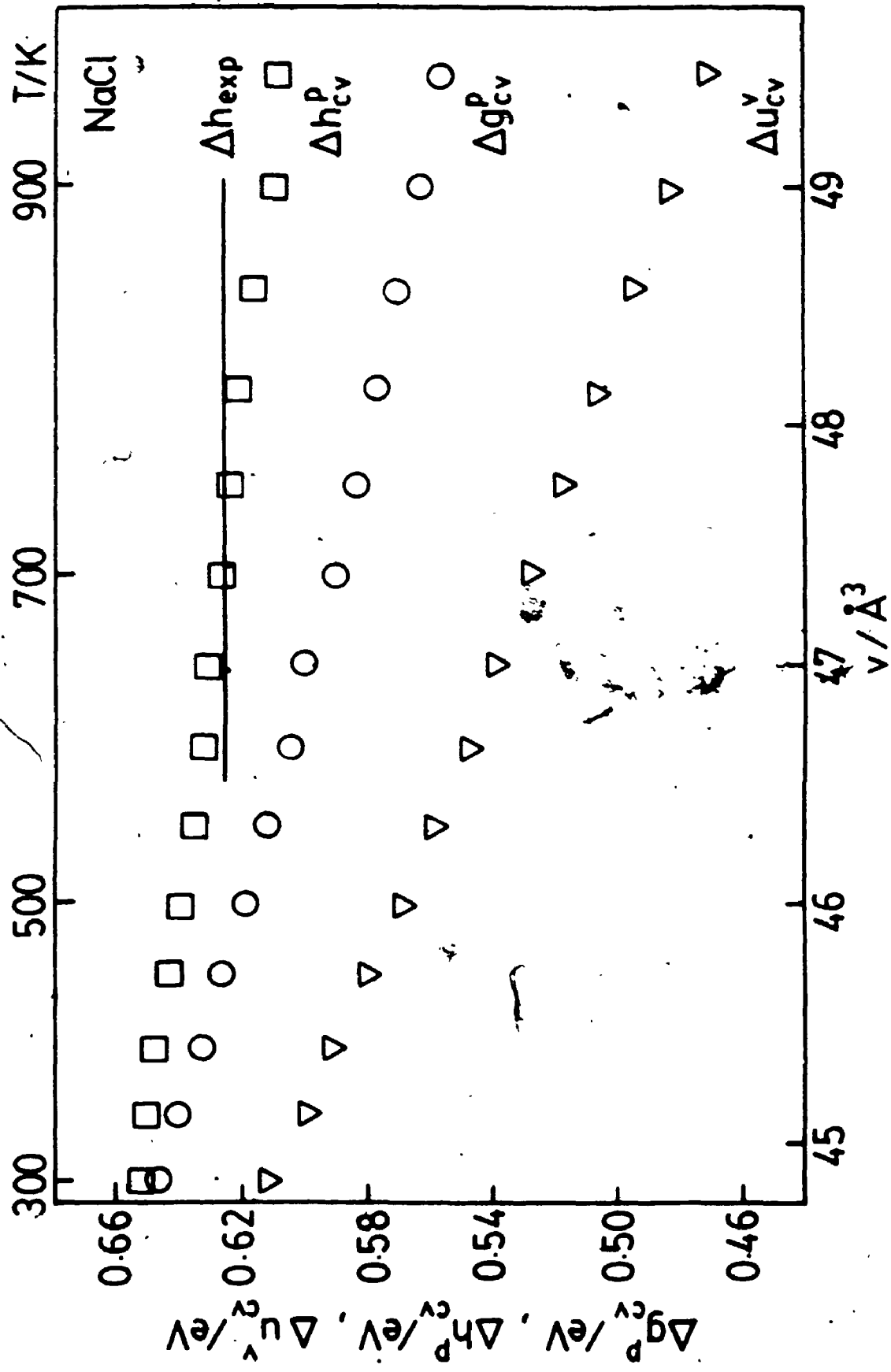


Figure 7-13: Values of Δs_{cv}^p , Δs_{cv}^v , and $\Delta v_{cv}^v/v$ for NaCl calculated using the TD potentials. The solid line represents the value of Δs_{cv}^v determined experimentally over the indicated temperature range.

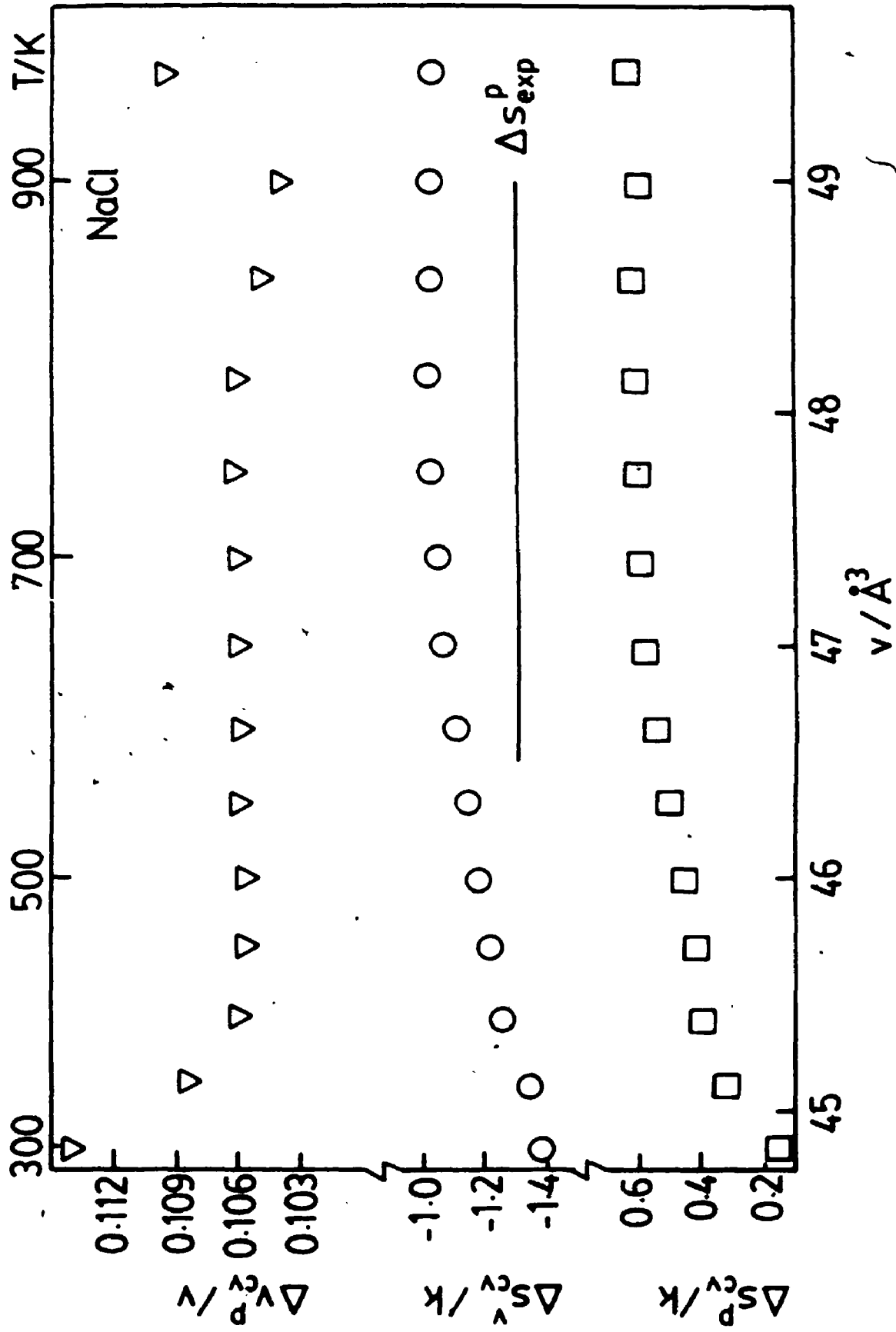


Figure 7-14: Values of Δg_{av}^p , Δh_{av}^p , and Δu_{av}^v for NaCl calculated using the TD potentials. The solid line represents the value of Δh_{av}^p determined experimentally over the indicated temperature range.

1.3

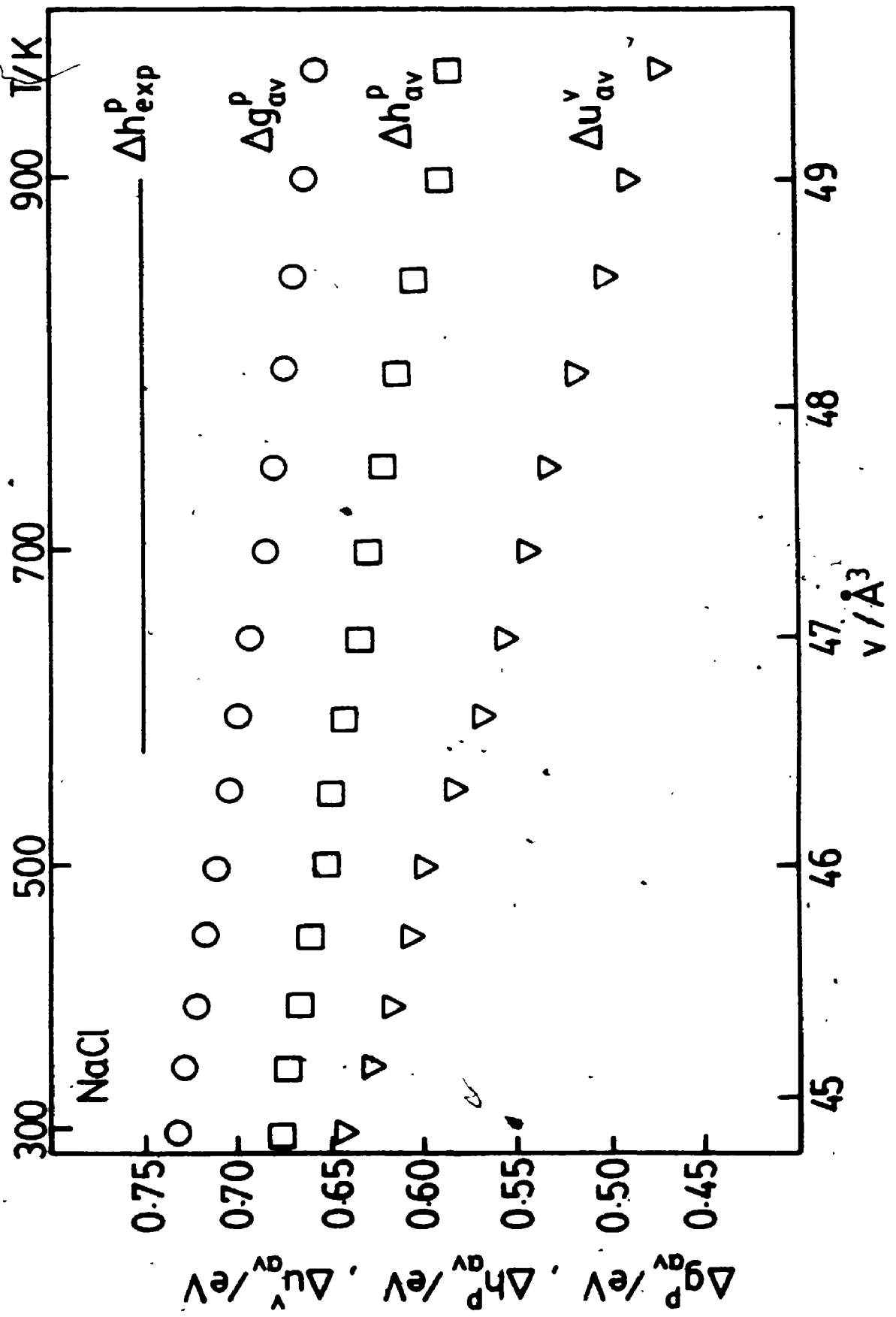


Figure 7-15: Values of Δs_{iv}^p , Δs_{iv}^v , and $\Delta v_{iv}^p/v$ for NaCl calculated using the TD potentials. The solid line represents the value of Δs_{iv} determined experimentally over the indicated temperature range.

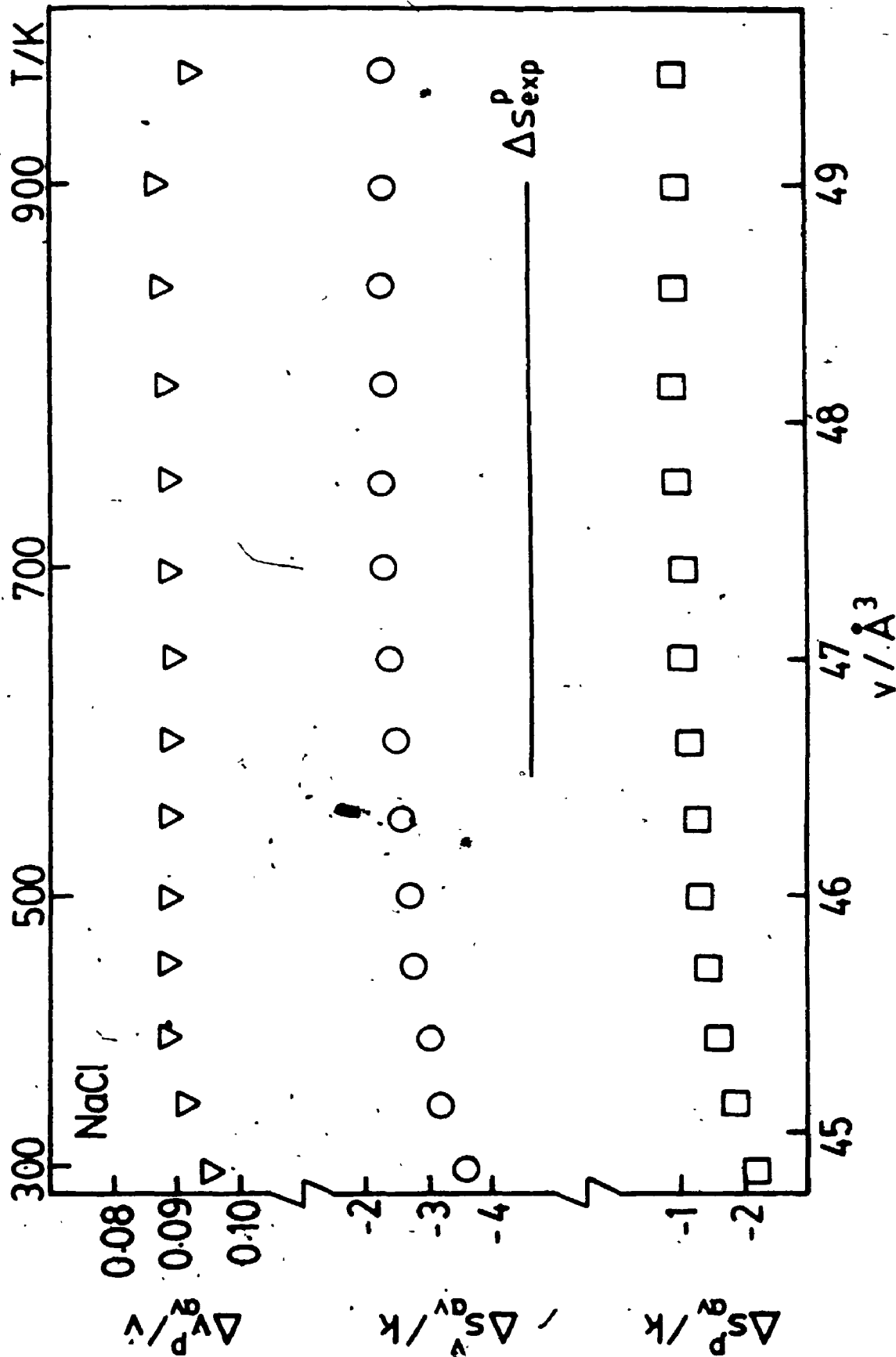


Figure 7-16: Values of g_{ξ}^0 , h_{ξ}^0 , and u_{ξ}^0 for KBr calculated using the TD potentials

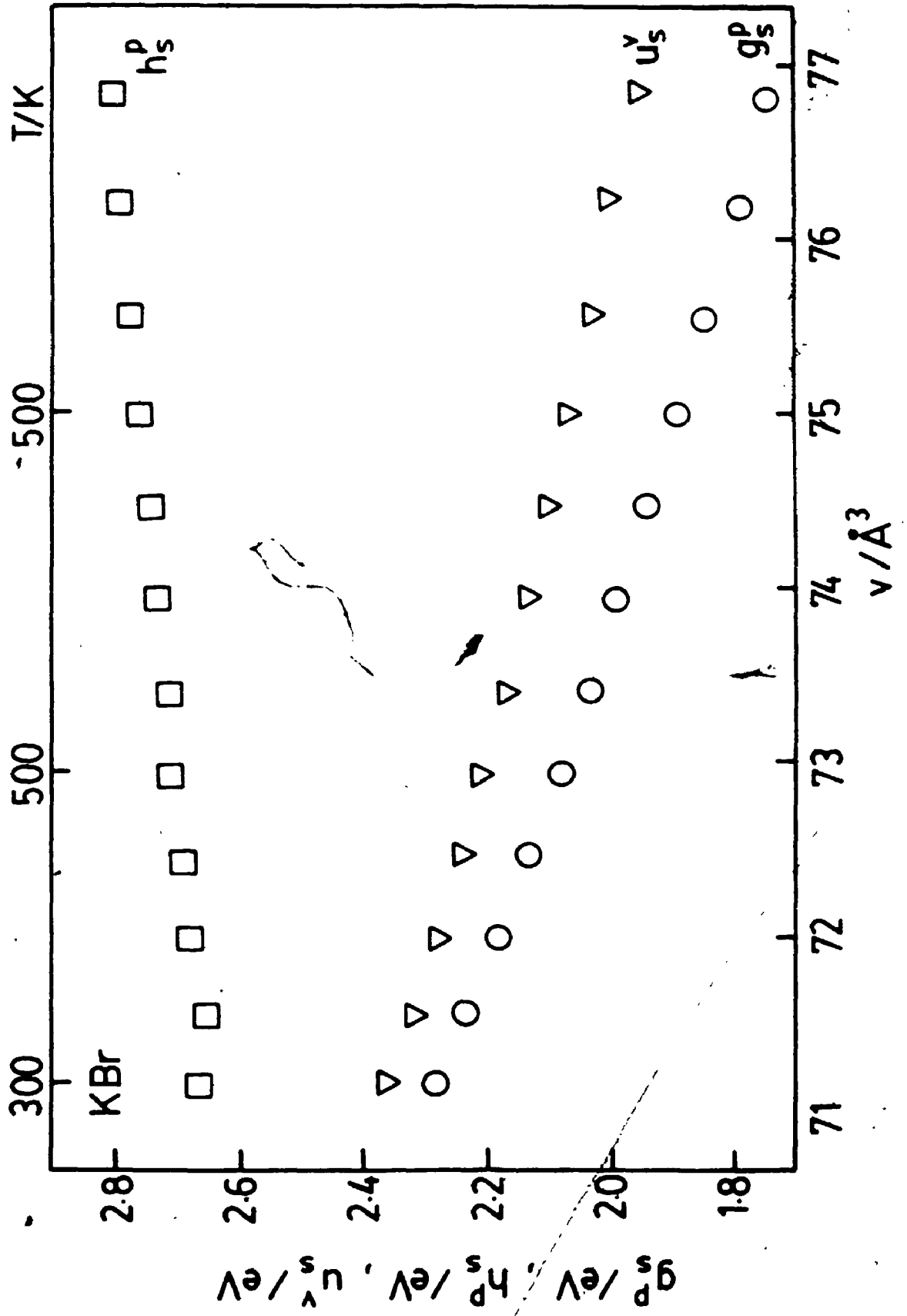


Figure 7-17: Values of s_{ξ}^{ρ} , s_{ξ}^{ν} , and v_{ξ}^{ρ}/v for KBr calculated using the TD potentials

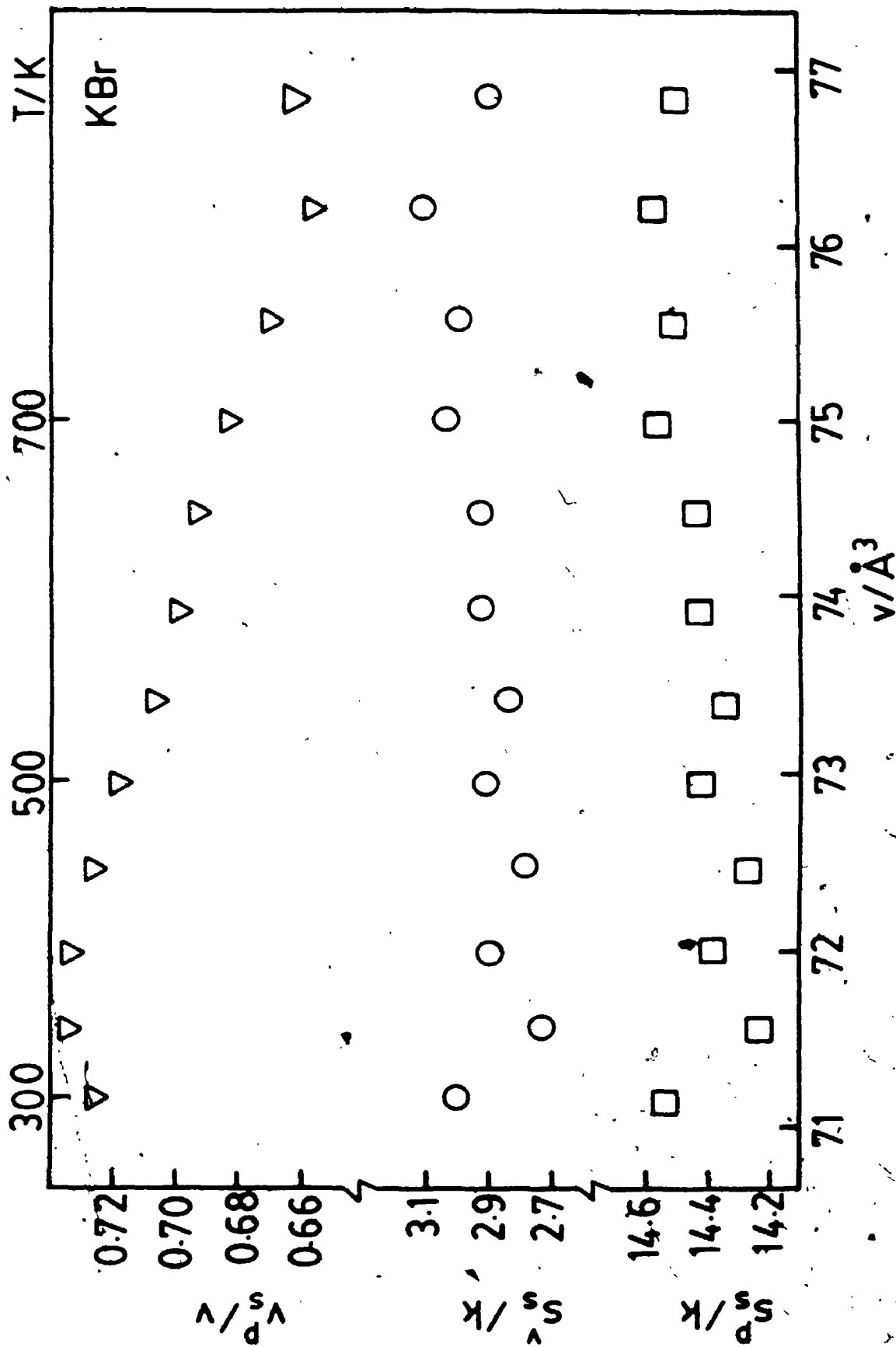


Figure 7-18: Values of Δg_{cv}^p , Δh_{cv}^p , and Δu_{cv}^y for KBr calculated using the TD potentials

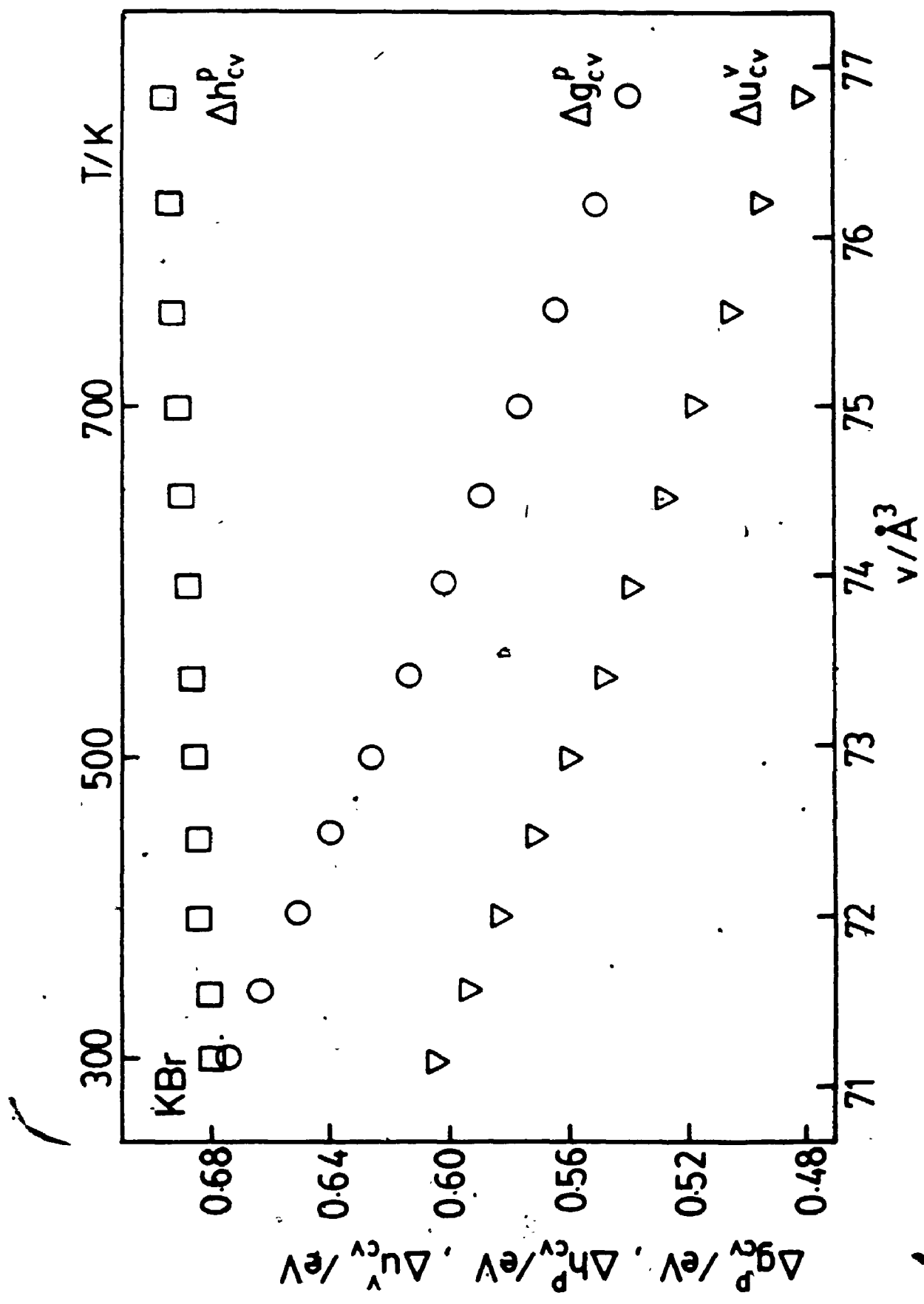


Figure 7-19: Values of Δs_{cc}^P , Δs_{cc}^V , and $\Delta v_{cc}^P/v$ for KBr calculated using the TD potentials

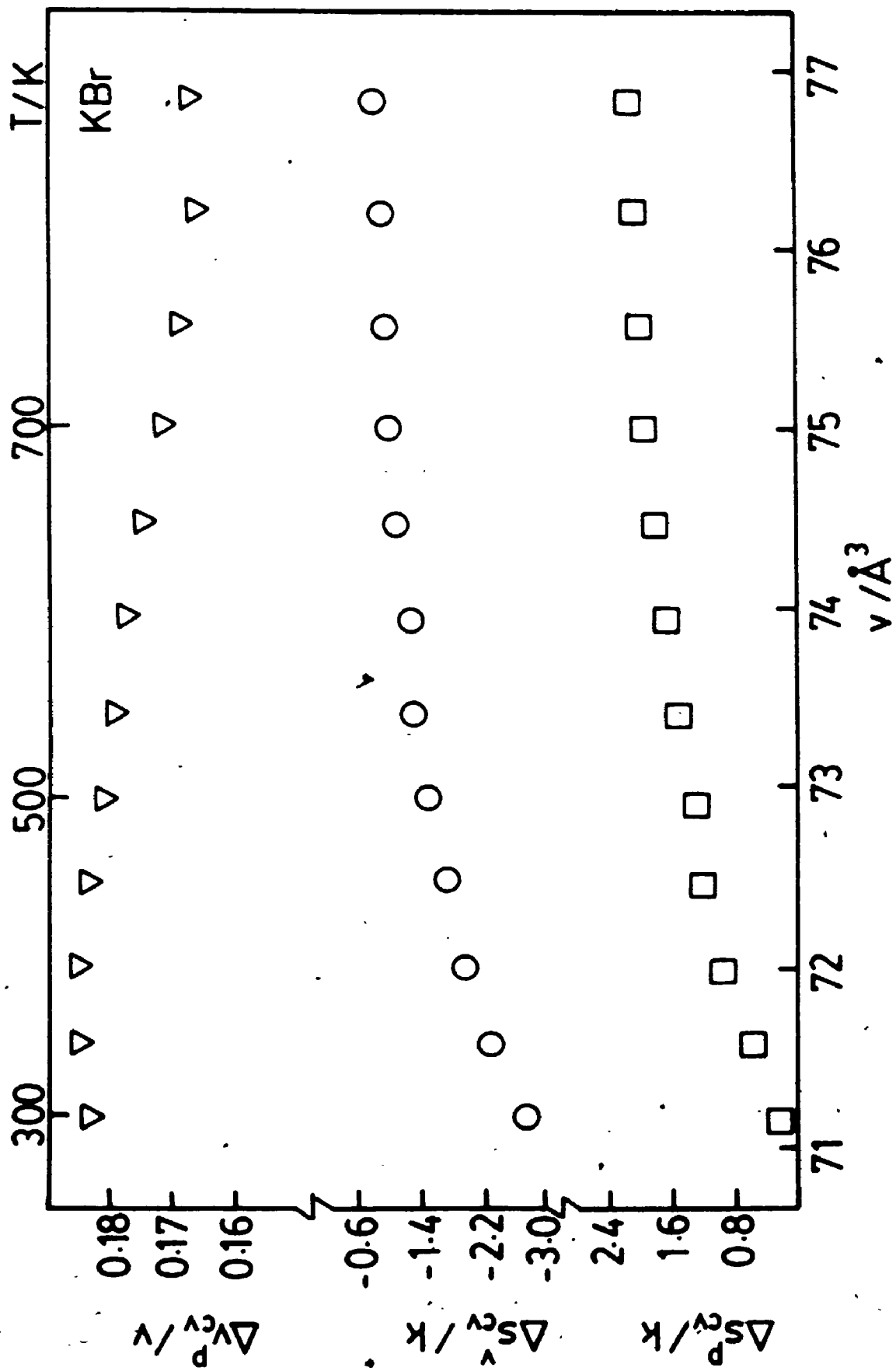


Figure 7-20: Values of Δg_{av}^p , Δh_{av}^p , and Δu_{av}^s for KBr calculated using the TD potentials

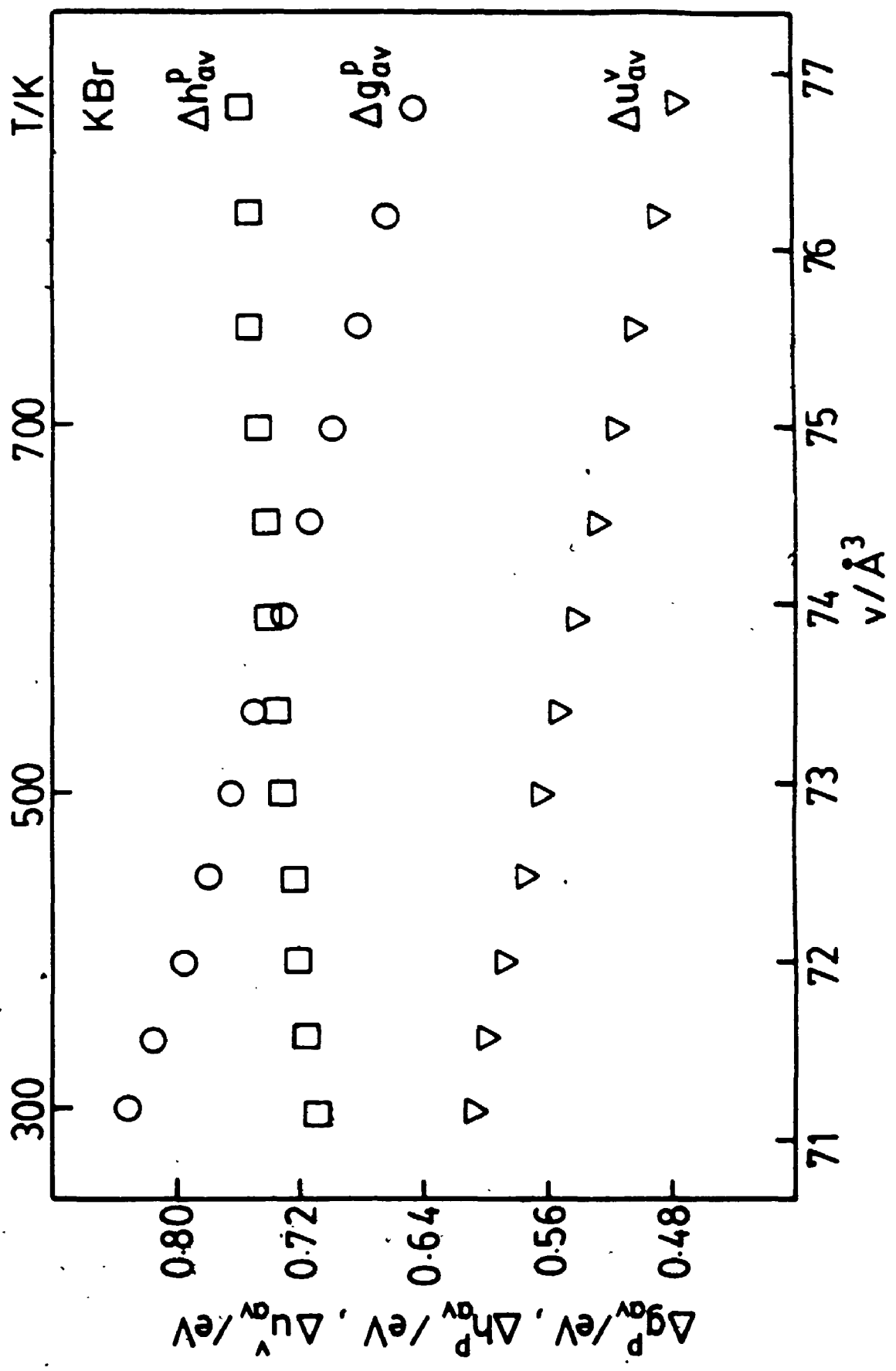


Figure 7-21: Values of $\Delta s_{\Delta v}^P$, $\Delta s_{\Delta v}^V$, and $\Delta v_{\Delta v}^P/v$ for KBr calculated using the TD potentials

